Department of Physics and Astronomy
University of Heidelberg

Reconstruction study of the S particle dark matter candidate at ALICE

Master Thesis in Physics
submitted by

Fabio Leonardo Schlichtmann

born in Heilbronn (Germany)

March 2021

Abstract:

This thesis deals with the sexaquark S, a proposed particle with $uuddss$ quark content which might be strongly bound and is considered to be a reasonable dark matter candidate. The S is supposed to be produced in Pb-Pb nuclear collisions and could interact with detector material, resulting in characteristic final states. A suitable way to observe final states is using the ALICE experiment which is capable of detecting charged and neutral particles and doing particle identification (PID). In this thesis the full reconstruction chain for the S particle is described, in particular the purity of particle identification for various kinds of particle species is studied in dependence of topological restrictions. Moreover, nuclear interactions in the detector material are considered with regard to their spatial distribution. Conceivable reactions channels of the S are discussed, a phase space simulation is done and the order of magnitude of possibly detectable S candidates is estimated. With regard to the reaction channels, various PID and topology cuts were defined and varied in order to find an S candidate. In total $2.17 \cdot 10^8$ Pb-Pb events from two different beam times were analyzed. The resulting S particle candidates were studied with regard to PID and methods of background estimation were applied. In conclusion we found in the channel $\overline{S} + \mathrm{p} \rightarrow \bar{\mathrm{p}} + \mathrm{K}^+ + \mathrm{K}^0 + \pi^+$ a signal with a significance of up to 2.8, depending on the cuts, while no sizable signal was found in the other studied channels. The mentioned significance does only reflect statistical uncertainties, therefore further studies are required with regard to systematic uncertainties. In general it was shown that it is feasible to search for the S particle at ALICE in the described way.

Kurzfassung:

Diese Arbeit handelt vom Sexaquark S, ein postuliertes Teilchen mit dem Quarkinhalt $uuddss$, das möglicherweise stark gebunden ist und als geeigneter Kandidat für die dunkle Materie betrachtet werden kann. Das S könnte in nuklearen Pb-Pb-Kollisionen erzeugt werden und könnte mit Detektormaterial interagieren, wodurch charakteristische Endzustände entstehen würden. Eine geeignete Möglichkeit, um diese Endzustände zu beobachten, stellt das ALICE-Experiment dar, das geladene und neutrale Teilchen detektieren kann und eine Teilchenidentifikation (PID) ermöglicht. In dieser Arbeit wird die komplette Rekonstruktionskette für das S beschrieben, insbesondere wird die Reinheit der PID für verschiedene Arten von Teilchen in Abhängigkeit von topologischen Beschränkungen untersucht. Außerdem werden nukleare Interaktionen im Detektormaterial in Bezug auf deren räumliche Verteilung betrachtet. Plausible Reaktionskanäle des S werden diskutiert, eine Phasenraumsimulation wird durchgeführt und die Größenordnung von möglicherweise detektierbaren S-Kandidaten wird abgeschätzt. Bezüglich der Reaktionskanäle werden einige geeignete PID- und Topologieschnitte definiert und variiert, um einen S-Kandidaten zu finden. Insgesamt wurden $2.17 \cdot 10^8$ Pb-Pb Events von zwei unterschiedlichen Strahlzeiten analysiert. Die gefundenen S-Kandidaten wurden hinsichtlich der PID untersucht und Methoden zur Untergrundabschätzung wurden angewandt. Abschließend fanden wir für den Kanal $\overline{S} + \mathrm{p} \rightarrow \bar{\mathrm{p}} + \mathrm{K}^+ + \mathrm{K}^0 + \pi^+$ ein Signal mit einer Signifikanz von bis zu 2.8 in Abhängigkeit von den Schnitten, während kein ähnliches Signal für die anderen betrachteten Kanäle gefunden wurde. Die erwähnte Signifikanz spiegelt nur die statistischen Unsicherheiten wider, daher sind weitere Studien hinsichtlich systematischer Unsicherheiten notwendig. Im Allgemeinen wurde gezeigt, dass es möglich ist, mit der beschriebenen Vorgehensweise das S-Teilchen in ALICE zu suchen.

This Master Thesis has been carried out by Fabio Schlichtmann at the
Physikalisches Institut in Heidelberg
under the supervision of
Prof. Dr. Klaus Reygers

Contents

1 Introduction

This chapter provides an overview about the Standard Model of particle physics including the fundamental particles, their interactions and especially the formation of hadrons, which is described by the fundamental theory of strong interaction, called Quantum Chromodynamics (QCD). Additionally to the well known mesons and baryons, exotic hadrons are mentioned. A brief introduction to some cosmological observations is given. They lead to the proposed existence of dark matter and dark energy which are currently intensively studied in the fields of astronomy and physics in general. Besides some other candidates, the proposed sexaquark S is mentioned and presented in detail. Thereby its properties and stability, as well as strategies for detection, will be discussed.

1.1 Overview of the Standard Model

The Standard Model (SM) of particle physics is the commonly accepted theory that describes all matter by fundamental particles, bosons and fermions, divided into quarks and leptons, as well as all their interactions, the so called fundamental forces, except for gravity [1]. It was developed in the early 1970s and is the result of theories and discoveries of thousands of physicists, so it is able to explain nearly all experimental results and therefore has become established as one of the most well-tested theories in particle physics. Three of these four previously mentioned forces are included in the SM: electromagnetic, weak, strong but not gravitational force, and these interactions are mediated by force-carrying bosons. All fermions can be divided in three generations as shown in Figure 1.1 and for each mass-carrying lepton exists a corresponding (nearly) massless neutrino [2]. Various quantities are associated with each fundamental particle like mass, electric charge, color charge and weak isospin, that determine their coupling to interactions. Gravity, despite being extremely weak compared to all other forces, couples to all massive particles and is always attractive, so therefore it is responsible for the large-scale structure of the universe [2]. On a smaller scale, atoms are formed by electrostatic attraction between oppositely electrically charged electrons and protons, which is described in detail by the low-energy manifestation of Quantum Electrodynamics (QED), the fundamental theory of the electromagnetic interaction [2]. Analogously to QED, there is a theory called Quantum Chromodynamics (QCD), that describes fundamentally the strong interaction between color charge carrying quarks and is responsible for the formation of mesons and baryons – a more detailed description will follow in section 1.3. Because every fermion carries weak isospin, all of them couple to the weak force which e.g. is responsible for β-decays. The three forces, included in the SM, are mediated via the exchange of spin-1 force-carrying gauge bosons which are photons in QED, gluons in QCD and $W^{\pm}$ or Z bosons in the weak interaction [2]. The way how these interactions

	Leptons				Quarks			
	Particle		Q	mass/GeV	Particle		Q	mass/GeV
First	electron	(e^-)	−1	0.0005	down	(d)	−1/3	0.003
generation	neutrino	(ν_e)	0	$< 10^{-9}$	up	(u)	+2/3	0.005
Second	muon	(μ^-)	−1	0.106	strange	(s)	−1/3	0.1
generation	neutrino	(ν_μ)	0	$< 10^{-9}$	charm	(c)	+2/3	1.3
Third	tau	(τ^-)	−1	1.78	bottom	(b)	−1/3	4.5
generation	neutrino	(ν_τ)	0	$< 10^{-9}$	top	(t)	+2/3	174

Figure 1.1: Overview of fermions, divided in leptons and quarks, and structured in three generations – taken from [2]. The charge and mass are shown, while the latter is only written as an approximate value.

occur can be represented as Feynman diagrams [3]. According to the SM, for each fundamental particle there exists a corresponding antiparticle which has, if one assumes that CPT-invariance holds, the same quantities like mass, lifetime and spin but opposite charge, magnetic moment and additive quantum numbers [4]. How these and other quantities are conserved in interactions, will be expounded in section 1.2.

1.2 Conservation laws

If a fundamental or composite particle interacts, some quantities are conserved, depending on the type of interaction. The resulting conservation laws are briefly described in this section, because later in section 5.2 especially the strangeness and baryon number conservation will be of importance, in order to define possible reaction channels. There is a variety of quantities and quantum numbers that is structured in the following:

- **4-momentum, angular momentum**
  conserved in all interactions [5]

- **Charge**
  conserved in all interactions [5]

- **Lepton numbers L_e L_μ, L_τ and total lepton number L**
  L_e = N(e)-N($\bar{e}$), others analogously, L = L_e + L_μ + L_τ
  approximately conserved in all interactions (except for neutrino oscillations [6]), total L is always conserved [5]

- **Baryon number B**
  B = +1/3 for quarks, B = -1/3 for antiquarks
  conserved in all interactions [7]

- **Strangeness S, Charm C, Topness T**
  S = N($\overline{S}$)-N(S), C = N(C)-N($\overline{C}$), T = N(T)-N($\overline{T}$)

conserved in strong and electromagnetic interactions, violated in weak interactions [7]

- **Isospin I, third component I_3**
  conserved in strong interaction, I_3 conserved in electromagnetic but I is violated in e.m., both violated in weak interaction [7]

- **Parity π**
  conserved in e.m. and strong interaction, violated in weak interaction [2]

1.3 Mesons and baryons

This thesis will deal with an exotic particle, therefore it is helpful to remind us of the common hadrons. Hadrons are subatomic composite particles, consisting of two or more quarks that are bound together by the strong force. The fundamental reason for the binding between quarks lays in QCD and is explained by the hypothesis of color confinement, which says, that no objects with non-zero color charge can exist as free objects. A qualitative understanding can be given by considering two quarks that are pulled apart from each other. These quarks interact with each other by the exchange of virtual gluons, while these gluons also interact among each other attractively because of carrying color charge. This leads to the formation of a 'tube' between the two quarks with constant energy density at large distances. Therefore the energy stored in the gluon field would increase linearly with distance. Accordingly free color charges at large macroscopic distances can not exist, because the stored energy would be enormous and therefore quarks are confined to colorless hadrons. The term 'colorless' means that in SU(3)-algebra any operation of a color ladder operator on the colorless state must yield zero, which will not be derived here. In conclusion one can say that a combination of a quark, that carries a color charge, and an antiquark, carrying the corresponding anticolor, is possible and this composite particle is called meson. Moreover baryons can be formed, usually consisting of three quarks with three different color charges – exceptions of hadrons made of more quarks are discussed below in section 1.4. Similar to fundamental particles, each hadron has a corresponding antiparticle with the opposite quark content, so each quark is replaced by its antiquark. Most of the known matter is only made of two baryons, the proton and the neutron, which form nuclei and combined with electrons they form atoms. It is assumed that almost all free hadrons decay except for the proton. Various other mesons and baryons than protons and neutrons can be produced and studied in high-energy collisions which happen at particle colliders. This will be described in more detail in chapter 2.

1.4 Exotic hadrons

In general every quark combination that does not fulfill the criteria of a usual meson or baryon[1], and therefore consists of more than three quarks, is called exotic hadron. Although usual mesons and baryons are much more often solely described in textbooks, there is no a priori reason why only hadrons with two or three quarks should exist. In fact even in the original paper from 1964 by Gell-Mann who postulated the quark model first[2], the possibility of exotic hadrons is mentioned [9]. Furthermore quantum chromodynamics, the theory of strong interactions between quarks and gluons, allows states with more than three quarks. Experimentally, exotic hadrons can be searched for by looking at scattering events with quantum numbers forbidden to ordinary hadrons, because as described in section 1.2 in particular the baryon number is conserved. There are some candidates and experiments with the aim of discovering them. The LHCb collaboration confirmed the existence of the $Z(4430)^-$ particle with the minimum quark content of $c\bar{c}d\bar{u}$ within a significance of 13.9σ, considering all the systematic variations in their model [11]. They studied resonant structures in $B^0 \to \psi' \pi^- K^+$ decays and found out that the data cannot only be described with $K^+\pi^-$ resonances alone, but there is a $Z(4430)^- \to \psi' \pi^-$ component required. Another example of the so called tetraquarks is the X(3872) state, that was first seen in 2003 by the Belle experiment [12] and confirmed by BaBar, CDF and D0. The quark content of this state is $u\bar{u}c\bar{c}$. There are different explanations how this state could be formed on the quark-level: The observed decay into a J/ψ and two charged pions suggests that it could be a new, excited charmonium state, binding a charm quark with its antiquark. On the other hand, it is also possible, that the X(3872) state is rather like a loosely-bound D^0-$\bar{D}^{*0}$-'molecule' or a 'tetra-quark', binding a di-quark and a di-antiquark. Both mentioned possibilites are supported by the fact, that the mass of X(3872) (3872 MeV) is very close to the sum of the masses of the D^0 and $\bar{D}^{*0}$. There are some (but compared to normal hadrons rather few) other candidates for tetra or pentaquarks, that are believed to have been observed, however they still remain a topic of controversy in particle physics. Hexaquarks have not yet been seen, but as explained in section 1.6.1 one candidate was proposed and the study of the feasibility to detect it, if it existed, will be the main part of this thesis.

1.5 Dark matter

In this section some cosmological observations are mentioned that suggest the existence of dark matter. General constraints to its properties and some promising candidates are presented. This section does not claim completeness, it should rather be seen as a short overview about dark matter, because discussing any observation or candidate in detail would rather give rise to several theses and therefore exceeds the limits of this work.

[1] Some sources define a meson and baryon as composite particle with exactly two respectively three quarks [8], others demand that mesons have even, and baryons odd quark numbers [9]. In the following I will use the term 'usual meson/baryon' that corresponds to the first mentioned definition.

[2] In fact G. Zweig postulated the existance of quarks independently from Gell-Mann in 1964 and called them 'aces'. [10]

1.5.1 Cosmological observations

Spiral galaxies show a velocity distribution of the orbital speed of visible stars or gas as a function of their radial distance from the center, called velocity curve. Applying the theory of gravity, using the observed matter in galaxies, allows one to predict this curve. For systems, whose mass is mainly concentrated in the center, like in the rather simple example of our solar system, one expects that the orbital velocities of objects decline with distance according to Kepler's third law. In galaxies we also observe a centrally focused mass distribution, so roughly speaking we expect the same decline of orbital velocities for increasing radii. However, this is generally not observed – see e.g. [13] and look at Figure 1.2. The rotation curve of many galaxies is not decreasing with radial distance, but rather flat or slightly increasing, which contradicts the theoretical predictions from gravity theory together with the visible matter. In general there are two ways to explain this discrepancy: Modifying the Newtonian dynamics or assuming that there is any non observed 'dark' matter also in outer regions of the galaxy, which boosts the star velocities. The former is done in the MOND hypothesis, which particularly claims, that Newton's laws have been tested extensively in high-acceleration environments, but are not verified for objects with extremely low accelerations, as stars in outer regions of galaxies, allowing to modify the gravity in that region [14]. However, the theory of dark matter is by far the most acknowledged theory in physics.
Besides the rotation curves, there are many other observations contradicting the predicted behaviour from observed mass distributions, motivating dark matter. Studying the X-ray emission of galaxy clusters, leads to a temperature and density profile, that can be used to estimate pressure. Assuming pressure and gravity balance in a hydrostatic equilibrium, the clusters mass profile can be estimated, resulting in a mass approximately five times higher than expected from visible objects [15]. Another cosmological result, which is in agreement with the existance of dark matter, are mass-to-light ratios of clusters obtained from gravitational lensing [15]. Some other, not further discussed, examples of observations that support the existence of dark matter are studies concerning the cosmic microwave background, measured by Wilkinson Microwave Anisotropy Probe (WMAP) mission [16], density perturbations when structure formation occurred after the Big Bang and the observed accelerated expansion of the universe [17].
In conclusion one can say, that there is very strong evidence that dark matter exists, so that it is included in the Lambda-CDM model [18], which is often referred as the standard model of Big Bang cosmology. According to this theory, normal matter only contributes 5% to the total mass-energy in the universe, while 27% dark matter and 68% dark energy are contained. Of course if one agrees that dark matter exists and even dominates the mass-energy in the universe, the questions arise which restrictions to properties of DM can be made, if there are candidates that fulfill these, and why they eluded all searches up to date. This will be of interest in section 1.5.2.

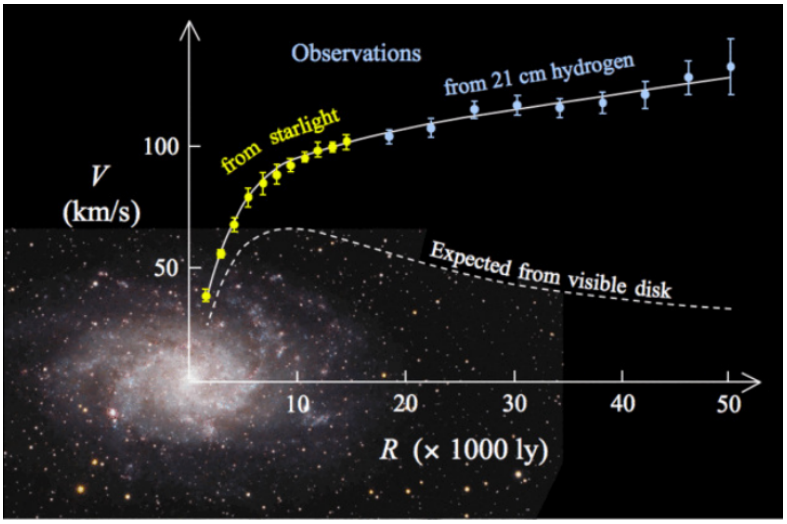

Figure 1.2: Rotation curve of the M33 spiral galaxy, and predicted curve from visible matter. The distribution of visible matter is visualized in an 'image' of the galaxy. Obviously there is a large discrepancy between expectation and measurement that can be explained by a dark matter halo surrounding the galaxy. Figure taken from [19], data from [13].

1.5.2 Properties and candidates

In general dark matter could be any type of matter that predominantly interacts with normal matter by gravitation, so that there are many types of candidates. Discussing all of them would exceed the limits of this chapter – the interested reader is referred to [20] – so they will only be mentioned shortly. Firstly, there are some basic constraints on properties of dark matter candidates in order to be in agreement with observations. Due to the fact that dark matter is not observed to shine, it must be optically dissipationless and therefore has to have very weak electromagnetic interactions. Thereby it is supposed to have either a vanishing electric charge and dipole moment, or it might be very heavy. Moreover, observations imply that dark matter is at least nearly collisionless with normal matter. The study of two clusters, that pass through each other, show a collisionally merged gas distribution, but galaxies and lensing masses are largely intact, which implies directly that DM did not significantly collide with galaxies [21]. Observations strongly suggest, that the DM is 'cold' or in other words sufficiently non-relativistic. This constraints the mass to be larger than 1 keV for particle species in thermal equilibrium [20]. Furthermore dark matter must be sufficiently small on galaxy scales, so that it eludes searches for discrete massive objects. Dark matter is supposed to exist since the beginning of the universe, explaining as mentioned before e.g. the cluster formations. Accordingly, the lifetime of DM candidates has to be much longer than the Hubble time $\approx$ 1Gyr. Another restraint is, that its cosmological density has to be compatible with the observed dark matter density. This could be achieved by thermal processes during early times of the universe. When the universe expands, the

production and annhilation rates become longer than the Hubble time, which is called 'freeze out', and at that point the density does not change any more. The evolution of the particle density from its equilibrium value, is described by the Boltzmann equation and the final density of the particles after freeze-out depends on whether the extant frozen-out dark matter is relativistic or not. A detailed calculation can be found in [20]. In general one can conclude, that particles whose calculated relic density match the observed dark matter density are serious candidates. For example Weakly Interacting Massive Particles (WIMPs) would have sufficient mass to give a proper relic density in non-relativistic freeze-out and thus might be a compelling dark matter candidate. Other candidates, that generally satisfy the mentioned restrictions, are spread over a large variety of particle species and energy ranges. One possibility would be that dark matter consists of hadronic matter that might be hard to detect, motivated by the fact that other hadronic objects (e.g. neutron stars, white dwarfs etc.) are also barely detectable. However, there is evidence suggesting that dark matter is not made of hadrons like the visibility when backlit by stars or the fact that baryonic dark matter would usually interact with ordinary matter not just by gravitational effects. As alternative there are also DM candidates that consist of non-baryonic matter. To list some of them, there are axions, a hypothetical elementary particle, and fuzzy cold dark matter, consisting of extremely light scalar particles. In the theory of supersymmetry, for each Standard Model particle there exists a so called superpartner, which differs in spin (and mass for a broken symmetry). If one assumes that the decay of a superpartner in the SM particle is strongly suppressed, in order to agree with experimental results, any superpartner could be theoretically a dark matter candidate. Especially the lightest neutralino, a composite of superpartners of gauge bosons, which has in some models a mass of a few hundred $\mathrm{GeV/c^2}$, might be a candidate for a weakly interacting massive particle.

There are various experiments with the aim to detect dark matter, focusing on different candidates. One of them is the CRESST experiment (Cryogenic Rare Event Search with Superconducting Thermometers) that uses ultra cold calorimeters in order to detect dark matter particles directly (e.g.) WIMPs. A main challenge in this experimental approach is the very low expected interaction rate and suppression/determination of background events [22]. Other examples of experiments, which will be just mentioned, are the MADMAX experiment, searching for axions, and the TRISTAN detector in the Katrin experiment, trying to detect sterile neutrinos [23]. In spite of the huge experimental effort, no convincing result that might indicate the existence of a DM candidate has been seen. Therefore besides searching for the most prominent candidates, it is also reasonable to open the view for more unconventional DM candidates.
An extraordinary dark matter candidate is the sexaquark S, which is presented in more detail in section 1.6. Despite being made of hadronic matter, it fulfills various of the above mentioned criteria, like being neutral, possibly stable and in particular that the density ratio of DM to baryons is in agreement with observations – see section 1.6.4.

1.6 The sexaquark

In this chapter the proposed neutral, B=2, flavor singlet sexaquark (S) composed of $uuddss$ is described. In the following an overview about the properties of the S, especially its mass and linked to that the stability will be given. Furthermore the ways of possible discovery (and former searches) are mentioned. According to its properties, the S might be a serious dark matter candidate, as discussed in section 1.6.4.

1.6.1 H dibaryon and proposal of the S

The sexaquark was proposed by Farrar in August 2017 [24]. She discusses why it could be formed by attraction, why it should be tightly bound considering the symmetries of the wave function, which mass might be reasonable and why it eluded all searches up to date.
Already 40 years ago, R. Jaffe pointed out [25] that a $uuddss$ state might be attractive and estimated a mass of $\approx 2150\,\mathrm{MeV}$, using a 1-gluon-exchange bag model calculation of hyperfine splitting, so its mass is 81 MeV lighter than the $\Lambda\Lambda$ threshold. He called this particle H-dibaryon. Because it is the ground state in the **S**=-2 sector of a **B**=2 system, the H-dibaryon cannot decay via strong but only by weak interaction. Due to the mass of $\mathrm{m}_H > \mathrm{m}_p + \mathrm{m}_e + \mathrm{m}_\Lambda$, its lifetime is estimated to be in the order of $10^{-10}\,\mathrm{s}$. Although lots of experimental efforts have been made, no convincing result for the existence of the H-dibaryon has been found [26]. However one has to mention, that experiments disfavor states with mass $\leq 2\,\mathrm{GeV}$. So it may be possible, that there is a $uuddss$ sexaquark which instead of being fairly loosely-bound, is deeply bound with low enough mass to be stable or essentially stable. This is the proposed particle by G. Farrar which is newly designated as 'S'[3] for Sexaquark, Singlet, Scalar, Strong and Stable.

1.6.2 Properties and stability

This chapter provides information about properties of the S, that are taken from G. Farrar's paper [24]. The general properties of the S are that it is a spin-0, flavor-singlet, parity even boson with **Q**=0, **B**=2 and **S**=-2. Its spatial wave function can be totally symmetric, while the color, flavor and spin wave function are individually antisymmetric. Theoretically, lattice QCD should be able to predict whether the sexaquark is stable, but studies concerning that topic are still far from the physical limits, using non-relativistic quark masses (in contrast to the ultra relativistic reality). As mentioned before, the S is assumed to be deeply bound and the stability is determined by its mass. If $\mathrm{m}_S \leq 2(\mathrm{m_P} + \mathrm{m_e}) = 1877.6\,\mathrm{MeV}$, the S would be absolutely stable due to baryon number conservation, while if $\mathrm{m}_S < \mathrm{m_P} + \mathrm{m_e} + \mathrm{m}_\Lambda$ the lifetime would be longer than the age of the universe, because it could only decay by a doubly-weak interaction. Accordingly, it is quite important to estimate the mass of the S (m_S), but there is no good empirical analog for assessing it based on other hadron masses. Some physicists argue [24] that a stable

[3] In order to avoid confusion with strangeness, the sexaquark is written as S, while the quantum numbers are written in bold letters **S** and **B**.

sexaquark is unlikely because they rely on the simple model, that each light/strange valence quark contributes to the hadron mass with $\sim 300/450\,\mathrm{MeV}$. However, this model is invalid which can be seen for example in the masses of the mesons: $\pi^{0,\pm}$ which are 135 and 140 MeV, so they are much lighter than the 'predicted' 600 MeV. Generally, there are many different mechanism that determine the mass of hadrons: hadrons consisting of light and strange quarks are highly relativistic bound (the quark masses are much lower than the hadron mass) and for $\pi^{0,\pm}$ the low mass is associated with them to be pseudo-Goldstone bosons of chiral symmetry breaking. Comparing the mass of two Λ's to the 'stability-limits' mentioned above, the result is that only 16% (10%) relative binding energy would be enough for the S to be stable (essentially stable), which seems small compared to the mass shifts in the meson sector.

There are three attributes that might be reasons why the conjectured S has not been detected so far: due to its mass it is difficult to distinguish it kinematically from the neutron, it doesn't couple to photons, pions and most other mesons, and it is probably more compact than usual hadrons. Anyway, the S nucleon scattering cross section is estimated to be in the same order as σ_{NN}^{el} (5-20 mb) for geometric reasons, so if a S existed, its scattering could be detected. However the production rate has to be sufficiently large so that sexaquarks are produced. The production in baryon collisions depends on the wave function overlap between the S and two baryons. If one uses the heuristic model, that there is a price of $\mathrm{O}(10^{-1})$ for each additional quark, based on the meson to baryon ratio in high energy collisions, this would imply that the S production-rate in hadronic interactions is 10^{-4} to 10^{-6} relative to pions. As a consequence, S particles would be produced regulary in high-energy collisions, although they might not be recognized because of the overwhelming neutron background which is $\mathrm{O}(10^{3-5})$ larger than S production rate. Neutrons behave similiarly: they are also neutral, in the same mass range, and the scattering cross section is in the same order, so if one does not especially search for a typical hadronic reaction channel with strangeness **S**=-2, the interaction would be normally dismissed [27]. In section 1.6.3 some possible strategies how the detection of the S might be possible are discussed.

1.6.3 Suggested strategies for detection

Glennys Farrar suggests different methods in accelerator based searches for the S particle [24]:
It is possible to observe the Υ decay, which may happen in a reaction like: $\Upsilon \rightarrow S\overline{\Lambda\Lambda}$ or $\overline{S}\Lambda\Lambda$ + pions and/or γ. If every final particle can be detected, then the mass of the unseen S can be reconstructed from 4-momentum conservation. Due to the high resolution of some detectors, the missing-mass peak could be resolved in the order of 20 MeV and already a few events, having a common missing mass, would be a serious indication for the existence of the S. In general, also other final states besides $\overline{\Lambda\Lambda}/\Lambda\Lambda$ could be used in order to discover the $S/\overline{S}$, as long as they fulfill the requirement of B = ± 2 and S = ∓ 2 quantum numbers. Experimentally, states containing Λ's are well detectable, because of the short decay length ($c\tau = 8\,\mathrm{cm}$) and the branching fraction of 64% to charged final states $\mathrm{p}\pi^-$, resulting in a high reconstruction efficiency for Λ's.

An experimental investigation of the above described strategy was done by the BABAR experiment [28]. They inspected a sample of $90 \cdot 10^6 \Upsilon(2S)$ and $110 \cdot 10^6 \Upsilon(3S)$ decays, with the result that no signal was observed. Accordingly, they were able to set an upper limit on the combined $\Upsilon(2S, 3S) \to S\overline{\Lambda}\overline{\Lambda}$ branching fraction in the range of $(1.2\text{-}1.4) \cdot 10^{-7}$ with 90% confidence level, including systematic uncertainties and background estimates.

Another suggested experimental approach is to study $\overline{S}$ annihilation, respectively S nucleon interactions, in an LHC detector, which is done in this thesis. As estimated above, sexaquarks might be produced in LHC collisions with a rate of approximately $10^{-4} - 10^{-6}$ relative to neutrons. This $\overline{S}$ can interact with a proton or neutron in the beam-pipe or detector, resulting in a characteristic final state with strangeness S = 2. Especially heavy ion collisions seem to be a very attractive production channel, because the produced quark-gluon plasma (QGP) has a very high energy density, which increases the production probability for the S, and it resembles the conditions of the early universe. At that time in the universe presumably the Dark Matter is produced, and if one assumes that the dark matter might consist of sexaquarks (see section 1.6.4) then it is reasonable to suggest, that the S is produced in heavy ion collisions. Therefore the ALICE experiment at LHC – see chapter 2 – seems to be the most promising experiment to deal with the sexaquark production, due to its capability to detect remnants of the quark-gluon plasma even with good resolution for small momenta and its ability to do satisfactory particle identification.

A previous search for the S at LHC was done by Florian Partous for p-p collisions and CMS-data – see [29]. He focused on nuclear interactions of the $\overline{S}$ with material layers of the CMS detector, studying the process:

$$\overline{S} + n \to \mathrm{K}_s^0 + \overline{\Lambda}^0. \tag{1.1}$$

The result was that no signal has been seen and an investigation of potential background, as well as a discussion of reconstruction efficiencies, led to an estimation of the upper limit, of $\sigma(\mathrm{pp} \to \overline{S}) = 43\,\mathrm{mb}$ at 95% confidence level. However a smaller cross section is conceivable as suggested by Farrar, and an even lower value can be obtained by estimating $\sigma(\mathrm{pp} \to \overline{S})$ based on the production cross section for deuterium – see section 5.4. Accordingly, a detection might still be feasible, but requires higher statistics and possibly should include other reaction channels. In addition, from our point of view, the reaction channel Equation (1.1) is allowed but, according to the OZI rule, it should be suppressed compared to the same channel including two additional pions – see section 5.2.

1.6.4 The S as dark matter candidate

This chapter should continue section 1.5.2 and discusses indications why the S might be a good candidate for being a dark matter particle. A detailed discussion exceeds the limits of this thesis – the interested reader is referred to [27], which is summarized here. In general it is not possible to decide on theoretical grounds whether there is an undiscovered stable sexaquark dark matter candidate, but its existence is not excluded

either by accelerator experiments, dark matter direct constraints or astrophysical constraints. In accelerator experiments the S might not have been seen for several reasons. Former searches might be inapplicable, because they either looked at the H-dibaryon through decay (but the S is assumed to be stable), or restricted the mass to $> 2\,\mathrm{GeV}$. Additional experimental challenges are the similarity to neutrons and the possibly low scattering cross section for interactions with detector protons/neutrons. The relic density of the S is determined by the physics of the transition from QGP to hadrons and in [27] it was derived from statistical physics and known parameters from QCD, like quark masses, abundance ratios and relevant temperature range, that the density ratio of DM to baryons is $\Omega_{DM}/\Omega_b \approx 5$. This is in very good agreement with the observed value of $\Omega_{DM}/\Omega_b = 5.3 \pm 0.1$. To sustain this ratio, the S has to be at least essentially stable, as discussed in section 1.6.2. In general, S dark matter would interact with baryons via a Yukawa potential, while the strength of this potential α_{SN} and its sign is a main uncertainty. Therefore the attractive and repulsive case can be treated separately. In order to be compatible to primordial nucleosynthesis, there is the constraint that $\alpha_{SN} < 0.7$ to avoid primordial ^{4}He to form a bound state with an S. If $\alpha_{SN} > 0.2$ the S could bind to oxygen in the Earth's oceans, crust and atmosphere, forming exotic isotopes, that have not been explored with adequate sensitivity. In a repulsive case, the maximum Yukawa coupling is restricted to be $|\alpha_{SN}| < 0.004$ and the cross section with nuclei has to be $\sigma_{SN} < 10^{-29}\mathrm{cm}^2$ in order to be compatible with limits from dewar experiments. If the cross section would exceed $\approx 10^{-28.5}\mathrm{cm}^2$, this would lead to a formation of a DM atmosphere with a density that would cause detectable effects, allowing to place limits on DM interactions with various materials. To sum it up, there are serious indications why the S might be a good dark matter candidate, that, for a set of suitable unknown parameters, could be in agreement with all dark matter and astrophysical constraints and might have eluded all accelerator experiments up to date. Combining the facts that the S, if it exists, would not just be the first hexaquark but in addition might be a serious dark matter candidate, and minding that the ALICE experiment could be the suitable way to detect it, this gives us more than sufficient motivation to study the feasibility of the S search in ALICE.

2 The ALICE experiment at CERN

In this chapter, a short overview about the history of CERN is given and some facts of the LHC are provided. Then, in more detail, the ALICE experiment and especially the construction and functionality of the detectors, relevant for this analysis, are explained.

2.1 CERN

The European Organization for Nuclear Research (Conseil Européen pour la Recherche Nucléaire) is a multinational organization based in Geneva, Switzerland, consisting of 22 member states and approximately 3200 employees, while there are totally about 14000 participating researchers among others research physicists, engineering/technical workers, and participating students [30]. CERN was founded in 1954 and invented several new techniques like for example in detector development, the multiwire proportional chamber, that was awarded with a Nobel Prize in 1992, has been designed by CERN staff researcher Georges Charpak [31]. Besides detectors, CERN built various particle accelerators like linear accelerators, e.g Linac 2 in 1978 and synchrotrons. The most prominent one is the LHC, which will be described in the following chapter.

2.2 LHC

The Large Hadron Collider (LHC) is the largest and most powerful particle accelerator ever built, located in an 26.7 km long tunnel below the surface close to Geneva [32]. It is designed for proton-proton and lead-lead collisions reaching center of mass energies of up to $\sqrt{s} = 14\,\text{TeV}$ (p-p) and $\sqrt{s_{NN}} = 5.02\,\text{TeV}$ (Pb-Pb). In order to keep the beam in a circular path, 1232 superconducting dipole magnets generate strong magnetic fields of 8.36 T. Before entering the LHC, the particles have to be pre-accelerated by various linear and ring accelerators [33]. In proton mode the first system is a linear particle accelerator LINAC 2 respectively LINAC 4[1], followed by the Proton Synchrotron Booster (PSB), the Proton Synchrotron (PS) and the Super Proton Synchrotron (SPS). For heavy ion mode, the LINAC 3 is used and instead of entering the PSB, the ions are stored and cooled in the Low Energy Ion Ring (LEIR). Then the particles are injected in bunches of around 10^{11} protons respectively $9 \cdot 10^7$ ions [34] into the LHC, which consists of two beam pipes in vacuum, so that the bunches orbit clockwise and anticlockwise. These beam pipes cross at four points where the detectors CMS, LHCb, ATLAS and ALICE are located. At these crossing points up to $6 \cdot 10^8$ collisions/s occur and are

[1] LINAC 2 was replaced by LINAC 4 in August 2020. The data used in this analysis were measured in the period in which LINAC 2 was installed.

detected [32]. All 4 experiments study these collisions and the created particles, focussing on various physics topics. The CMS detector is, among other things, able to detect muon tracks precisely and especially deals with supersymmetry. In 2012 the Higgs boson was discovered independently by CMS and ATLAS [35]. Furthermore, ATLAS and LHCb study the decay of hadrons and generally test the Standard Model e.g. by precise measurements of CP violation. Heavy ion collisions and in this regard the quark-gluon plasma is a research field especially in CMS, ATLAS and ALICE. The ALICE experiment will be described more detailed in chapter 2.

2.3 ALICE

ALICE (A Large Ion Collider Experiment) is a unique detector system, which is part of the LHC facility at CERN. It is optimized to study heavy ion collisions at high center of mass energies and therefore it is capable of deepening the understanding of matter in a high temperature and energy density state, the quark-gluon plasma (QGP) [36]. ALICE is designed to cope with high charged particle multiplicities of up to 8000 charged particles per unit of rapidity, produced in Pb-Pb collisions, and capable of identifying charged particles in a large transverse momentum range from $p_T = 0.15\,\mathrm{GeV}/c$ up to $20\,\mathrm{GeV}/c$ [37], combining measurements of different sub-detectors. In total, the ALICE detector has a length of 26 m, is 16 m in diameter and its mass is about 10 000 t [36]. The main part of the ALICE detector is a central barrel surrounding the beam pipe, which is fully contained within a solenoid magnet that provides a magnetic field of 0.5 T. Moreover, a part of the ALICE detector is a muon tracker, which does not play a role in this analysis. Starting at the beam pipe in the central barrel going further outwards, there is first the Inner Tracking System (ITS), followed by the Time Projection Chamber (TPC), the Transition Radiation Detector (TRD) and the Time-of-Flight (TOF) detector, all of them will be described in more detail in the following chapters. Information about the detectors are taken from [38], [39], [40], [41] and [42].

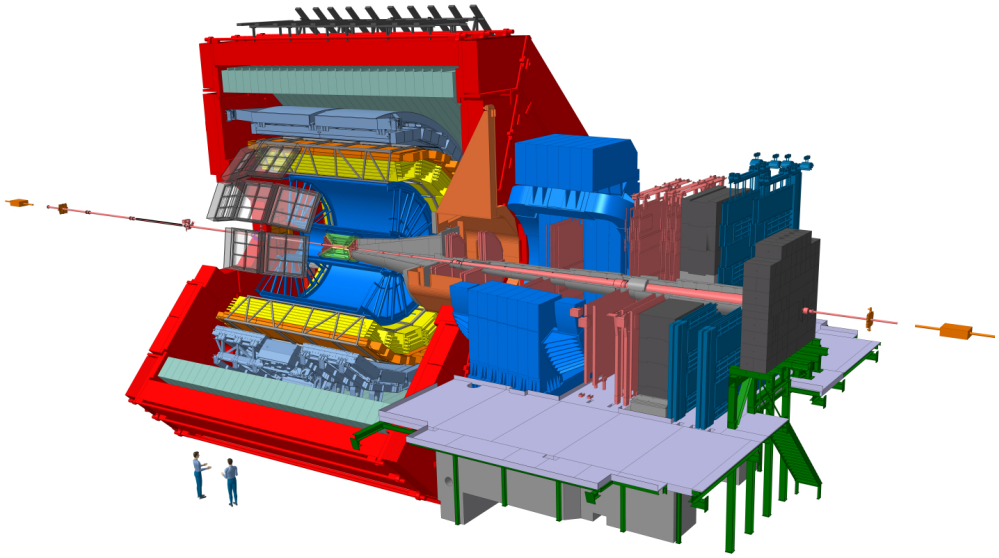

Figure 2.1: The detectors of the ALICE experiment are shown schematically. Inside the solenoid magnet (red) is the TOF (orange), the TRD (yellow), the TPC (blue) and the ITS (green) [43].

2.4 ITS

The most inner detector, with a radial distance from 4 cm to 44 cm to the beam pipe center, is the Inner Tracking System (ITS) [38]. It is made of in total six silicon detector layers, the first two are part of a Silicon Pixel Detector, the next two are a Silicon Drift Detector and the outer two belong to a Silicon Strip Detector. Its basic functions are determination of the primary vertex, particle identification and tracking especially for low-momentum particles, detection of charm decays e.g. for the D^0, as well as improvement of the momentum and angle measurements of the TPC.

2.5 TPC

The ALICE Time Projection Chamber (TPC) is the main tracking device. It has to cope with an environment of unprecedented densities of charged particles, needs to cover the full azimuth and provide a good acceptance in pseudo-rapidity [39]. Besides tracking, the TPC is used for particle identification and therefore has to provide excellent momentum and energy-loss resolution while running at high rates. The main part of the detector is a hollow cylinder, aligned with the beam axis and parallel to the magnetic field – see Figure 2.2, filled with a counting gas consisting of a Ne-CO_2-N_2 mixture at atmospheric pressure. The radius of this cylinder reaches from about 85 cm to 250 cm and its length in beam direction is 500 cm. A conducting electrode at the center of the cylinder is charged to 100 kV and provides an axial electric 'drift' field of 100 kV/250 cm = 400 V/cm. If a particle traverses the cylinder, it ionizes the gas molecules and due to the electric field,

the generated electrons drift towards the endplates with approximately constant drift velocity because of scattering with gas molecules. Multi-wire proportional chambers at the endplates can detect the two-dimensional particle track via pad readout and the z-component (coordinate in beam direction) is reconstructed using the arrival time. In general, the output signal of the readout pads is proportional to the energy loss per unit length of the traversing particle, so subsequently a particle identification (PID) can be done based on the Bethe Bloch formula [44]:

$$-\frac{\mathrm{d}E}{\mathrm{d}x} = Kz^2\frac{Z}{A}\frac{1}{\beta^2}\Big[\frac{1}{2}\ln\frac{2m_e c^2\beta^2\gamma^2 W_{max}(M)}{I^2} - \beta^2 - \frac{\delta(\beta\gamma)}{2}\Big] \tag{2.1}$$

that can be rewritten in parametrized form

$$\frac{\mathrm{d}E}{\mathrm{d}x} = \frac{P_1}{\beta^{P_4}}(P_2 - \beta^{P_4} - \ln(P_3 + \frac{1}{(\beta\gamma)^{P_5}})). \tag{2.2}$$

However, there are some prerequisites for a good $\mathrm{d}E/\mathrm{d}x$ calculation and a satisfactory particle identification: the gain of the readout channels has to be equalized, the momentum of the particle has to be measured and all parameters of the Bethe-Bloch formula have to be known. These parameters can be fixed if the gas mixture and pressure are known. In order to determine the gain of each individual readout channel (of in total 560000), calibration runs where done, during those radioactive krypton ($^{83\mathrm{m}}$Kr) was released in the TPC gas system. Krypton decays most probably to a distinct level, so the emitted electrons have a defined energy loss which causes a main krypton peak. The mean of a Gaussian fit to the main peak for each pad is used as definition for the individual pad gain. In total an energy resolution of around 5% can be achieved, including systematic uncertainties like gain calibration and gas pressure. The procedure how PID is done, using the measured energy loss, and which separation between particles can be achieved, will be discussed in more detail in section 3.1.

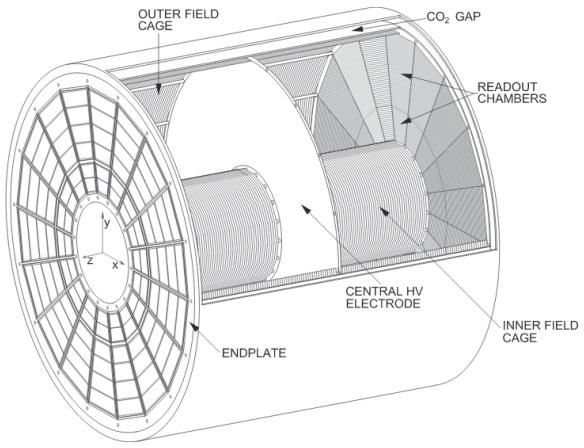

Figure 2.2: Schematic view of the ALICE TPC – taken from [45]

2.6 TRD

A transition radiation detector measures radiation which is emitted when a highly relativistic charged particle crosses many layers of thin materials with different di-electric constants [41]. In general, the detector is divided into four parts: a radiator region, a drift region, an amplification region and the readout part. The drift and amplification regions are both filled with gas. If a highly relativistic particle crosses the boundary between two media of different dielectric constants, a photon can be emitted whose energy depends on the Lorenz factor γ. This photon generates – in addition to the particle – clusters in the gas that drift towards the amplification region and are detected. Because the photon is absorbed most distant from the amplification region, its cluster will arrive there last which causes a second peak which allows one to distinguish between highly relativistic electrons/positrons and other 'slower' particles like pions that do not produce transition radiation. Apart from the transition radiation, which actually does not play an important role in the most current measurements, the TRD works similarly to the TPC: Charged particles ionize the gas, produced electrons drift towards the pad plane, they are amplified and their position is detected. Combined with temporal information, this allows 3-dimensional track reconstruction. In total the ALICE TRD consists of 521 detector moduls, each containing a radiator and a readout chamber. They are ordered in 18 supermodules in azimuthal direction which are subdivided into 5 stacks in beam direction, each of them consisting of 6 detector layers.

2.7 TOF

The main goal of the ALICE time-of-flight detector is to identify charged particles in the intermediate momentum range by measuring the time-of-flight [42]. Together with the

momentum and track length, obtained from tracking detectors, it is possible to calculate the particle mass m (or m^2) – treated in more detail in section 3.2. The TOF is placed outside the TRD, has a cylindrical shape, is also divided into 18 sectors in ϕ and covers polar angles between 45° and 135°. Multigap resistive plate chambers, like the ALICE-TOF, work in the following way: They are made of a stack of resistive glass plates and a high voltage is applied to the external surfaces of the stack. If a charged particle passes through the detector, it ionizes the gas in each gap and due to the high electric field, this ionization is amplified resulting in an electron avalanche. This avalanche is stopped by each plate, however there is a signal induced in the pickup electrodes. By the usage of many plates and a small gap width, high efficiency and good time resolution on the order of 50 ps can be achieved.

2.8 Tracking and secondary vertex finding

Track finding for the ALICE TPC is one of the most challenging parts due to the high-density of produced particles. It is based on the Kalman-filtering approach [46]. A detailed description of the Kalman filter exceeds the limits of this chapter but the principle is explained in section 2.8.1 based on [47] and [48].

2.8.1 Kalman filter

Generally the Kalman filter uses the prior knowledge of a state, including estimates of unknown variables and statistical noise or other inaccuracies. The algorithm can be divided into two repetitive processes: the prediction step and correction step. Firstly, the knowledge of the prior state is used to estimate the current state variables along with their uncertainties. Then in the following step, the outcome of the next measurement is compared to the predictions and by using a weighted average between them, the current state is updated. The algorithm is used recursively, so the updated current state is used as prior state in the next cycle. There are lots of advantages using a Kalman filter approach for tracking: Simultaneous track recognition and fitting can be done and incorrect space points can be rejected in the tracking process. Furthermore, it is a good way to extrapolate tracks from one detector to another. Some disadvantages are that due to high occupancies of up to $\approx 40\%$ in the detector, some clusters may overlap and therefore some are lost and others are significantly displaced which is hard to take into account by the Kalman filter. Moreover, the algorithm relies on good 'seeds' to start a stable filtering procedure but these seeds have to be constructed using TPC data themselves. This is described in the next section 2.8.2.

2.8.2 TPC seed finding

In general, tracking in the ALICE TPC in combination with the ITS is described in [48] respectively [36] and will be summarized in the following. It starts with a seed finding procedure for primary and secondary tracks.

Primary tracks

For primary tracks two space points in defined pad rows (outer row i and inner pad row j) are used as 'track seeds'. These points combined with the primary vertex, whose position is reconstructed with high precision from ITS hits, define the parameters of a helix going through these points – see Figure 2.4. These parameters are taken as an initial approximation of the parameters of the potential track. Then a Kalman filter is started from the outer point to the inner one. If enough points in between the two starting points are associated with the track, then it is stored as a seed. This procedure is repeated by looping over all cluster combinations in the two pad rows. The described method is most efficient for primary tracks, because demanding that that the initial helix goes approximately through the primary vertex penalizes secondary tracks. However, only for the first approximation, this moderate vertex constraint is used and later on

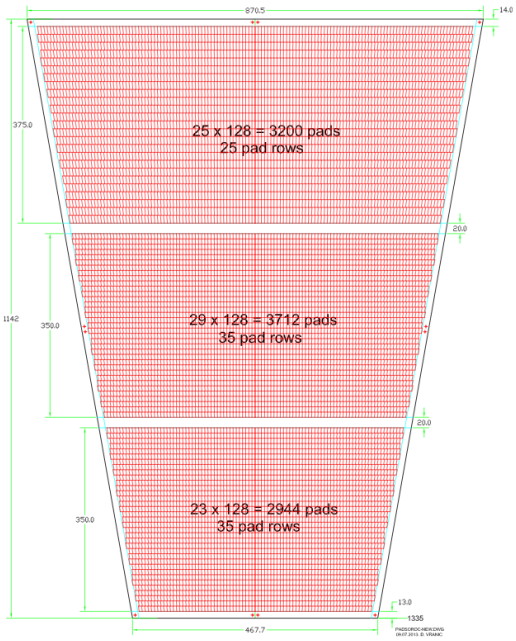

Figure 2.3: A TPC outer readout chamber with pads – taken from [49].

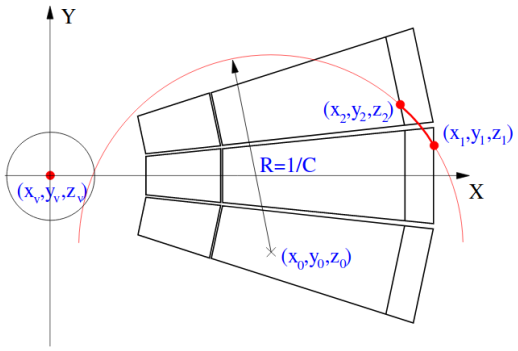

Figure 2.4: Schematic illustration of the combinatorial seeding procedure (mainly) for primary tracks. The primary vertex $\vec{x_v}$ together with one cluster from pad row i ($\vec{x_1}$) and one from pad row j ($\vec{x_2}$) define the initial parameters of a helix. A big uncertainty is added to the primary vertex position, so only a moderate vertex constraint is applied. Accordingly the helix (red) does not exactly go through the primary vertex. Taken from [48].

tracks are allowed to have any impact parameter. Accordingly, also some secondary tracks can be reconstructed by this method, although the next described procedure is more suitable.

Secondary tracks

Contrary to the procedure described in section 2.8.2, another seed-finding strategy without primary vertex constraint is used here. Therefore, for each cluster in the middle pad row $k = \frac{i+j}{2}$ the two nearest clusters in the neighboring detector layers $k+1$ and $k-1$ are found and a straight line fit is applied. Then the line is prolonged to the next pad rows $k+2$ and $k-2$, where again the nearest clusters are found and the fit is updated. If more than seven clusters are assigned to the track, then the fit is replaced by a polynomial and the algorithm continues until the pad rows i and j are reached. In order to increase the efficiency of seed finding, the procedure is repeated for various pad row combinations.

2.8.3 Track following

After finding all seeds, the whole track is reconstructed by the following algorithm for several tracks in parallel [48] (based on the Kalman algorithm described in section 2.8.1):

- For each track candidate the prolongation to the next pad-row is estimated.
- The nearest cluster is found.
- According to the deviation of the cluster position from the track and the cluster parameters, the track is updated.
- Track hypotheses which share too many clusters are removed.

This procedure is continued down to the last pad-row or until the track is lost or ended (for secondary tracks). In the step of prolongation of the track, one has to take into account multiple scattering and mean energy loss, which is done by adding the corresponding matrix to the track covariance matrix and considering the Bethe-Bloch formula assuming the particle is a pion. The next cluster then is searched within a window whose width is set to $\pm 4\sigma$ where σ is calculated according to the track covariance matrix and expected cluster position errors. Because the same track could have been seeded many times, an additional value, the 'overlap factor' is calculated as ratio of shared clusters between two track candidates and the number of all clusters. If this factor exceeds a given value, then the track candidate with higher χ^2 or lower number of assigned tracks is removed, which is a compromise between maximal track finding efficiency and minimal number of multiply reconstructed tracks. After the algorithm is finished, the tracking in the ITS takes over and the track is prolonged as close as possible to the primary vertex, assigning additional precisely reconstructed ITS clusters. Afterwards, one tries to recover tracks that were not found in the TPC for example because of dead zones between the TPC sectors or decays. Therefore an ITS stand-alone tracking procedure is applied to the non-used ITS clusters. Then the tracking is

restarted for all tracks beginning at the primary vertex to the outer layers of the ITS and then continued towards the outer radius of the TPC. The estimated track parameters are now good enough to extrapolate the track towards the outer detectors.

2.8.4 Secondary vertex finding

This section is based on chapter 5.1.7 of [36]. A V^0 consists of two secondary tracks, a positively charged and a negatively charged one (in the following abbreviated as positive/negative track), so the first step is to eliminate all tracks which have a too small impact parameter with respect to the primary vertex – see Figure 2.5. For positive and negative tracks two different cuts for the impact parameters b+ and b- are applied. Then each pair of positive and negative secondary track is considered as V^0 candidate. If the distance of closest approach (dca) between the tracks is larger than a given value, then this V^0-candidate is rejected. The dca is calculated by performing a numerical minimization using a 3-dim helix parametrization for each track. A 'good', 'non-fake' V^0 must fulfill the following criteria:

- consist of secondary daughter tracks, so b+ and b- are large enough
- dca between tracks and V^0 is sufficiently small
- daughter track parameters should be known precisely
- momentum should point back towards primary vertex if V^0 is assumed to be associated to decaying primary particle

The reconstruction quality depends strongly on the radial position of the V^0, the number of hits in the ITS (from zero to six) and the applied cuts like $b_{+/-} > b_{min}$ and dca $<$ dca_{max}. If one restricts a V^0 to be within the narrow fiducial zone of 0.9 to 2.9 cm distance to the primary vertex, and demands that the tracks have six hits in the ITS, then this allows applying tight reconstruction cuts because the track parameters are determined with a very good precision. Furthermore if $R < 2.9$ cm, then the reconstruction is limited to the region within the beam pipe and background coming from secondary interactions in the material is avoided [36].

However, in this thesis we are mainly interested in studying just these interactions – see chapter 4 and chapter 5. Therefore all TPC tracks are used without radial limitation and regardless of the number of ITS hits. Accordingly, the background increases due to combinatorics as well as nuclear interactions and track parameters are not known precisely which causes requires more severe cuts to be applied in order to get a sufficient S/B ratio for the reconstruction of any neutral particle.

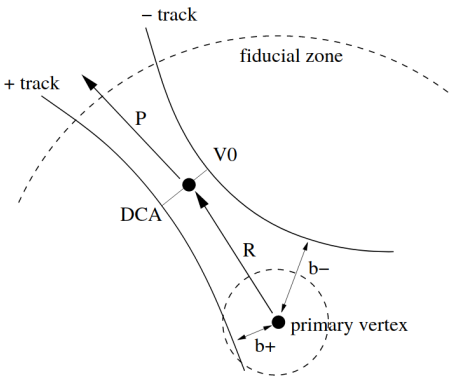

Figure 2.5: Illustration of a V^0 with important quantities – taken from [36].

3 Particle identification

In chapter 2 the construction and functionality of each detector was explained. In the following the output of these detectors is used to identify particles, by measuring their energy loss and time-of-flight. As described in section 1.6.3, it will not be possible to detect the S directly, therefore the reaction products, which may be pions, kaons, protons, K^0_S mesons and Lambdas (or their corresponding antiparticles), have to be identified with high purity. In this chapter, the possibilities of particle identification (PID) will be explained, and the efficiency as well as signal-to-background ratio of identified primary and secondary particles will be studied.

3.1 PID via energy loss in the TPC

A general way in ALICE to identify particles is measuring their characteristic energy loss per unit path $\mathrm{d}E/\mathrm{d}x$ in the TPC [40], given by the Bethe-Bloch formula [44], depending on charge, rest mass, density and momentum. In order to do so, a main prerequisite is that the TPC is calibrated [50], so that the output of the various readout channels is equalized and constant over time, concerning effects like pressure and gas composition dependence, high voltage settings and manufacturing tolerances. As described in section 2.5, this is done using krypton calibration runs. The measurement of $\mathrm{d}E/\mathrm{d}x$ for a track is executed by applying a truncated mean over the maximum number of 159 cluster information, leading to a resolution of about 5% for pp collisions [51]. In order to study how the measured energy loss depends on the momentum and to what extent particle species can be distinguished, $\mathrm{d}E/\mathrm{d}x$ as a function of charge times momentum is considered for p-Pb data TPC tracks. If no further cuts are applied, the result can be seen in Figure 3.1 and Figure 3.2. One can clearly distinguish the particle 'bands' for pion, kaon, proton and deuterium, while tritium is slightly visible. Pions are, as expected, the most frequently produced particles. Depending on the momentum bin, there are overlaps between these bands and especially for high momenta $\mathrm{p} \gtrsim 1.5\,\mathrm{GeV}/c$, pions, kaons and protons can only be barely separated, which will be studied in section 3.2. The same $\mathrm{d}E/\mathrm{d}x$ analysis was also done for Pb-Pb data, which lead to a completely similar result, so the corresponding figures can be found in the appendix – see Figure 8.1 and Figure 8.2. In order to do PID for a given track, the commonly used method is the 'number of sigma' $n\sigma$ approach, indicating the deviation of the measured energy loss to the expected energy loss in terms of the detector resolution [52]:

$$n\sigma_{particle} = \frac{\mathrm{d}E/\mathrm{d}x_{\mathrm{measured}} - \mathrm{d}E/\mathrm{d}x_{\mathrm{spline,particle}}}{\sigma(\mathrm{d}E/\mathrm{d}x)}. \tag{3.1}$$

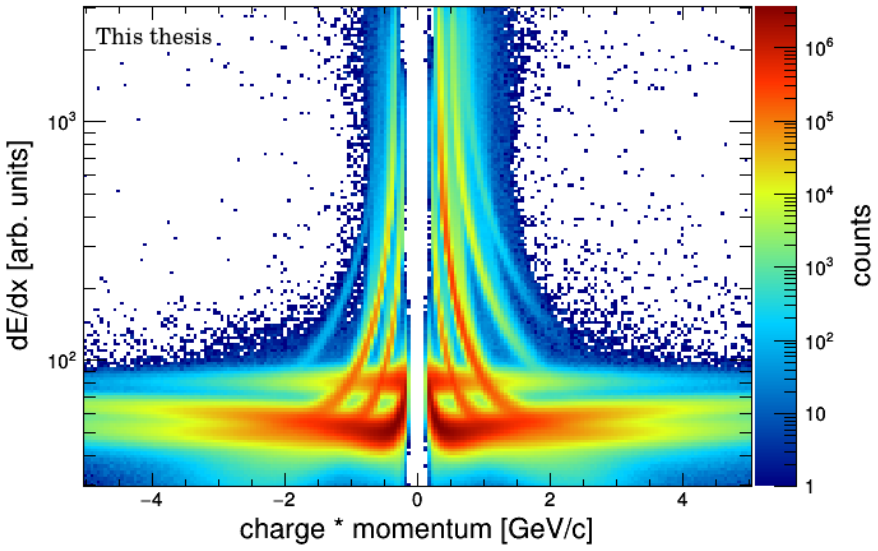

Figure 3.1: Energy loss plotted against charge × momentum for $\sqrt{s_{NN}} = 5\,\text{TeV}$ p-Pb data TPC tracks. The electron, pion, kaon, proton and deuterium 'bands' are clearly visible.

The value of $\mathrm{d}E/\mathrm{d}x_{\text{spline,particle}}$ is obtained from a Bethe Bloch parametrization, corrected for small deviations at low momentum, for each particle species. $\sigma(\mathrm{d}E/\mathrm{d}x)$ is the $\mathrm{d}E/\mathrm{d}x$ resolution, depending on $\mathrm{d}E/\mathrm{d}x$ itself, the number of used clusters for track reconstruction and calculation of the truncated mean, and the pseudorapidity η. Usually, a cut in the range of $n\sigma <$ 2-3 is set, in order to identify a track as corresponding particle species. However, if there is an overlap in $\mathrm{d}E/\mathrm{d}x$, the assignment of a track to a species using the $n\sigma$ cut is not unambiguous, which can lead to misidentification. To prevent this, further methods for PID are needed, as described in section 3.2.

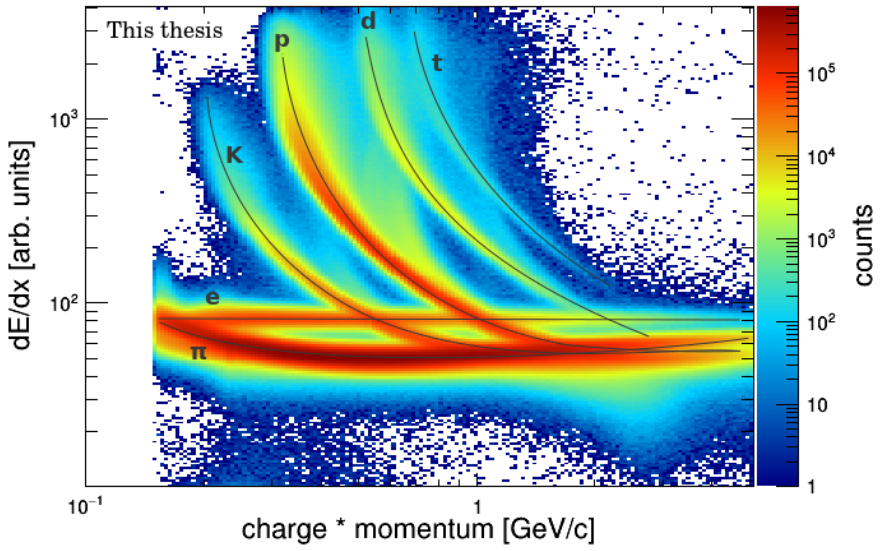

Figure 3.2: Same content like in Figure 3.1 plotted for positive x-axis range with logarithmic scale and bin size. The particle bands are indicated by drawn lines.

3.2 PID via time-of-flight

Another option to identify particles is using the TOF signal in order to calculate the mass squared m^2. As described in section 2.7, the TOF detector reaches a time resolution in the 50 ps range and the path length can be calculated by the helix parameters mainly obtained from the TPC. Combining these information, the mass squared m^2 of the particle can be calculated with high precision, using the relation

$$\frac{m^2}{q^2} = \frac{p_m^2}{\gamma^2 v^2}, \tag{3.2}$$

where m is the mass, q the charge, p_m the (measured) total momentum, γ the Lorentz-gamma and v the velocity, that is calculated using the time-of-flight t and the track length L: $v = \frac{L}{t}$. All mentioned quantities are regarded in the lab-frame. Equation Equation (3.2) can be derived from the general definition of 3-momenta $p = \gamma m v$ and γ^2 is calculated via $\gamma^2 = \frac{1}{1-(\frac{v}{c})^2}$. One has to note that the measured momentum p_m depends on q because it is calculated by equalizing Lorentz and centripetal force, inserting the bending radius r of the track, which gives the following equation:

$$p_T = 0.3 q r B \tag{3.3}$$

for r in meter, transverse momentum p_T in GeV/c, magnetic field B in T and q in units of e. The total measured momentum p_m is then obtained from p_T by using the direction

of the track. Because q in Equation (3.3) is generally not known and therefore set to one, it holds that $p = p_m \cdot q$, which causes the q^2 in Equation (3.2). For high velocities it is possible that measurement uncertainties lead to a velocity $v > c$ that would result in imaginary masses. To prevent this, not m but m^2 is used.

Systematic uncertainties

Systematic uncertainities in calculating m^2 arise from various factors: Firstly the TOF is calculated by subtracting the event collision time t_{event} from the time t_{TOF} measured with the TOF detector. The latter depends on intrinsic parameters and due to calibration a resolution of $\approx 56\,\text{ps}$ is achieved [53]. For the determination of the event collision time, a method can be used which is based on the TOF information alone [54], and its uncertainty depends on the number of tracks used for the calculation. As shown in Equation (3.3), variations in the magnetic field, and the tracking accuracy, which determines r and L, contribute as uncertainties. Especially for secondary tracks there are other factors that limit the m^2 resolution. If a primary neutral particle decays, this happens with a delay compared to the Pb-Pb (or p-Pb) collision, which is not taken into account in the calculation. The track length is obtained by integrating the path from the closest position to the primary vertex to the TOF, so accordingly not the real path, which originates from the V^0, is determined. To a certain degree this overestimation of TOF and path length cancel out when calculating m^2, however there still remain uncertainties: Firstly the track of the neutral primary particle is not curved in contrast to the used prolongation of the V^0 daughter track. Secondly, the velocity of the primary particle differs from that of the secondary one, resulting in an inaccurate averaged velocity that is used in the m^2 calculation. This effect increases with larger radial distances of the secondary vertex, causing more serious uncertainties in the m^2-determination and also a decrease in efficiency for secondary tracks. Accordingly, one has to consider, that the limited efficiency of the TOF detector leads to a decrease in statistics if strict m^2-cuts are applied for PID.

3.2.1 p-Pb data

The m^2 distribution plotted against charge times momentum for p-Pb data is shown in Figure 3.3a. In a momentum range up to $\approx 2.5\,\text{GeV}/c$, pions, kaons and protons (as well as their antiparticles) are clearly visible and can be distinguished, except for kaons which overlap with pions at around $1.7\,\text{GeV}/c$. The m^2 measurement via TOF-detector can be used to determine how well the $n\sigma$ cuts (also called $\mathrm{d}E/\mathrm{d}x$-cuts) are capable of distinguishing particle species, depending on the momentum bin. As one can see in Figure 3.2, for momenta in the range $0.5 < p < 0.8$ GeV/c, the pion, kaon and proton bands are unambiguously separated. The related m^2 distribution is shown in Figure 3.4a, applying various $\mathrm{d}E/\mathrm{d}x$-cuts. One can see cutting on pions or protons significantly improves the signal to background ratio for these species. If a cut on kaons is applied there still remains a pion background, but the pion peak is clearly separated. Anyway, if a different momentum range $1.5 < p < 2$ GeV/c is chosen, then

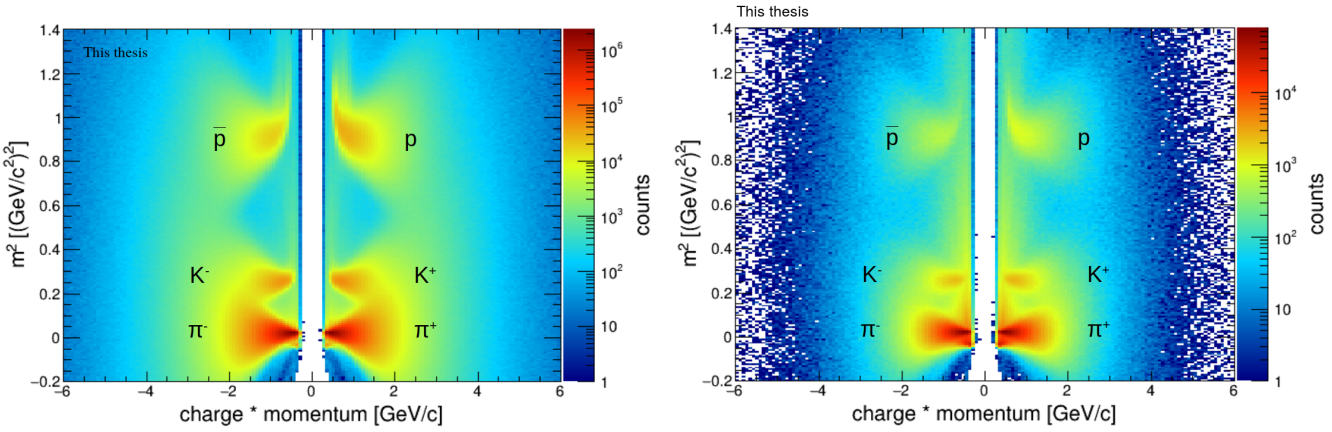

(a) p-Pb data

(b) Pb-Pb data

Figure 3.3: m^2 plotted against charge·momentum. Pions, kaons and protons can be identified in a momentum range up to $\approx$ 2.5 GeV/c. Especially for kaons there is an overlap with pions.

the overlap in dE/dx between all three species is significantly larger – see Figure 3.2. Therefore applying dE/dx cuts for this momentum bin, as shown in Figure 3.5a, does not noticeably improve the signal to background ratio. Accordingly, a PID solely by dE/dx cuts is not possible in this momentum range.

3.2.2 Pb-Pb data

The same analysis as described in section 3.2.1 was done for $\sqrt{s_{NN}} = 5.02\,\text{TeV}$ Pb-Pb data. Comparing Figure 3.3a to Figure 3.3b shows the same general structure, but for Pb-Pb data, the TOF mismatching, which occurs mainly due to photons, seems to be higher, which can be seen by the vertical stripe at very low momenta. In Figure 3.4b one can see that the signal to background ratio for all three particle peaks is lower than for p-Pb, especially if no dE/dx cut is applied. Cutting on pions and protons provides a satisfying particle separation, but if one cuts on kaons, there are by a factor of about 5 more pions remaining than the desired kaons. For momentum bin 2, no sufficient particle separation is possible by solely applying $n\sigma$ (dE/dx) cuts.

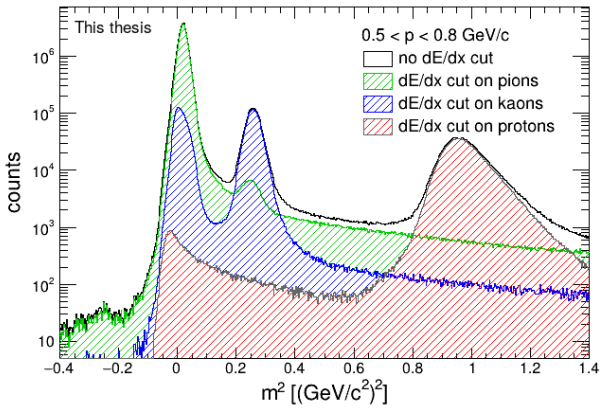

(a) p-Pb

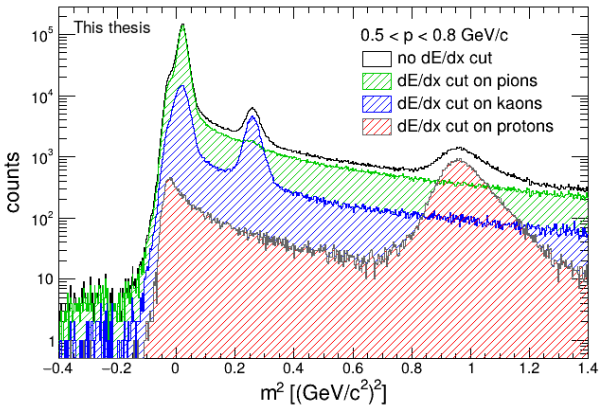

(b) Pb-Pb

Figure 3.4: m^2 distribution of particles in the momentum range $0.5 < p < 0.8$ GeV/c (momentum bin 1), dE/dx cuts for identifying pions, kaons and protons are applied separately.

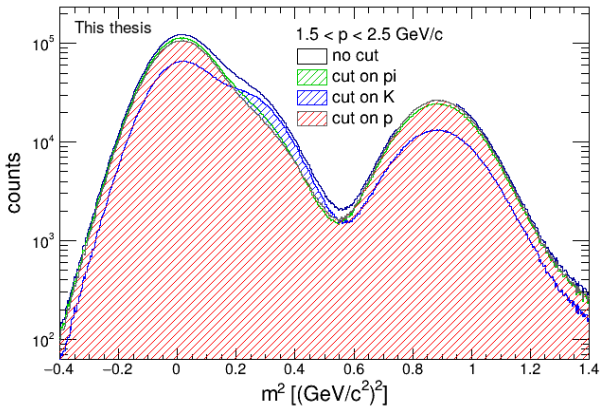

(a) p-Pb

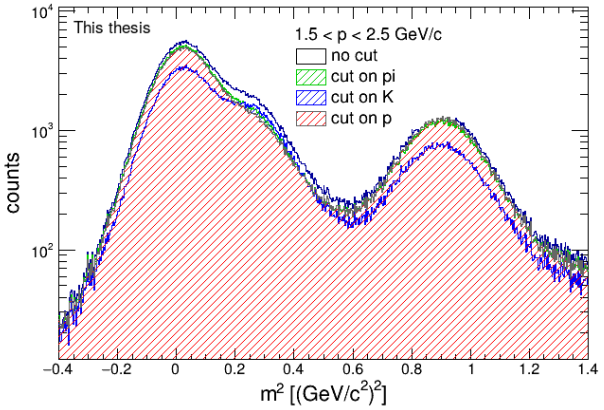

(b) Pb-Pb

Figure 3.5: m^2 distribution in the momentum range $1.5 < p < 2.5$ GeV/c (momentum bin 2). Applying dE/dx cuts for each particle species does not achieve satisfactory PID.

3.3 PID by invariant mass

Previously, the PID for stable, charged particles was discussed, but there are also unstable and neutral particles which can only be detected via their decay products. Commonly, these particles are identified by reconstructing secondary vertices (V^0s), cutting on dE/dx for the secondary daughter tracks, demanding them to be the desired species of the decay products (sometimes using additionally m^2 cuts), and calculating the invariant mass of the decaying particle. This is done by adding up their four-momenta, using the measured momentum vector, determined at the secondary vertex position, and setting the mass to the literature value of the corresponding species. The invariant mass histograms can be evaluated using Gaussian fits combined with background fits, resulting in an estimation of the signal-to-background ratio and the width of a peak. In the following, this will be discussed for neutral kaons (K^0), (Anti-)Lambdas (Λ^0), Xi's (Ξ^-) and Omegas (Ω^-).

3.3.1 Kaons K^0

Neutral kaons exist in two physical states K^0_S and K^0_L, with lifetimes differing by a factor ≈ 600. Therefore the decay length $c\tau \approx 15\,\mathrm{m}$ of the K^0_L is way to high to detect them regularly, so only K^0_S mesons are usually observed, decaying within a decay length of $c\tau \approx 2.8\,\mathrm{cm}$ mainly into π^+ and π^-. These charged particles can be tracked, identified via dE/dx-cuts and their origin, the vertex V^0, is reconstructed using the V^0 finder. Summing up the four-momenta of these two pions for each V^0: $p_4 = p_{\pi^+} + p_{\pi^-}$ and calculating the invariant mass $m = \sqrt{p_4^2}$ results in the invariant mass distribution shown in Figure 3.6. For p-Pb data, including primary K^0_S mesons, a clear peak is visible with a mean value of $\mu = 0.498\,227\,\mathrm{GeV/c^2}$ which is compatible with the literature value of $m_{K0,lit} = 0.497611 \pm 0.013$ GeV/c^2 [55] within 1σ. One has to keep in mind that the K^0 as well as its antiparticle $\overline{K^0}$ may be produced in strong interactions as strong eigenstates. However, they decay as weak eigenstates (K^0_S and K^0_L), which are quantum mechanical mixtures of K^0 and $\overline{K^0}$. Accordingly, it is not possible to determine if the original strongly produced particle was a K^0 or $\overline{K^0}$ by considering the decay.

3.3.2 Lambdas, antilambdas

The Lambda baryon Λ decays with a probability of nearly 100% into one nucleon and pion. In that process there is a 63.9% chance for decaying into proton and π^-, which are both detectable. Therefore the Lambda mass can be reconstructed by finding V^0's, consisting of protons and π^- (using dE/dx cuts), adding their four-momenta and calculating the invariant mass. Analogously, antilambdas decay mainly into antiproton and π^+, so the reconstruction is done in the same way. The result for Lambdas and antilambdas combined can be seen in Figure 3.7. Even without any further PID or topology cut, the peak that corresponds to Lambdas can be clearly resolved over the background and a value for the mass $m_{\Lambda,exp} = 1.115718 \pm 0.001484$ GeV/c^2 is obtained.

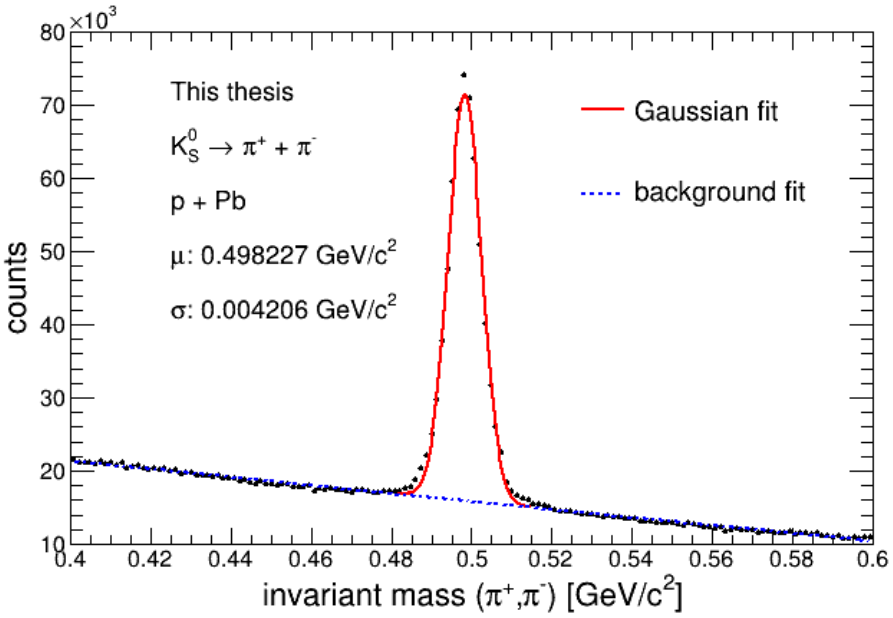

Figure 3.6: Invariant mass distribution for secondary vertices with $\mathrm{d}E/\mathrm{d}x$ selected pions as daughter particles. A Gaussian plus linear background fit was applied.

This is in very good agreement with the literature value of $m_{\Lambda,lit} = 1.115683 \pm 0.006$ GeV/c^2 [56] within 1σ.

3.3.3 Xi baryon

The Ξ baryons are doubly strange carrying baryons with quark content dss (Ξ^-), $\overline{dss}$ (Ξ^+) or uss (Ξ^0). The Ξ^- decays with nearly 100% probability into Λ and π^-. Due to the second decay of the Lambda into proton and π^-, the Xi is also denoted cascade particle. All final charged particles can be detected and therefore the Ξ is reconstructed and its invariant mass is determined. The reconstruction happens in the following way: A V^0 is found consisting of proton and π^- as daughters, that are identified by using $\mathrm{d}E/\mathrm{d}x$ cuts – analogous as in section 3.3.2. Then the momentum vector of this V^0, which corresponds to a decaying Λ, is calculated and a backtracking straight in the direction of the momentum is performed. Regarding all other tracks in this event, one is searched that has a dca $< 0.5\,\mathrm{cm}$ to this straight. Finally, the total four-momentum and invariant mass can be calculated. The result is shown in Figure 3.8: The peak at approximately $1.322\,\mathrm{GeV}/c^2$ definitely corresponds to the Ξ^- with a literature value of $m_{Xi,lit} = 1.321\,71\,\mathrm{GeV}/c^2$ [44]. In the following analysis the Ξ will not be regarded any more, which is the reason why no more detailed study was done. Our goal was mainly to show that we are able to reconstruct a doubly strange particle because this is to some extent similar to the S in terms of topology.

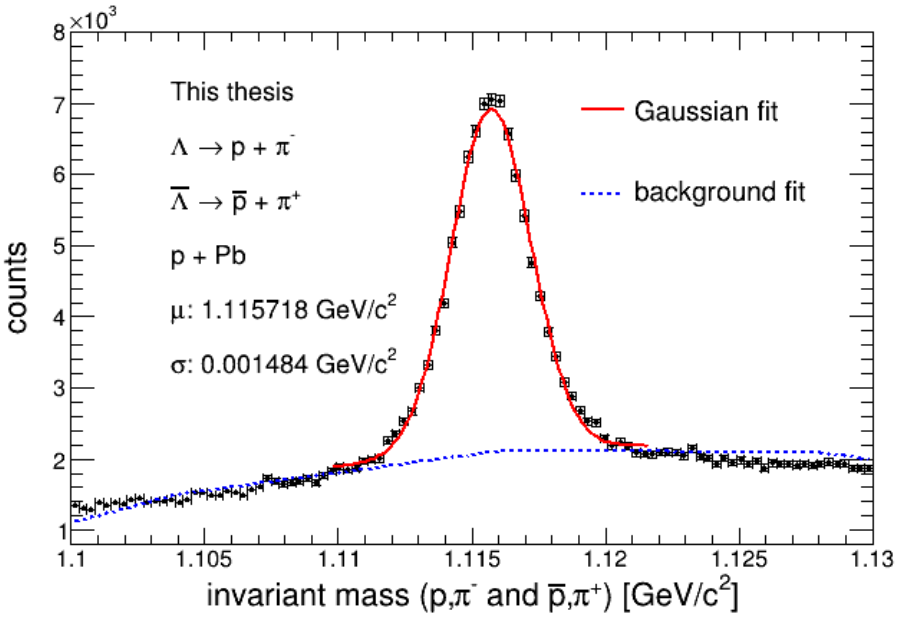

Figure 3.7: The invariant mass distribution for secondary vertices made of $\mathrm{d}E/\mathrm{d}x$ selected p and π^- or $\overline{\mathrm{p}}$ and π^+ is shown.

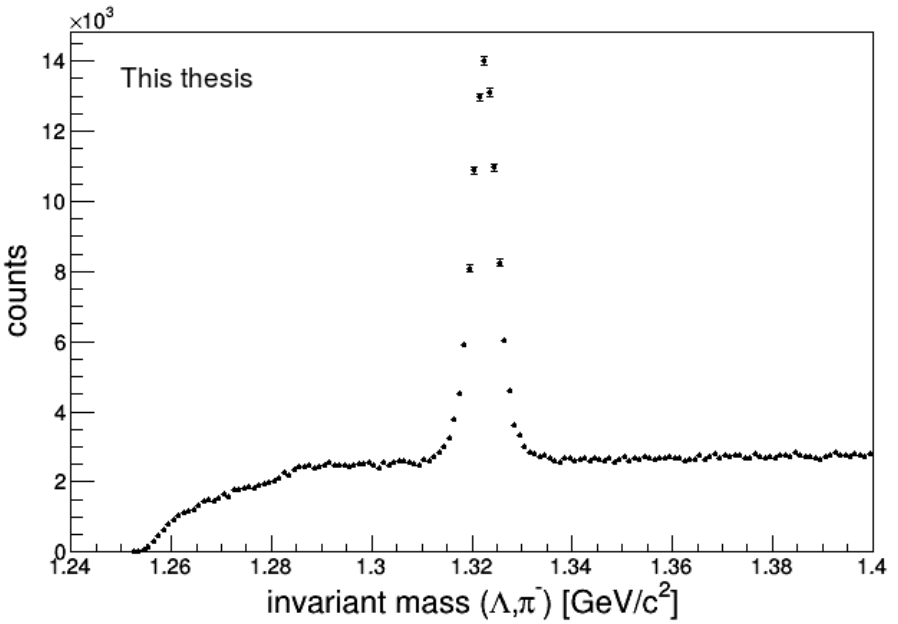

Figure 3.8: The invariant mass spectrum for V^0s made of Λ and π^- is depicted for p-Pb data.

3.3.4 Omega baryon

The Ω^- baryon was detected 1964 in Brookhaven and, with a quark content of sss, it is the only known particle, consisting of three heavy quarks of the same flavour. Moreover, there exist the heavy baryons Ω_c^0 and Ω_b^-, for which, compared to the Ω^-, one s quark is replaced with a charm respectively bottom quark. The most likely decays of the Ω^- are the decays into $\Lambda^0 + \mathrm{K}^-$ or $\Xi^0 + \pi^-$. The first of them will be considered in the following. The reconstruction procedure is analogous to the one described in section 3.3.3, replacing the π^- with a K^-. The invariant mass spectrum is shown in Figure 3.9 and, as the peak at around $1.673\,\mathrm{GeV}/c^2$ indicates, we are capable of reconstructing the Ω^- which has a mass of $m_{\Omega,lit} = 1.672\,45\,\mathrm{GeV}/c^2$ [44]. The purity could be improved by applying m^2 cuts for the decay products because especially the kaon shows an overlap in $\mathrm{d}E/\mathrm{d}x$ as discussed in section 3.2. Furthermore it could be excluded that the daughter particles originate from the primary vertex by demanding a sufficiently high dca. Moreover, there are other topological cuts considering angles and distances that could be applied. Anyway, as already mentioned in the previous chapter, our aim was not to study Ξ's and Ω's in detail but only to show that we can reconstruct them.

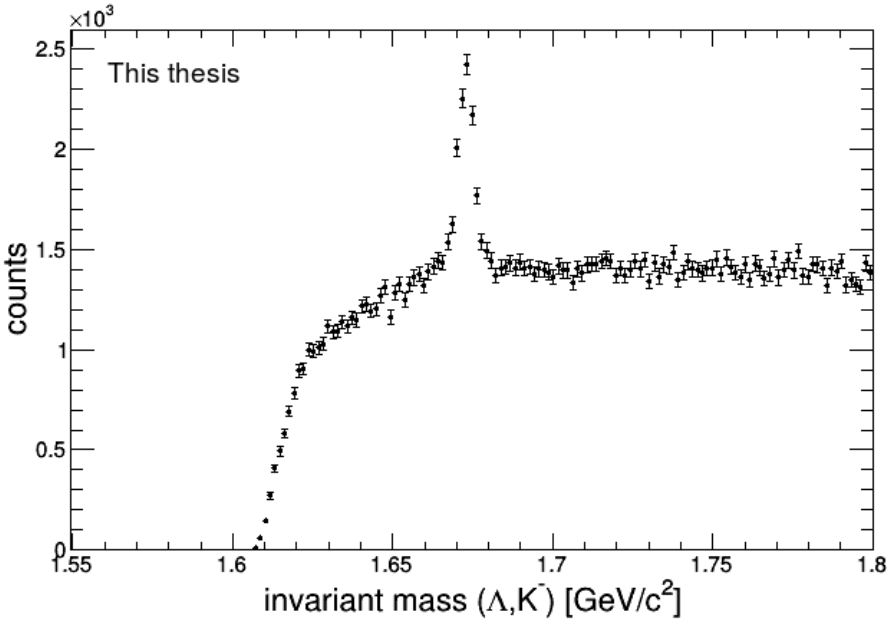

Figure 3.9: Invariant mass distribution for secondary vertices made of Λ and K^- for p-Pb data.

3.4 Radial dependence study

In this chapter it will be examined how the number of primary and nonprimary Lambdas, antilambdas and K^0_S mesons changes depending on the distance to the primary vertex (called radius r). The term 'particle' will in this context be used representing Lambdas, antilambdas and K^0_S mesons simultaneously. This dependence is of interest because in chapter 5 the mentioned neutral particles have to be identified as daughters of nuclear S interactions which will be considered especially for larger radii. Therefore it is reasonable to study the frequency of these particles in combination with their S/B ratio individually for primary, secondary and all particles as a function of the radius. In particular it can be studied how the number of primary particles changes due to their decay, and to what extent primary particles might contribute as a background source for the identification of secondary ones. In order to do so, an invariant mass spectrum like the one described in section 3.3.2 and section 3.3.1 was determined for $r > r_{\mathrm{min}}$ with r_{min} in steps of 1 cm in a range of 0 cm to 70 cm. For the daughter $\mathrm{p}/\bar{\mathrm{p}}$ of the $\Lambda/\overline{\Lambda}$ an additional m^2 cut is applied. Then for each spectrum a Gaussian combined with a second order polynomial fit was performed – an example with $r > 10$ cm for Lambdas can be seen in Figure 3.10. In order to assure stability of the fit, the background fit was done first, using the range directly besides the peak, then the parameters of the second order polynomial were fixed and after that the Gaussian fit was done. The same procedure is repeated for neutral particles whose backtracking momentum vector has a dca to primary vertex $\mathrm{dca_{PV}} < 0.5$ cm, in the following called 'primary' particles – shown in Figure 3.11a for Lambdas with $r > 10$ cm; similar figures for antilambdas and kaons can be found in the appendix. Moreover, it is also done for nonprimary particles which will be of importance in chapter 6. Because neutral particles, decaying within small radii, produce daughter particles that can be tracked very precisely, due to up to 6 hits in the ITS layers, for them only a small $\mathrm{dca_{PV}}$ cut has to be applied. In contrast, more outer produced daughter tracks are not necessarily that precise and even small changes in the reconstructed momentum vector might cause, due to the distance from the primary vertex, a significant change in $\mathrm{dca_{PV}}$ even if the track is primary. To prevent misidentification of secondary neutral particles, a radially linear dependent $\mathrm{dca_{PV}}$ is used, demanding that $\mathrm{dca_{PV}} > \mathrm{dca_{min}}$. We defined the condition that for $r = 5$ cm it holds $\mathrm{dca_{min}} = 0.5$ cm and for $r = 25$ cm it applies $\mathrm{dca_{min}} = 2$ cm, with a linear interpolation between this points.

Integrating the difference between Gaussian and background in a 2σ range gives us the number of particles. This number is then plotted against the applied radius cut for each particle species and for primary, nonprimary and combined particles individually.

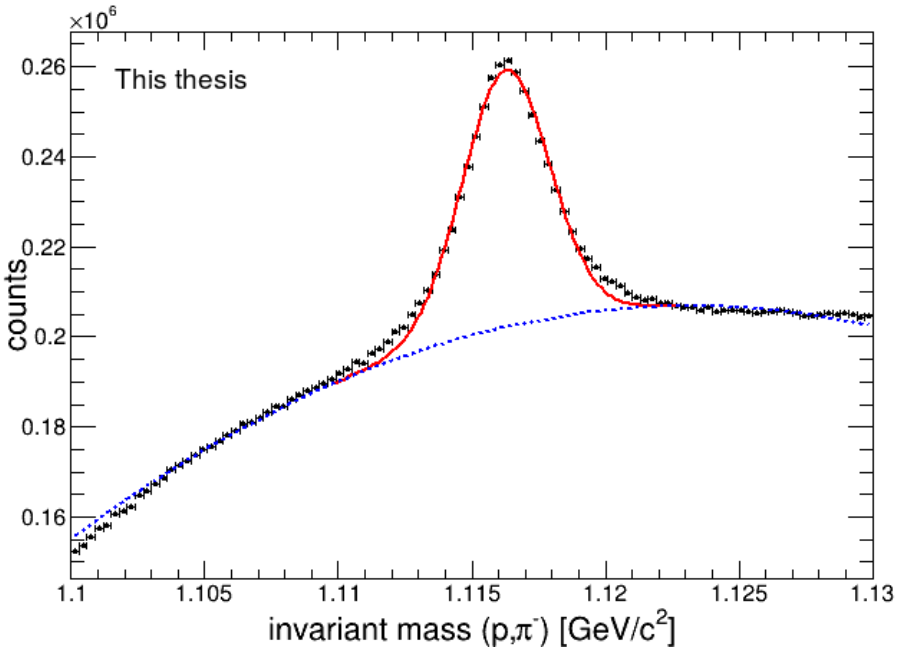

Figure 3.10: Invariant mass distribution of p and π^- with $r > 10\,\text{cm}$ for Pb-Pb data.

3.4.1 Lambdas

The above described procedure was done for Lambdas. Comparing Figure 3.11a to Figure 3.10 shows that primary Λ's contain less background. Regarding Figure 3.11b, one can conclude that even for small radii it is a challenge to reconstruct true secondary Lambdas due to the dominating background. This will remain a difficulty in the main part of this thesis – chapter 5. The polynomial fit in Figure 3.11b is only important to describe the background below the Gaussian, so the deviation for smaller masses is not significant for analyzing the number of particles. One can conclude from the tail of the Gaussian that the peak is not exactly described by a Gaussian, however, for a qualitative study this is acceptable.
As expected, if one increases the radial restriction, the number of (primary, secondary and total) Λ's decreases, which can be seen in Figure 3.13. A set of example invariant mass histograms for various radii, which contribute to the numbers in Figure 3.13, can be found in the appendix, see Figure 8.3. Primary particles are more frequent than secondary ones, however, the latter do not completely vanish. The difference between total and primary particles does not result in the number of secondary ones, because we demand stricter cuts for them, as described previously. There might be a contribution of primary tracks in the red curve especially for smaller radii, however, the increasing dca cuts for larger radii should assure that this background source is minimized.

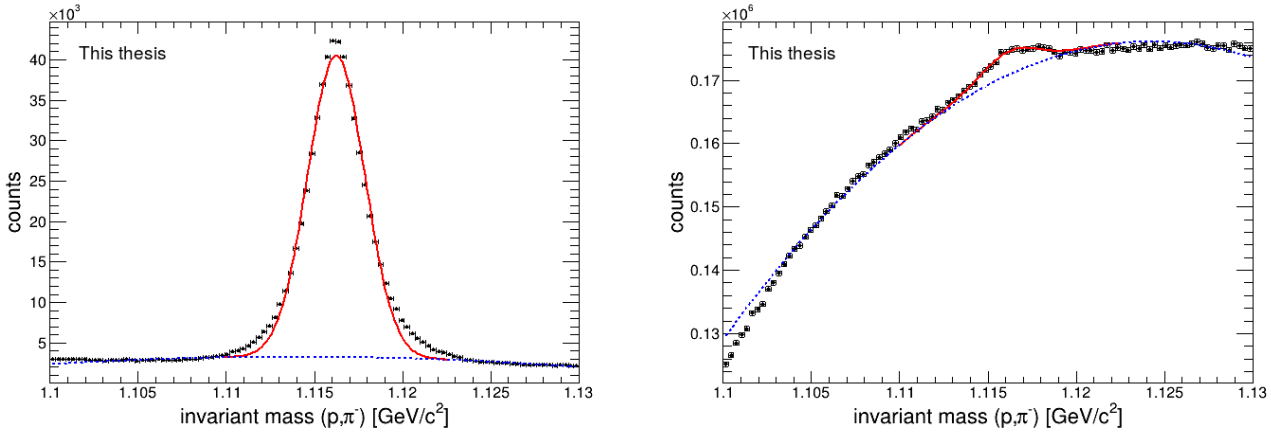

(a) only primary particles

(b) only secondary particles

Figure 3.11: The invariant mass distribution of p,π^- with $r > 10\,\text{cm}$ is shown for Pb-Pb data.

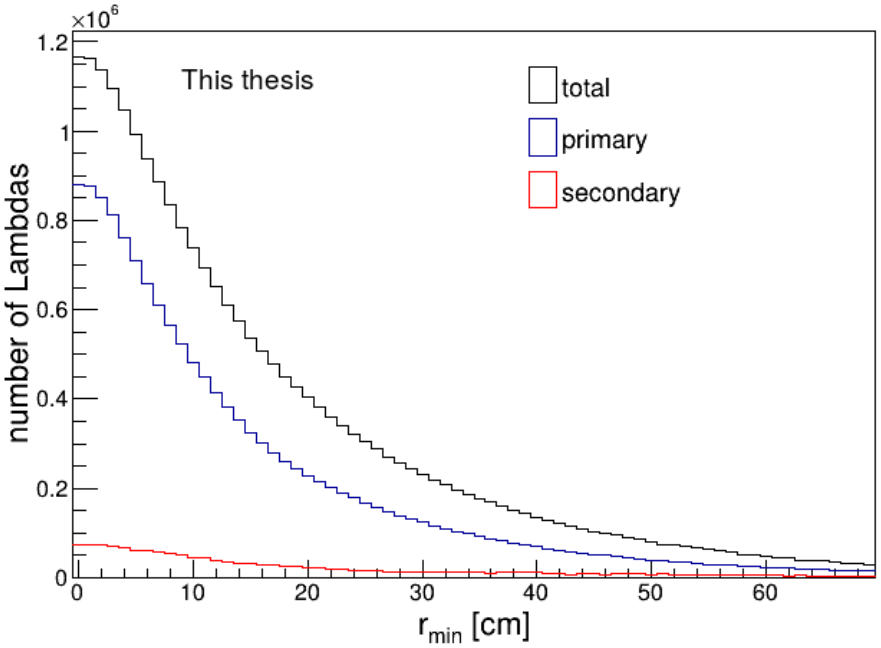

Figure 3.12: The number of total, primary and secondary Lambdas is shown, requiring $r > r_{\text{min}}$ for Pb-Pb data. Further cuts and the procedure of obtaining the numbers are described in the text.

3.4.2 Antilambdas

In general the invariant mass spectra of $\overline{\Lambda}$'s and the radial dependences are quite similar to that of Λ's. Some example invariant mass distributions can be found in the appendix – see Figure 8.4. The signal-to-background ratio for antilambdas is better than for Lambdas which can be seen especially in a comparison of invariant mass spectra of secondary particles – compare Figure 8.3e to Figure 8.4e. A reason for that might be that protons have to be a part of the background contribution for Lambdas. Protons appear more frequently in nuclear interactions than antiprotons because, due to baryon number conservation, their final state can be made of only one baryon. In contrast, if an antiproton is part of the reaction products of a nuclear interactions there usually have to be more baryons in order to assure that the baryon number is conserved and accordingly, this reaction is less favored in phase space. As a consequence, there are much more protons that contribute to combinatorial background in the Λ spectrum than there are antiprotons that affect the $\overline{\Lambda}$. This can generally be seen as an advantage because later on, the study of secondary $\overline{\Lambda}$'s will be important and a sufficiently good signal to background ratio supports further steps of the analysis. Interestingly, the number of $\overline{\Lambda}$'s is of the same order of magnitude but a bit higher than that of Λ's. We know that primary Lambdas/antilambdas are produced in equal amounts in Pb-Pb collisions. The distributions are not corrected for efficiency of any kind which could explain the difference between primary Lambdas and antilambdas.

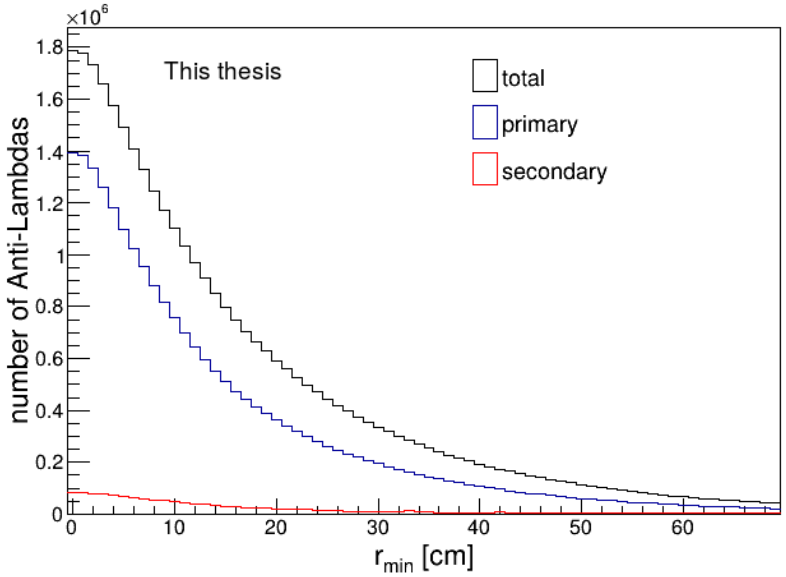

Figure 3.13: Analogous to Figure 3.13 the number of antilambdas as a function of $r_{\min}$ is shown.

3.4.3 Neutral kaons

As displayed in Figure 3.15, the number of total and primary K^0_S mesons decreases faster than for Lambdas, due to the shorter decay length – corresponding example invariant mass distributions for $r > 10\,\text{cm}$ can be seen in Figure 3.14. The fraction of primary K^0_S mesons to total ones is quite high and secondary K^0_S mesons cannot reasonably be reconstructed for $r \gtrsim 15\,\text{cm}$ – this can be seen in Figure 3.15 when the red curve approaches zero, and the corresponding invariant mass histograms do not show a visible peak in that region, e.g. in Figure 8.5f. This does not mean that there are no secondary K^0_S mesons at large radii, but only that the background dominates, supported by the fact that pions are the most frequent particles and accordingly large random combinatorics contribute to the background. In conclusion, we expect that it will be challenging to find secondary vertices at larger radii in chapter 5 which contain K^0_S mesons. On the other hand, it might be possible that for more complicated topologies the background could be decreased and some few K^0_S mesons might become visible which would then be a serious indication for something interesting occurring.

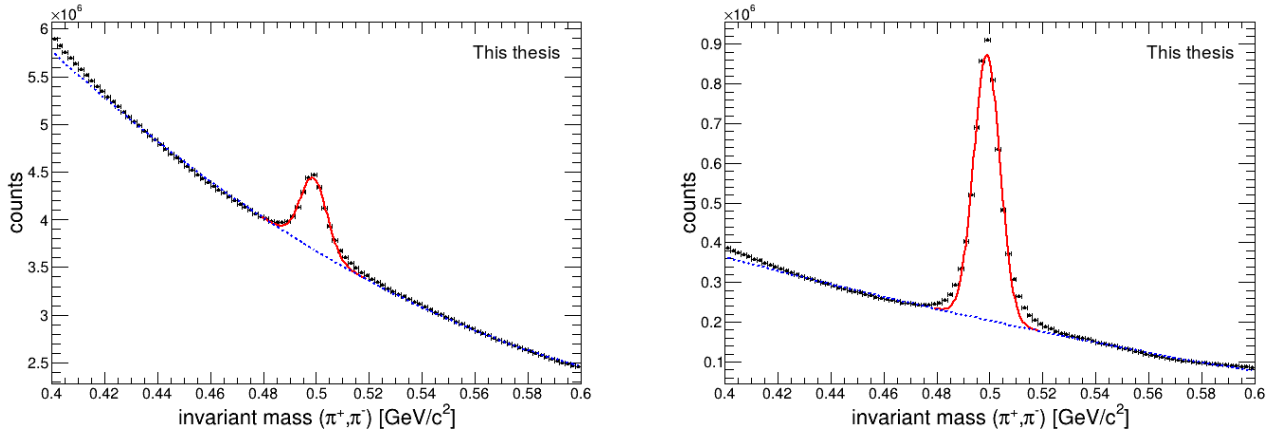

(a) 'all' particles

(b) only primary particles

Figure 3.14: Invariant mass distribution of π^+,π^--vertices with restriction $r > 10\,\text{cm}$ for Pb-Pb data.

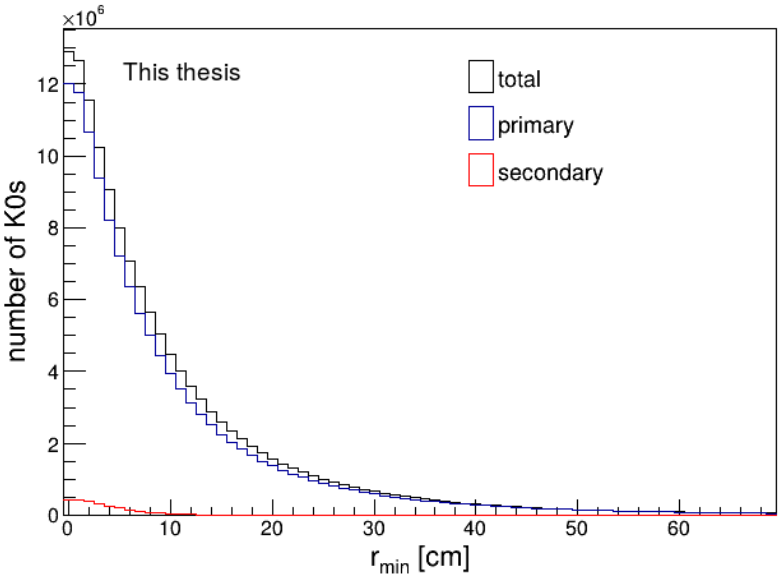

Figure 3.15: Number of K^0_S mesons as a function of $r_{\min}$ for Pb-Pb data.

4 Secondary hadronic interactions

A strategy to find S candidates is detecting its interactions with protons or neutrons in the detector material. Therefore it is reasonable to study general secondary hadronic interactions of primary particles with detector nucleons, in order to be capable of showing that these interactions can be traced. A similar analysis was done for example by Friederike Bock in [57].
The reconstruction is based on finding secondary vertices which is done by a V^0 finder as described in section 2.8. Only V^0s are accepted whose daughter tracks fulfill distinct criteria. To assure that we are observing a secondary hadronic interaction, it is demanded that both tracks are nonprimary, therefore the restriction $\mathrm{dca}_{\mathrm{PV}} > 5\,\mathrm{cm}$ is set. This cut is chosen intentionally quite severe, because our aim is to show that hadronic interactions can be localized and therefore a higher priority to purity than efficiency is given. Furthermore, one has to exclude decaying particles like especially K^0_S, Λ or $\overline{\Lambda}$ and in addition γs have to be excepted. If a V^0 consists of two $\mathrm{d}E/\mathrm{d}x$ selected electrons then it is rejected. If both tracks are decay products of a K^0_S or (anti)Lambda, then the invariant mass is computed and if its inside a 2σ range of the corresponding decaying particle, see section 3.3.2 and section 3.3.1, then the V^0 is rejected. To avoid low momenta curling tracks and high momenta tracks, that wouldn't allow a good PID because of overlapping in $\mathrm{d}E/\mathrm{d}x$, as discussed in section 3.1, only tracks with $0.5 < p < 2$ GeV/c are accepted. The highest density of fake V^0s due to combinatorial background is close to the primary vertex and therefore only vertices with radius $r > 2\,\mathrm{cm}$ were used. For each remaining V^0, additional secondary pions originating from its position are searched by looping over all other tracks. A method to distinguish V^0s due to decays from secondary hadronic interactions would be to demand a higher multiplicity of $N \geq 3$, however many hadronic interactions only result in two tracks, as tested in this work. For all tracks it must hold that they originate from the V^0 and therefore it is checked whether there is an ITS hit associated with one of the two tracks of the V^0 radially closer to the primary vertex than the V^0 position. If so, then the hadronic interaction candidate is rejected. To sum it up, the following cuts are applied:

- radial position of the secondary vertex $r > 2\,\mathrm{cm}$
- $\mathrm{dca}_{\mathrm{PV}} > 5\,\mathrm{cm}$ for all tracks
- 'anticut' on γ: if V^0 daughters are electron and positron then candidate is rejected
- 'anticut' on K^0_S, Λ and $\overline{\Lambda}$: if daughters are decaying products and invariant mass is in 2σ range of decaying particle, then V^0 is rejected
- $0.5 < p < 2$ GeV/c for V^0 daughter tracks

- total number of tracks: $2 \leq N \leq 4$
- dca of all particles to secondary vertex corresponding to a $V^0 < 0.5\,\text{cm}$
- no ITS hit associated to V^0 daughter track radially closer to primary vertex.

In order to verify if a reconstruction of true nuclear interactions in detector material was successful, it is reasonable to study the spatial distribution of these events and compare it to the detector structure. Because of the cylindrical detector symmetry, one main variable of interest is the distance from the z axis – in the following called orthogonal radius $r_o = \sqrt{x^2 + y^2}$.

1D consideration

For each nuclear event vertex which passes all mentioned cuts, the r_o distribution is shown in Figure 4.1. The peaks correspond to ITS layers, see Figure 4.2, and TPC parts as indicated. In the range of around $7 < r_o < 55$ cm there is a significant background structure which will be discussed in the next part. Due to that background, the second ITS layer cannot be resolved, while the first and third are only slightly visible. The inner containment vessel, starting at around 60.6 cm, as shown in Figure 4.6, can be clearly resolved. Likely due to the slightly curved structure of the vessel, the corresponding peak position is at around 62 cm. The TPC inner field cage vessel with TPC rods can be seen by the hadronic interactions, occurring in a range of $75 < r_0 < 85$ cm.

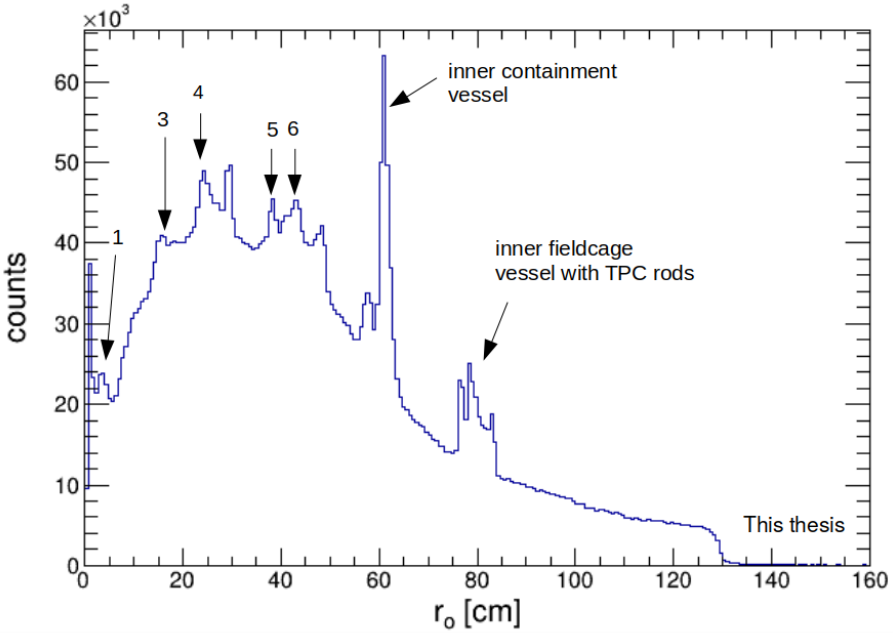

Figure 4.1: Distribution of r_o for p-Pb data in a pseudorapidity range of $-0.8 < \eta < 0.8$. The numbers indicate the ITS layers.

Table 1.2: Dimensions of the ITS detectors (active areas).

Layer	Type	r (cm)	$\pm z$ (cm)	Area (m^2)	Ladders	Ladders/stave	Det./ladder	Tot. channels
1	pixel	4	16.5	0.09	80	4	1	5 242 880
2	pixel	7	16.5	0.18	160	4	1	10 485 760
3	drift	14.9	22.2	0.42	14	—	6	43 008
4	drift	23.8	29.7	0.89	22	—	8	90 112
5	strip	39.1	45.1	2.28	34	—	23	1 201 152
6	strip	43.6	50.8	2.88	38	—	26	1 517 568
Total area = 6.74 m^2								

Figure 4.2: Radial positions of ITS detector layers – taken from [38].

z-r plane

The distribution of secondary hadronic vertices in the z-r plane for p-Pb collisions is shown in Figure 4.3. The general structure of the ITS can be seen, e.g. the fourth detector layer at $r_0 = 23.8\,\text{cm}$ with $\pm z = 29.7\,\text{cm}$. At around 60 cm, the central drum of the inner containment vessel is clearly recognizable. An abnormality is the structure at $|z| \lesssim 20\,\text{cm}$ and $5 \lesssim r \lesssim 40$ cm. In this region there exists material which gives rise to nuclear interactions, however the number of them exceeds the expectation from material budget and furthermore, the detector structure is only fairly patterned. One assumption was that the central HV-electrode might cause interactions due to particles with very small η having a long pathlength through it. However, applying cuts on η did not decrease this structure and the HV electrode is very thin, so there must be another reason for it. Our guess is that primary Ω baryons or cascade particles which decay at around 2.5 cm to 10 cm can create fake nuclear events in that range. This could for example happen if an Ω decays into kaon and Λ, which decays into proton and pion. The track of the proton could be very close to the kaon track which might result in a fake V^0 that would not be excluded by the mentioned 'anticuts'. Moreover, there is increased detector material in that region which could in addition to nuclear events also cause scattering of particles. These scattered tracks could then form fake V^0s and contribute to the background which leads to a blurring in Figure 4.3. One also has to consider that the selection is biased by TPC cluster cuts. For larger η values, the TPC acceptance is exceeded so some clusters are not detected. This is correlated with the abnormal structure which is focused in a small $|\eta|$ range.

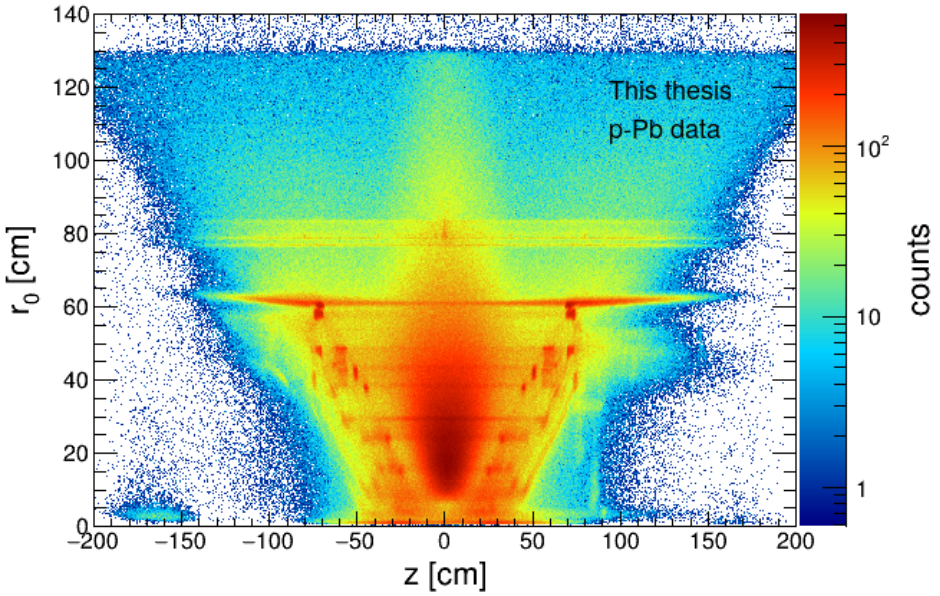

Figure 4.3: The orthogonal radius is plotted against the z value for nuclear interactions that fulfill all above mentioned cuts.

x-y plane

Regarding the x-y plane clarifies even more how well the detector structure can be resolved, especially for larger z slices. In Figure 4.4 one can see the nuclear interaction distribution in the x-y plane for various z slices, as indicated. From outside to inside, the TPC inner field cage vessel with TPC rods, the inner containment vessel and parts of the ITS are visible. For $|z| > 20\,\text{cm}$ the previously mentioned 'background' structure is not dominant anymore. Especially in a range of $20 < z < 60\,\text{cm}$, the ITS shape is well resolvable, while for larger $|z|$ the ITS detector layers cannot be seen because they are build in more narrow z ranges – see Figure 4.2. In every z slice plot, the TPC inner field cage vessel with TPC rods and the inner containment vessel are unambiguously resolved – for comparison see Figure 4.5.
In conclusion, one can say that nuclear events can be resolved adequately, which motivates the feasibility of S detection in similar interactions. However, the combinatorial background has to be taken into account and will remain an extensive challenge in the following chapters.

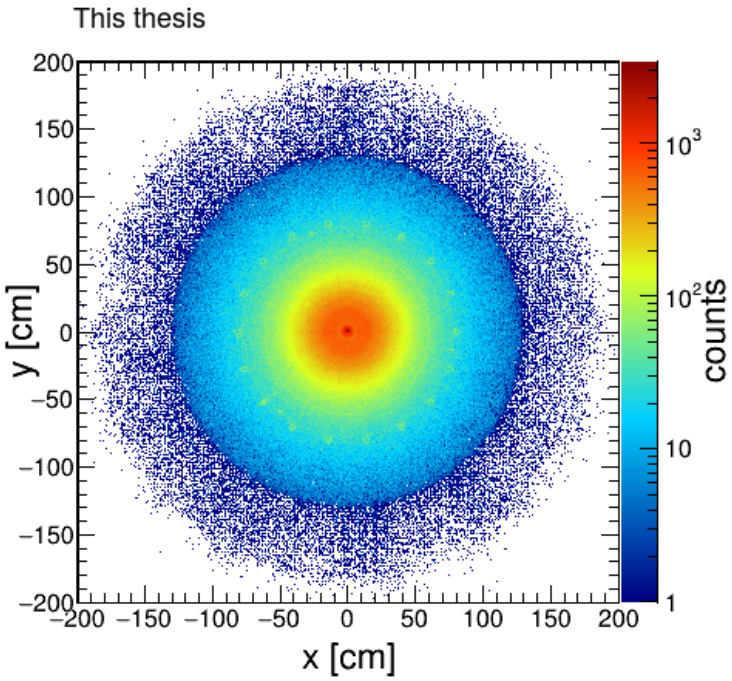

(a) $0 < z < 20\,\mathrm{cm}$

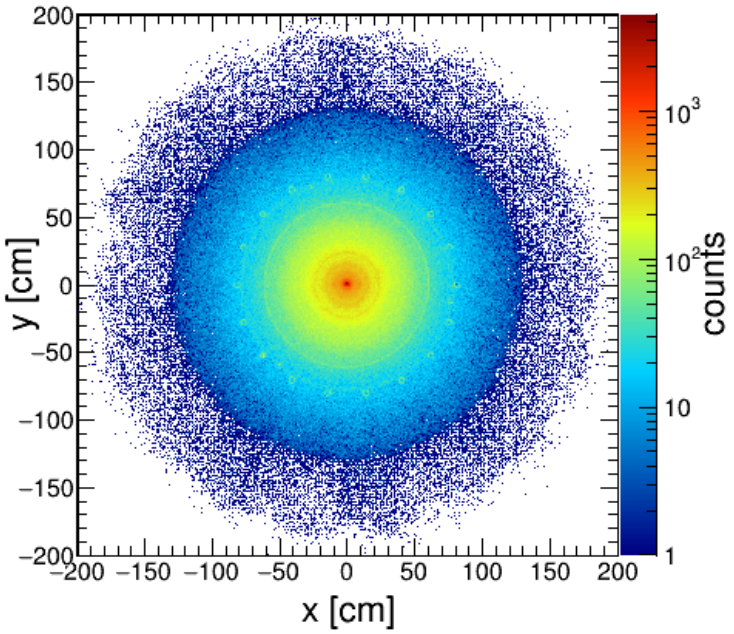

(b) $20 < z < 40\,\mathrm{cm}$

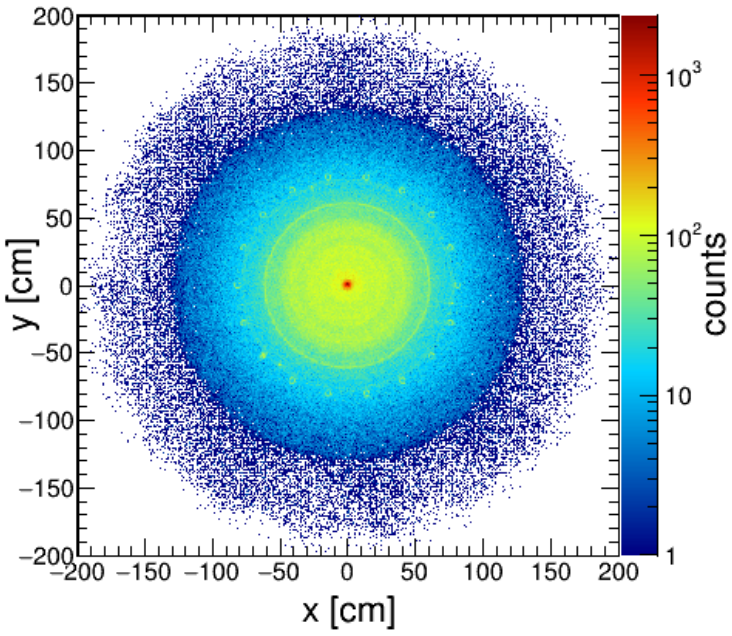

(c) $40 < z < 60\,\mathrm{cm}$

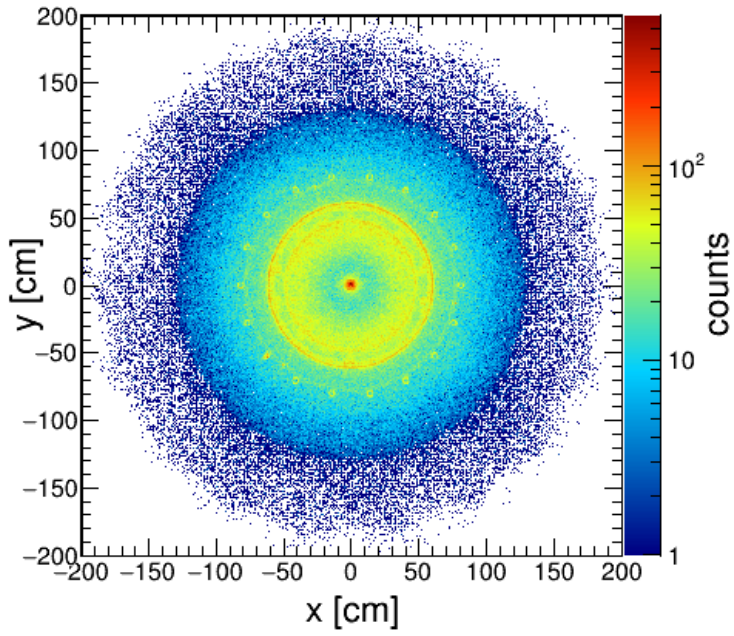

(d) $60 < z < 80\,\mathrm{cm}$

Figure 4.4: Nuclear interactions shown in x-y plane for various z slices, p-Pb data.

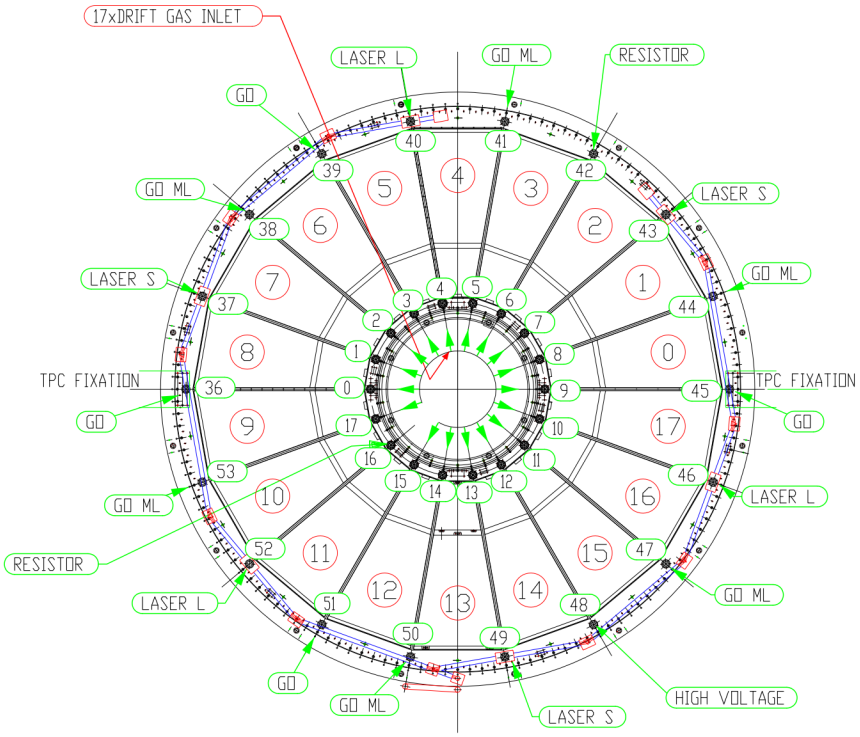

View of one of the endplates of the TPC; the different types of rods are indicated.

Figure 4.5: Illustrated TPC structure in x-y plane – taken from [49].

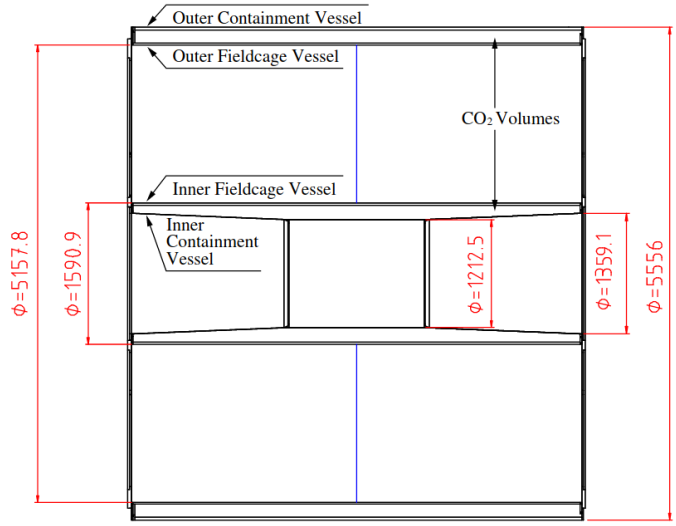

Figure 4.6: Schematic structure of the TPC in z-r_0 plane – taken from [58].

5 Estimation and simulation of S reaction channels

5.1 Motivation and overall strategy

As discussed in section 1.6, the S might exist having a mass of $m_S \gtrsim 2m_p$. It was already mentioned in section 1.6.3 that a possible discovery channel might be $\overline{S}$ that are produced in heavy ion collisions and interact with detector material, resulting in a characteristic strangeness **S**=2 state. The ALICE experiment is then capable of detecting and identifying the charged and neutral reaction products of such a nuclear interaction, as we showed in chapter 3, where the ability to reconstruct strangeness carrying particles like kaons, Λ's, cascade particles and Ω's was analyzed. Furthermore, it was shown that nuclear events can be detected precisely, so that we are able to reconstruct the shape of the ALICE detectors. In combination, this knowledge will be used to apply it on the S topology and PID. Firstly, in section 5.2 it is discussed which nuclear interaction channels are possible and the most promising candidates are chosen for the further analysis. Then in section 5.3 a phase space simulation for these channels is done which delivers as result angular and momentum distributions as well as reconstructed invariant mass spectra for the S. As a starting point before analyzing data, it is reasonable to estimate how many S are expected to be produced in Pb-Pb collisions. It was out of scope for this thesis to perform a full GEANT simulation for the S analysis, therefore the interaction with detector material and efficiency plus acceptance were estimated. Moreover, topology cuts and PID cuts have to be taken into account. As a result we obtain in section 5.4 an estimate in which order of magnitude the number of detectable S might be. A further study of the mentioned reaction channels will be done in chapter 6, considering reasonable topology cuts, particle identification and possible ways of background estimation.

5.2 Reaction channels

In Pb-Pb collisions, the S and its antiparticle $\overline{S}$ should be produced in equal amounts. Due to the lack of antinucleons in the detector material, there are in general two interaction possibilities:

R(S): S + p/n

R($\overline{S}$): $\overline{S}$ + p/n

In case of R(S) the S has a baryon number of **B**=2 and it interacts with a proton or neutron, so due to baryon number conservation, the products have to have in total a baryon number of **B**=3. Hence the sum of the masses of all final particles m_{sum} has to be at least larger than $3m_{\mathrm{p}}$ (because the proton is the lightest baryon). In fact it holds that $m_{\mathrm{sum}} \gg 3m_{\mathrm{p}}$ because the interactions are mediated via the strong force, so the quark content cannot change and therefore the products must contain two strange carrying particles which are heavier. In case R($\overline{S}$) the overall baryon number of all final particles only has to be **B**=1. Therefore the masses of the products can be lighter, so in phase space it is much more likely, which is the reason why case R(S) is expected less frequently than R($\overline{S}$). Accordingly, possible reaction channels of the $\overline{S}$ with nuclei will be studied. There are various possibilities for products because in general there is the possibility that multiple emitted gluons form quark-antiquark pairs, which combine to additional particles. In the following only those reactions which conserve exactly the reactant quark content are presented:

$\overline{S}$ + n →

$\overline{\Lambda}$ $\mathrm{K}^+\pi^-\pi^0$

$\overline{\Lambda}$ $\mathrm{K}^0\pi^-\pi^+$

$\overline{\Lambda}$ $\mathrm{K}^0\pi^0\pi^0$

$\overline{\mathrm{p}}$ K^0 $\mathrm{K}^0\pi^+$

$\overline{\mathrm{p}}$ K^0 $\mathrm{K}^+\pi^0$

$\overline{S}$ + p →:

$\overline{\Lambda}$ $\mathrm{K}^+\pi^-\pi^+$

$\overline{\Lambda}$ $\mathrm{K}^+\pi^0\pi^0$

$\overline{\Lambda}$ $\mathrm{K}^0\pi^+\pi^0$

$\overline{\mathrm{p}}$ K^+ $\mathrm{K}^+\pi^0$

$\overline{\mathrm{p}}$ K^+ $\mathrm{K}^0\pi^+$

For the following analysis we focused on the most promising reaction channels. Generally it holds that we are not able to detect π^0s efficiently and therefore all channels containing it are not ideal. As shown in section 3.4, the reconstruction purity of secondary neutral particles like K^0s and $\Lambda/\overline{\Lambda}$s is inconvenient and therefore channels that contain more than one neutral particle are not favored.
Finally we decided to focus on the following three channels:

a) $\overline{S} + \mathrm{p} \rightarrow \bar{\mathrm{p}} + \mathrm{K}^+ + \mathrm{K}^+ + \pi^0$

b) $\overline{S} + \mathrm{p} \rightarrow \bar{\mathrm{p}} + \mathrm{K}^+ + \mathrm{K}^0 + \pi^+$

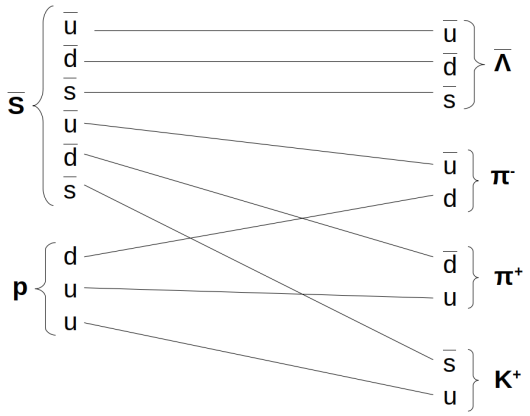

Figure 5.1: Description of channel c) on quark level.

c) $\overline{S} + \mathrm{p} \rightarrow \overline{\Lambda} + \mathrm{K}^+ + \pi^- + \pi^+$

Channel a) was chosen, because it does not contain any Lambda or kaon, however, the π^0 constitutes a disadvantage, since it is not detected and therefore a precise invariant mass reconstruction of the $\overline{S}$ will be impossible for this channel. The antiproton and K^+ in a) and b) form a characteristic V^0 that will be used for reconstruction – see section 6.2.2. In all three channels the $\overline{S}$ vertex is the origin of three charged detectable particles so it can be distinguished from a V^0 consisting of solely two daughter tracks. In Figure 5.1 a quark-line diagram for channel c) is shown which illustrates how the interaction occurs on quark level and that all quark flavors are conserved. How the interactions happen topologically will be discussed in section 6.2. In the following the distinction between S and $\overline{S}$ will be dropped and both are denoted by S, so an S candidate is in fact an interaction of the $\overline{S}$. Moreover, the K^0 is produced as strong eigenstate in a nuclear interaction but decays as weak eigenstate K_S^0 or K_L^0 – see section 3.3.1. So if we talk about the reaction channel, then the term K^0 should be used and in contrast if detected particles are considered, then mainly the K_S^0 is meant. However, often the channel and measured particle are discussed simultaneously therefore in the following the distinction will be dropped and the general term K^0 is used.

5.3 Phase space simulation

In this chapter a phase space simulation is described which was done for the three mentioned channels in order to obtain information about momentum distributions and invariant mass spectra. We used the root object 'TGenPhaseSpace' in order to simulate the 'decay' which in our case is the nuclear interaction that is regarded as fixed target experiment. The S mass is assumed to be the double proton mass $m_S = 1.876\,\mathrm{GeV}/c^2$. For the proton as target, a Fermi momentum distribution obtained from [59] is used and the momentum direction is chosen randomly. The S beam hits the target in a given direction that is obtained by using the transverse momentum distribution of deuterons

based on [60] and setting the pseudorapidity to a random value in between $|\eta| < 0.8$. In the simulation both four-momenta of beam and target are added and a decay into the daughter particles with given masses, depending on the reaction channel, is simulated. As result four-momenta of all products are created. In reality these particles have to be measured, and their four-momenta have to be reconstructed which involves the uncertainity of the TPC. This is included in the simulation by 'blurring' the momenta of charged particles by adding a Gaussian distributed uncertainity value with $\sigma_{\text{Gauss}}=\sigma_{pT}$ where σ_{pT} is the p_T resolution obtained from [61] and depends on p_T. In channel b) and c) there is a neutral particle as reaction product, namely the K^0 and $\overline{\Lambda}$. Their decay is also simulated and an uncertainty is added to the momenta of the daughter particles. Then the four-momentum of the neutral particle is reconstructed and after that the reconstruction of the S momentum and mass is done. In total, a statistic of 1 million S collision events was created.
Firstly one can look at momentum distributions of final particles like for example the K^+ in channel b) which is shown in Figure 5.2a. Mostly, the momentum is lower than $1\,\text{GeV}/c$, so that in $\text{d}E/\text{d}x$ there should not be a too big overlap with pions. This motivates that a sufficient PID can be done, and 'overlap cuts', like described in section 6.3.1, will mainly affect the background and not the reaction products of the S, if they exist.

Another quantity of main interest in this simulation is the shape of the reconstructed S mass distribution, which is shown for channel a) and b) in Figure 5.3 respectively Figure 5.4. The distribution for channel c) – which can be found in the appendix Figure 8.6 – is nearly identical to that in channel b) because it contains the same number of final particles and the equal Fermi-momentum distribution is used. In channel a) there is a missing particle which leads to a mainly lower reconstructed invariant S mass than actually correct. The width of the peak for channel b) and c) is nearly identical and almost completely determined by the Fermi-momentum distribution of the proton (in the detector material). The effect of including the measurement uncertainties of the final particle momenta is negligible – as one can see by comparing the width of the curves with and without Fermi-momentum. In conclusion, the invariant mass distribution for the reconstructed S is obtained for all three channels of interest. This gives the possibility to compare measured S mass spectra with the simulated one. However, the width of the peak is not narrow, which indicates that it will be challenging to detect a S peak over the expected large background.

In section 5.4 and 6 the expected angular distribution of the K^0 is needed in order to do an estimation and define reasonable cuts. This simulated distribution is shown in Figure 5.2b. As suggested, due to total momentum conservation, it is more likely in phase space that the K^0 moves forward compared to the direction of the S.

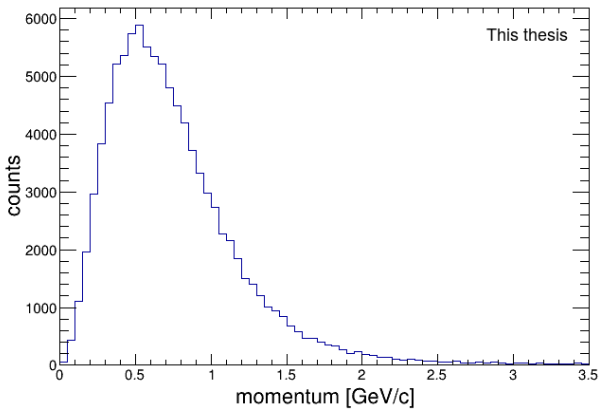

(a) Momentum distribution of positively charged kaons in channel b).

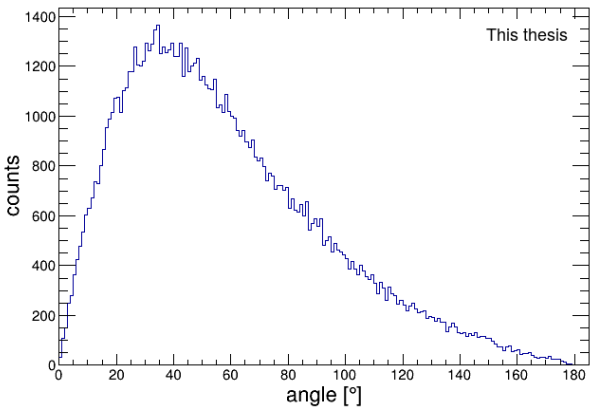

(b) Distribution of the angle between the K^0 momentum vector and the S momentum vector.

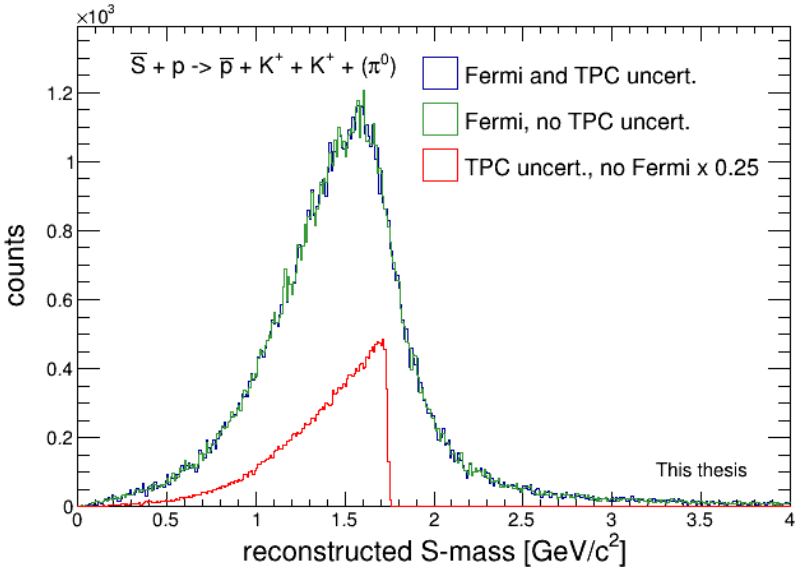

Figure 5.3: Simulation of reconstructed S mass for channel a). 'TPC uncert.' stands for adding a Gaussian distributed uncertainty value to the momentum of each final particle. 'Fermi' means including the Fermi-momentum of the proton in the detector material. The π^0 is not detected and therefore not included in the reconstruction.

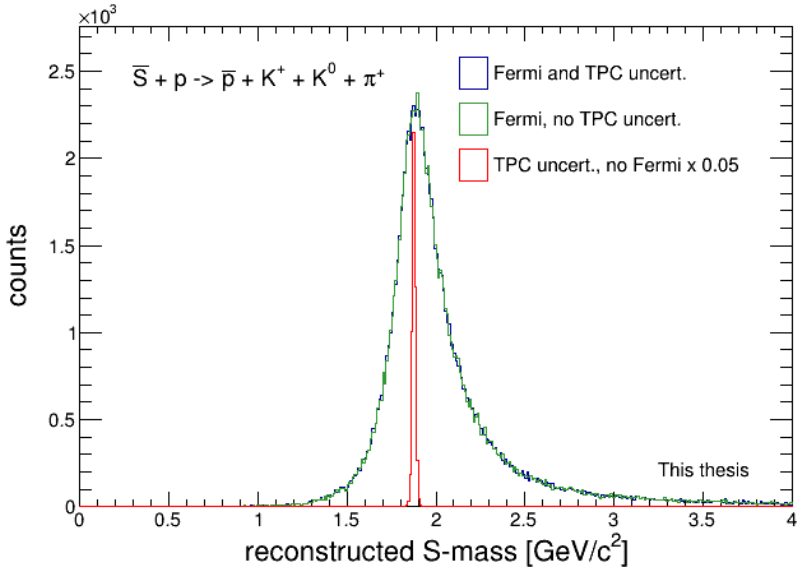

Figure 5.4: Reconstructed S mass for channel b) in simulation. Same nomenclature as in Figure 5.3.

5.4 Estimation

In this section it will be estimated how many S might possibly be detected in the further analysis, depending on the number of Pb-Pb events, the nuclear interaction probability of the S, the 'branching ratio' of the chosen channel, reconstruction efficiencies and effects respectively losses due to topology and PID cuts. Some of these cuts, especially for topology, are already used for the estimation in this chapter, and will be described later in detail in section 6.2 respectively 6.3. In order to anticipate it, this estimation will be based on some assumptions and therefore does not claim to be precise, but should rather give an order of magnitude estimation for the expected number of possibly detectable S particles. This chapter deals with channel b) ($\bar{\mathrm{S}} + \mathrm{p} \rightarrow \bar{\mathrm{p}} + \mathrm{K}^+ + \mathrm{K}^0 + \pi^+$), however an estimation for the other channels can be done analogously because in principle the same arguments hold. In the following all contributing factors will be listed, calculated and discussed:

Total number of Pb-Pb events

The number of possibly existing S scales linearly with the total number of Pb-Pb collisions. In this thesis data from 2015 and 2018 were analyzed. As result we achieved combined a total number of Pb-Pb events of $N_{\mathrm{PbPb}} = 2.169 \cdot 10^8$.

Number of produced S per event

The next step is to estimate the number of produced S per Pb-Pb event $N_{S,\mathrm{prod}}$. As a basis, data of measured $\mathrm{d}N_{\mathrm{d,prod}}/\mathrm{d}y$ of deuterons from Pb-Pb collisions at $\sqrt{s_{NN}} = 2.76\,\mathrm{TeV}$ are used [62]. Deuterons also consist of six quarks and have a similar mass, so to some extent they are comparable to S particles with regard to the production. The value $\mathrm{d}N_{S,\mathrm{prod}}/\mathrm{d}y$ for the S is obtained by calculating the number density n of deuterons (n_{d}) and S particles (n_S) in a non-interacting hadron gas, using the equation [63] [64]:

$$n = \frac{g}{2\pi^2} T \cdot \sum_{k=1}^{\infty} \frac{m^2}{k} s^{k+1} \cdot e^{k\cdot\mu/T} \cdot K_2(km/T). \tag{5.1}$$

In this equation g is the spin degeneracy $g = 2 \cdot spin + 1$, while $spin = 1$ for deuterons and $spin = 0$ for the S. The value s is the sign, which is -1 for fermions and +1 for bosons, so in our case it holds $s = +1$ because deuteron and S are bosons. For T the chemical freeze-out temperature of the quark-gluon plasma $T = 156\,\mathrm{MeV}$ is used, obtained from statistical model fits to particle yields [65], m is the mass, and the baryo-chemical potential μ is set to 0. K_2 stands for the modified Bessel function of the second kind.
Applying eq. (5.1) separately for deuterons and S particles allows us to estimate the desired yield from the deuteron measurement:

$$\mathrm{d}N_{S,\mathrm{prod}}/\mathrm{d}y = \mathrm{d}N_{\mathrm{d,prod}}/\mathrm{d}y \cdot \frac{n_S}{n_{\mathrm{d}}}. \tag{5.2}$$

The resulting yield as a function of the S mass is shown in Figure 5.5. If one assumes $m_S = 2m_{\mathrm{p}}$, a value of $\mathrm{d}N_{S,\mathrm{prod}}/\mathrm{d}y = 0.0326$ is obtained for 0-10% centrality.
Under the assumption of a constant yield, the total number of produced S can be calculated by multiplication with the y range: $N_{S,\mathrm{prod}} = \mathrm{d}N_{S,\mathrm{prod}}/\mathrm{d}y \cdot \Delta y$
Given from the detector structure we know that there is an azimuthal coverage of $-0.8 < \eta < 0.8$, accordingly $\Delta\eta = 0.8 - (-0.8) = 1.6$, so Δy can be calculated using the relation [66]:

$$y(\eta) = \frac{1}{2} \log \left(\frac{\sqrt{p_T^2 \cosh^2(\eta) + m^2} + p_T \sinh(\eta)}{\sqrt{p_T^2 \cosh^2(\eta) + m^2} - p_T \sinh(\eta)} \right), \tag{5.3}$$

inserting $m = m_S = 2m_p$ and a typical value of $1.5\,\mathrm{GeV}/c$ for p_T. This results in $\Delta y = 1.06$ and accordingly $N_{S,\mathrm{prod}} = 0.0326 \cdot 1.06 = 0.0346$.

Nuclear interaction probability

As already mentioned in section 1.6.2 and section 1.6.4, the S nucleon cross section and therefore its nuclear interaction probability $p_{S,\mathrm{N}}$ is expected to be low, so accordingly this factor will significantly reduce the number of detectable S, although possibly a lot of them might have been produced as described previously.

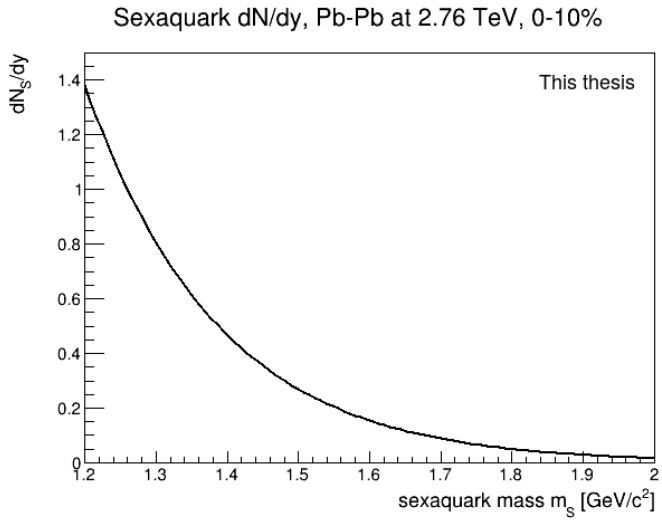

Figure 5.5: Estimated yield for the S as a function of sexaquark mass [67] for Pb-Pb collisions at 2.76 TeV and 0-10% centrality, based on the corresponding yield of deuterons from [62]. The yield is calculated using Equation (5.2), inserting number densities of deuterons and S particles obtained from Equation (5.1) using $T = 156\,\mathrm{MeV}$.

As first step, the S nucleon interaction cross section has to be estimated which is done based on [24] and [27]. Farrar discusses in [24] that $\sigma_{SN} \lessapprox (\frac{1}{4} - 1)\sigma_{NN}^{el} \approx 5 - 20\,\mathrm{mb}$, due to geometric reasons that apply for $p \gtrsim 1\,\mathrm{GeV}/c$. In [27] she demonstrates that the cross section strongly depends on the Yukawa interaction coupling strength α_{SN}. Accordingly, the true σ_{SN} might vary in a range of orders of magnitude. Assuming a repulsive interaction and demanding that the interaction cross section is compatible with experimental restrictions for dark matter, this leads to the estimation of $\sigma_{SN} < 10^{-29}\mathrm{cm}^2$. In summary, the interaction cross section remains a major uncertainty and in the following a value of $\sigma_{SN} = 10\,\mathrm{mb}$ will be used, based on the first mentioned estimation of Farrar and compatible with the previously mentioned dark matter limit.
In order to get an interaction probability, the effective thickness of the detector material has to be calculated, depending on various quantities like the (target/detector) element, its radiation length X_0 [in g/cm^2], molar mass M [g/mol][1], proton number Z [unitless], Avogadro number $N_A[\mathrm{mol}^{-1}]$ and fraction of radiation length f. As a result the effective target thickness given as the number of protons per mb (t_p) is obtained according to the following equation[2]

$$t_p = f \cdot X_0 \cdot N_A/M \cdot Z \cdot 10^{-27}. \tag{5.4}$$

If t_p is known, the desired interaction probability of S and proton $p_{S,p}$ can simply be calculated by: $p_{S,p} = t_p[\mathrm{mb}^{-1}] \cdot \sigma_{SN}[\mathrm{mb}]$. The fraction of radiation length $f \approx 0.125$,

[1] The molar mass M and mass number A only differ in unit.
[2] N_A/M gives the number of atoms per g and multiplying by Z gives the number of protons per g.

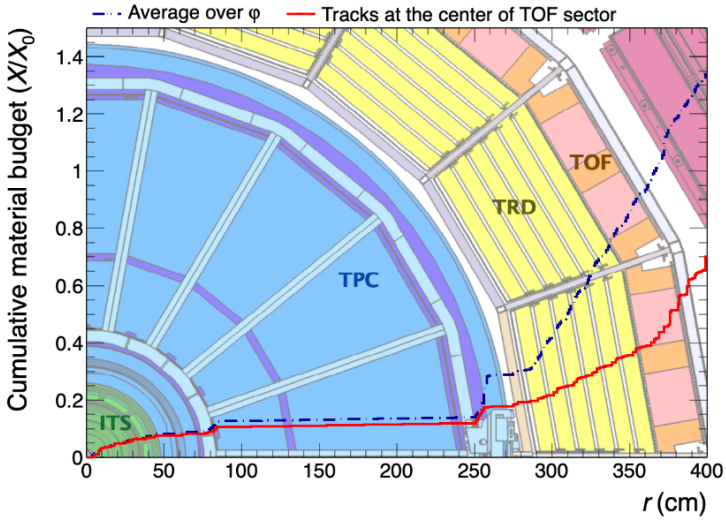

Figure 5.6: Material budget in units of relative radiation length – taken from [69].

used in Equation (5.4), is obtained from Figure 5.6, because our measurement range goes roughly up to the plateau at $r = 150\,\mathrm{cm}$. As average values of molar mass and proton number in Equation (5.4) we used $M = 31.8\,\mathrm{g/mol}$ and $Z = 14.8$ based on [68][3]. These values refer to the ALICE detector material from the primary interaction point up to the TOF, weightening the contribution from different materials with their density and length crossed by particles. The radiation length X_0 is estimated based on the elements aluminum and silicon which can mainly be found in the detectors. Unfortunately no exact detector composition ratio was found in [68] or any other source, therefore we assumed $X_0 = 20\,\mathrm{g/cm^2}$, which is chosen a bit lower than $X_{0,\mathrm{Al}} = 24.01\,\mathrm{g/cm^2}$ and $X_{0,\mathrm{Si}} = 21.82\,\mathrm{g/cm^2}$ because of some copper parts in the detector. X_0 only contributes linearly in Equation (5.4), therefore the uncertainty due to estimating it imprecisely is negligible compared to other estimations in this chapter.
Finally a value of $p_{S,p} = 0.0070$ is obtained.

Branching ratio

As discussed in section 5.2, there are various possible final states for an S nucleon interaction. We listed in total five reaction channels for an S interacting with a proton, considering only channels that conserve the quark content. Generally, other final states are also possible, but are likely suppressed because of the OZI rule [70] or in general because of participating gluons. The sum of the final state masses of all mentioned reaction channels does not differ significantly and ranges from 1.879 to $2.069\,\mathrm{GeV}/c^2$, accordingly we do not expect any of them to be massively suppressed or favored in phase space. In order to get an exact result of the branching ratio, a simulation including

[3] In [68] the value for A is given.

momenta distributions and all conceivable reaction channels would be necessary, however, at this point we are satisfied with a qualitative estimation, so we assume each channel to be equally likely. Therefore according to this assumption, the branching ratio for channel b) would be 1/5. Because we cannot exactly determine the fraction of other not considered interaction channels, we include an uncertainty factor of 2 at this point, so that the branching ratio of channel b) $BR(S + \mathrm{p} \rightarrow \text{channel b})$ is estimated to be 1/10.

Another branching ratio which has to be considered is, that we only reconstruct K^0s that decay into charged pions, which happens with a probability of 69.2% [71]. Moreover we expect that half of the K^0 mesons decay as K^0_L which are usually not detected.

Reconstruction efficiencies

In order to reconstruct an S interaction, all corresponding tracks and V^0s have to be found. The track reconstruction efficiency for secondary tracks is roughly $e_{track} = 0.9$ [72]. Accordingly for channel b) which results in 5 final tracks, a factor of e^5_{track} contributes.

In general it is hard to find an exact value for the reconstruction efficiency of V^0 without a full GEANT simulation, given that both track daughter tracks are already reconstructed. Limiting factors for this efficiency might be imprecisely reconstructed tracks that do not have a sufficiently low dca to each other, so that although they originate from one vertex, the V^0 is not reconstructed. Furthermore, as described in section 2.8.4, the impact parameter cuts might exclude some true V^0s, because one daughter track might coincidentally come close to the primary vertex, which is more likely for decaying high momenta neutral particles, whose daughters have a small opening angle. Anyway, we expect the V^0 reconstruction efficiency to be quite high of the order 0.95. Therefore in channel b) which consists of two V^0s, a factor of 0.95^2 has to be taken into account.

PID efficiency

For all charged particles, a $\mathrm{d}E/\mathrm{d}x$ cut of $n\sigma < 2$ is used – for explanation see section 3.1. If we assume the distribution of $\mathrm{d}E/\mathrm{d}x$ around the expected value from Bethe-Bloch to be Gaussian with a standard deviation that is determined by the detector resolution, then a 2σ range should include 95% of the corresponding particle species. Therefore in channel b) a factor of 0.95^5 limits the PID efficiency due to $n\sigma$-cuts.

The TOF efficiency for primary particles can be found for example in [73]. However, in our special case, which deals solely with secondary tracks, we cannot assume such a high efficiency. Furthermore, as discussed in section 3.2, there are other uncertainties that play a role for secondary tracks. Therefore, the TOF efficiency is determined as the ratio of the number of particles for which the TOF information is available divided by the number of tracks. This was done for the $\mathrm{d}E/\mathrm{d}x$ identified K^+ in channel b), using 182198 tracks in total, while 42704 corresponding TOF hits were registered, resulting in an efficiency of 23.4% We do not demand for every track a TOF hit, so it would be an overestimation to use 0.234^5 as factor. Instead, for each particle that is not a pion, we

check if there is an overlap in $\mathrm{d}E/\mathrm{d}x$ with any other particle. Only if so, then an m^2 information is demanded – see section 6.3.1. We measured how often an overlap occurs for antiproton and kaon which is in 58% the case for antiprotons, and in 93% it happens for kaons. As already seen in section 3.2, the overlap of kaons with other particle species is very frequent. Considering all possible cases in a tree structure, like e.g. the antiproton does not have an overlap, but the kaon does, so that in a fraction of $(1 - 0.58) \cdot 0.93$ of all cases one TOF hit is demanded, resulting in a factor of $0.42 \cdot 0.93 \cdot 0.234$ for this branch, and adding all of them up, leads to a TOF efficiency factor of 0.1598.

Effects of topology cuts

The topology cuts will be discussed in detail in section 6.2 where also the used abbreviations are explained. Usually an efficiency and purity optimization would be desirable, however, due to the complex topology we have to deal with a 'best guess approach'. In this part we will roughly try to estimate the influence of the used topology cuts, assuming one cut combination, although in the following chapters the cuts will be slightly varied. If we demand that the distance between K^0 vertex and S is in the range of $0.5 < \mathrm{dist}(\mathrm{K}^0, S) < 20\,\mathrm{cm}$, as used in chapter 6, the number of K^0_S mesons decaying in this interval can be estimated using the decay length L in the exponential decay. Assuming an average K^0 momentum of $0.5\,\mathrm{GeV}/c$ – see section 5.3, this leads to:

$$L = \tau c \beta \gamma \tag{5.5}$$

$$L = 8.95 \cdot 10^{-11}\mathrm{s} \cdot 3 \cdot 10^8 \frac{\mathrm{m}}{\mathrm{s}} \cdot 0.71 \cdot 1.42 \tag{5.6}$$

$$L = 2.71\,\mathrm{cm} \tag{5.7}$$

and accordingly the relative number of K^0_S mesons in that interval is: $N = e^{-0.5/2.71} - e^{-20/2.71} = 0.831$.

In the following, we will mainly be interested in S candidates with sufficient radial distance from the primary vertex, in order not to be dominated by combinatorial background. Therefore the restriction of around $r > 40\,\mathrm{cm}$ is used. The number of produced S that would interact in that region can be estimated based on the material budget – see Figure 5.6. Comparing the value at the end of our measurement range (12.5%) to the value at $r = 40$ (7.5%), a fraction of $5/12.5 = 0.4$ is left for $r > 40\,\mathrm{cm}$ in our detection range.

If we cut on the angle between K^0 and the connection vector β from primary to S vertex, so that $\beta < 120°$, this should only reduce the number of detectable S by a factor of about 0.94, which is obtained from the simulation in section 5.3 using the expected angular distribution of the K^0 in Figure 5.2b.

Furthermore we apply cuts in order to assure that the particles are nonprimary. In this estimation a K^0 at $r = 40 + 3$ cm will be considered for which $\mathrm{dca}(\mathrm{K}^0, \mathrm{prim}) \gtrsim 3\,\mathrm{cm}$ is demanded according to the linear dependent $\mathrm{dca}_{\mathrm{PV}}$ used in section 3.4. Based on its

angular distribution compared to the flight direction of the S – see Figure 5.2b – will be calculated which fraction coincidentally points back towards the primary vertex within a 3 cm window. It is assumed that the S roughly originates from the primary vertex, so that the angular estimation can be done. For simple geometrical reasons it follows that the angle between K^0 and S flight direction α must fulfill $|\alpha| < \tan^{-1}(3./43) \approx 4°$ if dca(K^0,prim) < 3 cm. Based on the simulation this happens in 0.54% of all events, so a factor of 0.9946 contributes. In a similar way the in section 6.2.3 mentioned cut dca(K^0-$\pi^{\pm}, S$) > 0.2 cm can be estimated, assuming a distance of 3 cm between S vertex and K^0 vertex. This does not happen in 95.2% of all cases. Further cuts like e.g. dca($K^0 - \pi^{\pm}$, prim) > 2 cm and dca(π^+, prim) > 2 cm are expected to maintain a fraction larger than 99% due to the large distance of at least 40 cm (similar to the restriction dca(K^0,prim) > 3 cm) and therefore they are neglected.

Final calculation

Combining all the contributing factors discussed previously, an order of magnitude estimation of possibly detectable S candidates in channel b) is achieved. However it has to be considered, that many assumptions were made, especially for the numbers of S per event, the nuclear interaction probability and for the branching ratio. The effects of the topology cuts are mainly based on a simple phase space simulation, more precise results could be achieved by a full simulation which exceeds the scope of this thesis.
Overall we perhaps expect that there could be in total a number of detectable S candidates N:

$$\begin{aligned} N_{S,\mathrm{meas}} &= N_{\mathrm{Pb,Pb}} \cdot N_{S,\mathrm{prod}} \cdot p_{S,\mathrm{p}} \cdot BR(S + \mathrm{p} \rightarrow \text{channel b}) \cdot BR(\mathrm{K}^0_S \rightarrow \pi^+ + \pi^-) \\ &\quad \cdot BR(\mathrm{K}^0 \rightarrow \mathrm{K}^0_S) \cdot e^5_{\mathrm{track}} \cdot e^2_{\mathrm{V}^0} \cdot e_{n\sigma} \cdot e_{\mathrm{TOF}} \cdot N_{\mathrm{dist}} \cdot N_{r,40} \cdot N_{\mathrm{ang}} \cdot N_{\mathrm{dca,K0}} \cdot N_{\mathrm{dca},\pi} \\ N_{S,\mathrm{meas}} &\approx 35 \end{aligned}$$

Contributing factors in final calculation		
variable	**explanation**	**value**
$N_{\mathrm{Pb,Pb}}$	number of Pb-Pb events	$2.169 \cdot 10^8$
$N_{S,\mathrm{prod}}$	number of produced S per event	0.0345
$p_{S,\mathrm{p}}$	probability that S interacts with proton	0.007
$BR(S + \mathrm{p} \rightarrow$ channel b)	branching ratio that S which interacted with proton results in channel b)	0.1
$BR(\mathrm{K}^0_S \rightarrow \pi^+ + \pi^-)$	branching ratio that K^0_S decays into two charged pions	0.692
$BR(\mathrm{K}^0 \rightarrow \mathrm{K}^0_S)$	branching ratio that strongly produced K^0 decays as K^0_S	0.5
e^5_{track}	efficiency for reconstruction of 5 tracks	0.9^5
$e^2_{\mathrm{V}^0}$	efficiency for reconstruction of 2 V^0s	0.95^2
$e_{n\sigma}$	efficiency of $n\sigma$ cut	0.7738
e_{TOF}	efficiency of 'overlap' m^2 cut	0.1598
N_{dist}	fraction of remaining S after cut $0.5 < \mathrm{dist}(\mathrm{K}^0, S) < 20\,\mathrm{cm}$	0.831
$N_{r,40}$	effect of cut $r > 40\,\mathrm{cm}$	0.4
N_{ang}	effect of angular cut $\beta < 120°$	0.94
$N_{\mathrm{dca,K0}}$	effect of dca(K^0,prim) $< 3\,\mathrm{cm}$	0.9946
$N_{\mathrm{dca},\pi}$	effect of demanding dca(K^0-$\pi^\pm, S$) $> 0.2\,\mathrm{cm}$ for K^0 daughters	0.952

Table 5.1: Overview and explanation of all contributing factors in the final calculation.

6 Data analysis

In this chapter the previously gained knowledge from PID (chapter 3), secondary hadronic interactions (chapter 4), the study of possible reaction channels and the phase space simulation (chapter 5) will be used in order to define reasonable cuts for possible S candidates that might be found by analyzing Pb-Pb data. The aim of this thesis is to prove conceptually that the S search can be done in the described way. A full analysis, including complete GEANT based simulations and the study of all efficiencies, uncertainties and background sources, would exceed the scope of this thesis, accordingly this thesis should rather be seen as feasibility study that motivates further analysis of ALICE data with regard to the S.

6.1 Overview of analysis structure

The analysis is structured in two parts. Firstly there is an analysis task, looping over Event Summary Data (ESD) files of $\sqrt{s_{NN}} = 5.02\,\text{TeV}$ Pb-Pb data from 2015 and 2018 separately. This task takes all relevant information of tracks and V^0s from the ESD files and stores them in our own data container classes. There are classes for tracks, V^0s, nuclear events, and S candidates. Cuts applied on this level of the analysis are most important because they could not be changed easily due to the fact that the task had to run on the CERN grid which takes several weeks. The reason for the duration is that one has to loop over a number of collision events of the order 10^8 which corresponds to hundreds of Terabyte data in ESD files. Moreover, the combinatorics is excessive because – as described later in detail – one has to loop over various V^0 and track combinations in each event and for each potential S candidate. Our first approach was to store all tracks and V^0s in an output 'TTree' consisting of our data container classes, but on the one hand the size of the output would exceed technical limits and on the other hand the amount of needed calculation due to combinatorics would not be feasible on local computers. Therefore we agreed on applying basic cuts that will be described in section 6.2.1 and implemented the search for reaction channels on this first level of analysis. Hence individual topological and PID cuts for each reaction channel are applied in the analysis task code – they are described in detail in section 6.2.2 respectively 6.3. Then the remaining S candidates are stored in a data container class that includes sub classes containing all tracks and V^0s with relevant information like the track helix parameters, positions of V^0s, momenta, as well as TPC and TOF particle identification information. These data can be used in order to apply stricter cuts in the next part of the analysis. The next level of analysis is a code that reads the output tree of the previous analysis task containing the S candidate data container class. Now the PID and topology can be refined and for example effects of topology cuts on invariant mass

spectra can be studied. Moreover, various methods for background estimation can be done like described in section 6.4 respectively section 6.7. In order to study whether the applied topology cuts work as expected, the remaining S candidates can be stored and plotted in 3D using the ROOT package 'TEve' [74] – see section 6.2.3. In this way also unrealistic topologies can be spotted and accordingly cuts can be improved or added.

6.2 Topology cuts

If the S exists its reactions could be filtered by demanding distinct topological structures as described in the following. As mentioned in section 6.1, the analysis is divided in various steps and correspondingly the topological cuts are applied successively. Firstly some general cuts are applied mainly in order to reduce the combinatorics. Then each channel is further analyzed by individually applying reasonable topological cuts like in particular restrictions for distances of closest approach (dca). This is done by rather loose cuts in the analysis which runs on the GRID and they will be refined in the further analysis.

Abbreviations

In the following some abbreviations are used, which should be explained shortly. The term 'dca' stands for distance of closest approach. An abbreviation like dca(x,y) means the smallest distance between x and y, while x/y can stand for tracks and/or vertex positions. The distance between two (vertex-)positions is abbreviated as dist(position1, position2). For the often used distance between primary and S vertex, dist(prim, S vertex), the abbreviation 'radius' or 'r' is utilized. The primary vertex position is shortly written as 'prim'. A 'secondary' track is a track which does not originate from the primary vertex in contrast to 'primary' tracks. For neutral particles, the momentum is obtained by adding the four-momenta of the daughter particles. Then the trajectory of the neutral particle is reconstructed using a straight line going through the neutral particles decay vertex and in the direction of the momentum. A term like for example dca(prim,K^0) means the smallest distance between this straight line and the primary vertex.

6.2.1 General cuts

The first characteristic of all conceivable S reactions is that only secondary tracks are detected as final particles, because the neutral primary S cannot be detected. Therefore only 'secondary' tracks with the condition that dca(prim,track) $> 0.5\,\text{cm}$ are regarded in the further analysis[1]. Moreover we excluded all V^0s that are very close to the primary vertex, with $r < 5\,\text{cm}$ due to several reasons: Inside the beam pipe there is no material, so a nuclear interaction is not possible. Moreover in an area close to the primary vertex there is the highest track density, accordingly the combinatorial background is enormous

[1] This condition is firstly only applied for tracks that do not correspond to a V^0, because for them we assume that sufficient restrictions were already set as described in section 2.8.4

which would lead to lots of fake S candidates. In general, the S could interact anywhere in the detector material, so it is reasonable to focus on outer radii where the background of for example primary Λ's and K^0s is significantly less. An observation was that some tracks look very similar if we regard them in a 3D event display although it is checked that they have different track ids. Possibly some track hypothesis, as described in section 2.8, caused a double reconstruction of the same track. Just to assure that tracks are not reconstructed twice, it is looped over all pair combinations of tracks and their direction is compared. If the direction in x, y, and z-coordinate is identical within a 5% window and moreover the dca between the tracks at one chosen point is less then 0.5 cm, then one of these tracks is excluded. To sum it up, the following cuts are applied for all tracks and V^0s independent from the S reaction channel:

- dca(track,prim) > 0.5 cm for each track
- radius > 5 cm for each V^0
- if two tracks are too similar, one is removed to assure that there is no double reconstruction.

6.2.2 Cuts and finding procedure for individual reaction channels

Various PID and topology cuts are applied for each reaction channel, which are described in the following. Figure 6.1 shows exemplarily a reaction of channel c) which displays the cut variables. Additionally in Figure 6.2 there is a zoomed in picture of a V^0 that shows which dcas play a role on this small scale. Obviously a V^0 is only theoretically a crossing point of two tracks, in reality the track helices do not intersect due to resolution effects and therefore the vertex has to be found minimizing the dcas between track and V^0 as mentioned in section 2.8.4. Although there were already cuts applied in the V^0 finding procedure, we do not want to rely on them completely, confirmed by observations in 3D which revealed that sometimes there are large dcas (of more than 5 cm) between daughter tracks. Therefore we demand in the second analysis step that dca(a or b,V^0) < 0.5 cm for all V^0s.

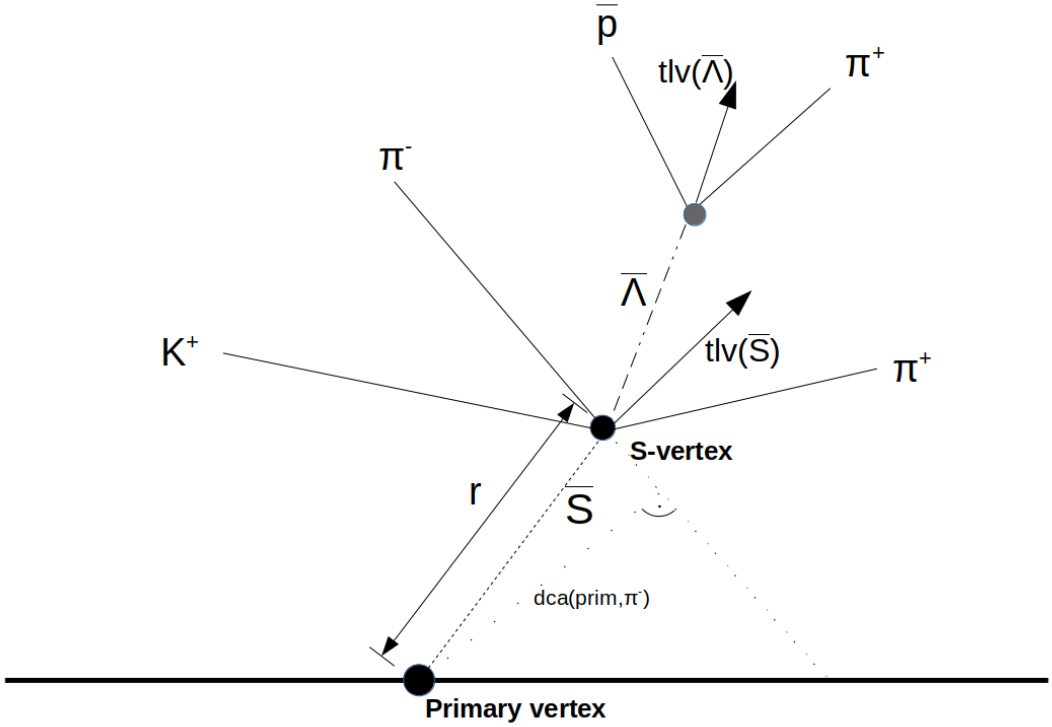

Figure 6.1: Schematic illustration of channel c). Charged particles are drawn as solid lines, neutral particles with dashed lines and dots symbolize vertices. Arrows represent the momentum components of four-momenta (tlv stands for the used ROOT class TLorentzVector), r is the distance from primary to S vertex and with doted lines the dca of the negative pion to the primary vertex dca(prim,π^-) is indicated. For simplicity the curvature of the tracks is not taken into account.

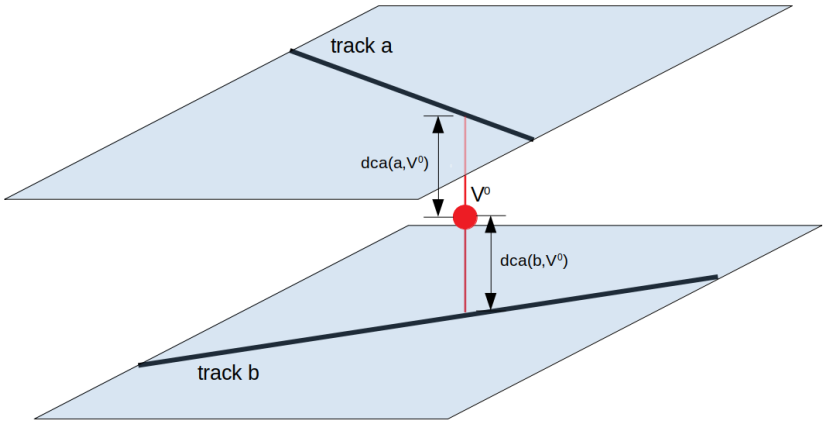

Figure 6.2: Closely zoomed in illustration of a V^0 consisting of daughter tracks a and b. As indicated by the blue layers, the drawing is in 3D. The dca(a,V^0) and dca(b,V^0) are shown. The total dca(V^0) is the sum of both.

Channel a) $\overline{S} + p \rightarrow \bar{p} + K^+ + K^+ + \pi^0$

In channel a) is one neutral particle, the π^0, which is not detected. Therefore, the search for this reaction focuses on finding a vertex which is origin of an antiproton and two K^+. We used the V^0-finder described in section 2.8.4 to get a V^0 made of antiproton and K^+. This vertex is (theoretically) the interaction point of the S with a proton and will be called 'S vertex' in the following. Then it is looped over all other secondary tracks in order to find exactly one K^+ track that also originates from the S vertex. For this secondary track we additionally demand a dca(K^+, prim) $> 2\,\mathrm{cm}$. In order to prevent unrealistic topologies like for example backwards (in direction of the primary vertex) flying daughter tracks, a comparison between total momentum vector and flying direction of the potential S is done. Therefore the connection vector between primary and S vertex is calculated and the total momentum vector of all (detected) daughter tracks at the S vertex position is obtained by adding them up. For V^0-tracks the four-vector information, given from the ESD files, was used. Oppositely, obtaining the momentum vector of a non V^0-track like the additional K^+ at a given position, cannot be done by simply using the given four-momentum in the ESD file because it does not contain the direction at this position. Hence the direction has to be obtained by 'deriving' the track path at the S vertex position. This is done by evaluating the track position twice: at the S vertex and a small step in path length further, so that the difference gives us the direction. Normalizing this direction vector and multiplying it with the absolute momentum, given at the beginning of the track, results in the momentum vector at the S vertex position, neglecting the energy loss of the particle. Normalizing the total momentum vector and the connection vector and scalar multiplying them gives us the possibility to cut on this scalar product. Because the π^0 is not detected and it could

carry a large fraction of total momentum, only a loose 'scalar product cut' is applied, demanding it to be larger than 0.6. Of course, the PID is likewise important for all channels and will be discussed in detail in section 6.3.

Channel b) $\overline{S} + p \rightarrow \bar{p} + K^+ + K^0 + \pi^+$

Compared to channel a), the topological reconstruction of b) is a bit more complicated due to the neutral K^0. Firstly (similar to a) a V^0 made of an antiproton and K^+ is found with an additional pion coming from this S vertex, which has a distance of closest approach of dca(π^+,S) $< 0.5\,$cm. In parallel the K^0 vertex is reconstructed like described in section 3.3.1. The momentum vector of the K^0 is used for backtracking the K^0 path from its vertex towards the S vertex and for calculating the dca(K^0,S). It is looped over all pairs of K^0 and S vertices, saving all of them with dca(K^0, S) $< 0.5\,$cm. We are only interested in K^0s that are created at the S vertex and therefore all primary ones have to be removed, which is done by at least demanding dca(K^0,prim vertex) $> 0.5\,$cm. For all remaining S,K^0 vertex pairs the total momentum vector is calculated and – as described in the previous part for channel a) – a scalar product cut is applied, demanding it to be larger than 0.8. At this point a stricter cut can be used because each final particle is detected. However, demanding the momentum vector to be nearly completely parallel to the vector from primary to S vertex (e.g. scalarproduct >0.95) is not recommendable due to two reasons: Firstly there is an uncertainty in the measurement of each final particle momentum which add up. Secondly in particular the Fermi-momentum of the proton can contribute to a large fraction, as discussed in section 5.3. Another reasonable cut is to demand that there is a minimum distance between S vertex and K^0 vertex, allowing a clear distinction between these two vertices. The mean path length for a mid-range momentum K^0_S is $L \approx 3\,$cm, therefore a cut of at least dist(S vertex,K^0 vertex) $> 0.5\,$cm seems to be appropriate. Of course some very low momenta kaons will be lost using this cut, anyway it is necessary in order to separate the two vertices. This distance cut is not yet implemented in the first part of the analysis which was running on the GRID but will be used later.

Channel c) $\overline{S} + p \rightarrow \overline{\Lambda} + K^+ + \pi^- + \pi^+$

The topology of channel c) is in general similar to that of channel b). The V^0 is made of K^+ and π^-, as an additional track a π^+ is found. The $\overline{\Lambda}$ as corresponding neutral particle is reconstructed similar to the K^0 in channel b). Analogous dca cuts are applied:

- dca(π^+, S) $< 0.5\,$cm
- dca($\overline{\Lambda}$,S) $< 0.5\,$cm
- dca($\overline{\Lambda}$, prim vertex) $> 0.5\,$cm
- scalarprodcut: total momentum $\cdot$ vector(prim to S) > 0.8.

The average decay length L for a mid range momentum $\overline{\Lambda}$ is approximately $L \approx 8\,$cm and therefore a distance(S,$\overline{\Lambda}$) cut will be applied hereafter.

Additional topological cut possibilities

The topology of an S interaction is definitely more complicated than reconstructing other baryons like even cascades or omegas. For each reaction channel, there are various dca and angular cut possibilities, and in the previous part of this chapter only the basic, loose cuts were described. In the following parts of this analysis more strict cuts can be applied. In general, one can cut on the following quantities: distance(prim vertex,S vertex), dca(π or K or p , S vertex), dca($\overline{\Lambda}$ or K^0 , S vertex), dca(charged particle , prim vertex), distance(S vertex, $\overline{\Lambda}$ or K^0 vertex), dca($\overline{\Lambda}$ or K^0, prim vertex) and dca($K^0/\overline{\Lambda}$-daughters , S). Furthermore there are various angles that can be used for topological cuts: One can calculate the vector from the S vertex to the $\overline{\Lambda}$ or K^0 vertex and compare it with the vector from the primary to the S vertex. Cutting on this angle can be used in order to prevent the neutral particle from flying backwards compared to the momentum direction of the S. Moreover the total reconstructed momentum of the S can be compared to the vector from primary to S vertex – as done previously by the 'scalar product' cut. Additionally, for V^0s that were found by the V^0 finder, one can cut on the distance of the daughter tracks a and b to the V^0: dca(a or b , V^0). There are even more topological quantities like the opening angle of V^0s or the pseudorapidity of the S that could be used for cuts.
Obviously due to the complex topology of S channels it is not possible to apply strategies like a 'brute force' variation of the cuts in order to find the best cut combination. Instead different reasonable cut combinations were used.

6.2.3 Example topology

In Figure 6.3 an example S candidate of channel b) is shown. The following cuts are applied in addition to the previously described basic cuts:
distance cuts: $1.5\,\text{cm} < \text{dist}(K^0,S) < 25\,\text{cm}$, radius $> 40\,\text{cm}$
dca cuts: $\text{dca}(K,S) < 0.5\,\text{cm}$, $\text{dca}(p,S) < 0.5\,\text{cm}$, $\text{dca}(\pi^+,S) < 0.5\,\text{cm}$, $\text{dca}(K^0\text{-}\pi^+,S) > 0.2\,\text{cm}$, $\text{dca}(K^0\text{-}\pi^-,S) > 0.2\,\text{cm}$, $\text{dca}(\text{particle,prim}) > 0.5\,\text{cm}$ for all 5 final particles, $\text{dca}(K^0,\text{prim}) > 2\,\text{cm}$
angular cuts: angle between vector from primary to S vertex and vector from S vertex to K^0 vertex $< 120°$
PID-cuts: if overlap in $\mathrm{d}E/\mathrm{d}x$ for proton and other particles then: $0.6 < m^2 < 1.2$ $(\text{GeV}/c^2)^2$
if overlap in $\mathrm{d}E/\mathrm{d}x$ for K^+ and other particles then: $0.2 < m^2 < 0.35$ $(\text{GeV}/c^2)^2$
The term 'K^0-π^+' means the positive pion that is a daughter particle of the K^0, not to confused with the π^+ that originates from the S vertex. All PID-cuts do not play a role for the topology and are only listed for completion. They are discussed in chapter 3. The meaning of the colored lines, dots and arrows is explained in the caption of Figure 6.3. This example fulfills all topological criteria we demand: Firstly all tracks are clearly distinguishable, there is no overlay that might indicate doubly reconstructed tracks and both V^0s seem to be the origin of the corresponding tracks. The K^0s momentum is compatible to the assumption that it originates from the S vertex which can be

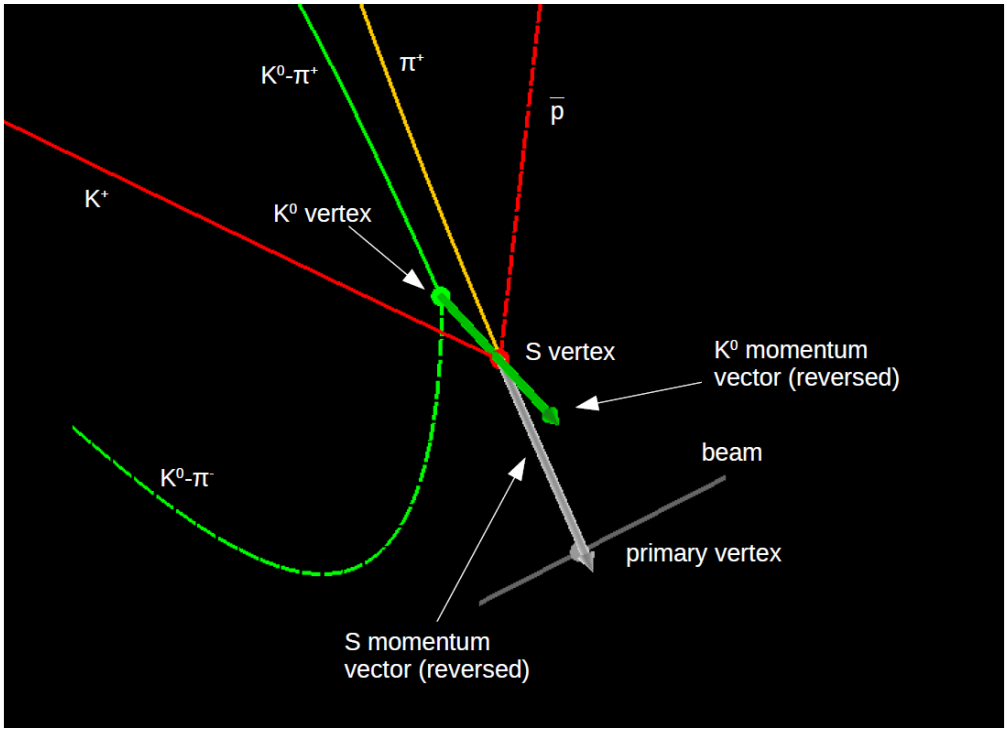

Figure 6.3: An example S candidate of channel b). The applied topology cuts are described in the chapter. The beam is drawn as grey line with the primary vertex as grey dot. In red there is the S vertex with its daughter particles the K^+ (solid red line) and $\bar{p}$ (dashed red line). From the S vertex also originates the π^+ drawn as orange line. Green colored is the K^0 vertex with its daughter particles $K^0 - \pi^+$ (solid) and $K^0 - \pi^-$ (dashed). The inverse momentum vector of the K^0 is drawn as green arrow that goes through the S vertex, as supposed to. The total inverse momentum vector of the S is drawn as grey arrow.

seen by the green arrow, that goes through the S vertex. Moreover the back-pointing K^0 momentum does not point towards the primary vertex, which assures that it is a secondary particle. The total momentum vector of the S (reversed) goes in the direction of the primary vertex which substantiates the assumption that the red dot might be a real nuclear interaction point of a primary S.

6.3 PID

One of the most important parts of this thesis is to optimize particle identification. Finding candidates that fulfill basic topology cuts and whose final particles can be clearly identified as reaction products of a S channel, would be a strong hint for the existence of the S. Even finding a vertex that is origin of two strange carrying particles (net

strangeness of +2 or -2) would be a serious candidate. However, as already indicated in chapter 3, there are various challenges in particular regarding the purity of PID. For charged particles there is an overlap in $\mathrm{d}E/\mathrm{d}x$ depending on the momentum and in particular kaons can hardly be distinguished from pions. Moreover, as shown in section 3.4, K^0's and Λ's especially secondary ones at larger radii – that are most interesting for S candidates – only deliver a poor signal-to-background ratio.
In this chapter the PID for all channels will be studied and optimized. All relevant particles for this analysis together with their quantities can be found in Table 6.1.

6.3.1 PID for charged kaons

As discussed previously in section 3.2, especially the PID for charged kaons is difficult. Each of the three chosen S channels contains at least one K^+ so therefore one has to assure a sufficiently high purity of kaons in order to get potential S candidates. In Figure 6.4 the m^2 distribution for $\mathrm{d}E/\mathrm{d}x$ selected kaons of channel a) is shown. As expected the purity of kaons is very low if only $\mathrm{d}E/\mathrm{d}x$ selection is done and there is an order of magnitude more pion background. The distribution is fitted using a combined Student's-t function fit (in red) that contains three simultaneously fitted Student's-t functions describing each particle species. In a m^2 range of around 0.2 - 0.4 $(\mathrm{GeV}/c^2)^2$ a separation of kaons from other species with sufficient signal to background ratio is possible. One solution to assure a high kaon purity would be to apply a m^2 cut for each kaon, however this would cause a significant decrease in statistics because of the limited TOF efficiency. A more convincing strategy is to check for each $\mathrm{d}E/\mathrm{d}x$ identified kaon if there is an overlap in $\mathrm{d}E/\mathrm{d}x$ with other particles within $n\sigma < 2$. If not, then no m^2 cut is needed, otherwise an m^2 cut is applied. Then the m^2 is restricted to be in a range of $0.2 < m^2 < 0.35\,\mathrm{GeV}^2/c^4$, approximately a 1σ range, in which the S/B-ratio is sufficiently high and at least > 1. Furthermore it is reasonable to use the m^2 information if available, which should not decrease the signal but only the background. Accordingly, if there is a TOF hit, then the above mentioned cut is applied. Concerning the K^+, the three channels do not distinguish in principle, so kaon PID is done in the same way for all of them.

Properties of important particles			
particle	**lit. mass [GeV/c^2]**	**exp. mass [GeV/c^2]**	**cτ [cm]**
π^+	$0.13957039 \pm 1.8 \cdot 10^{-7}$	0.1371 ± 0.1133	780.4
K^+	$0.493677 \pm 1.3 \cdot 10^{-5}$	0.5073 ± 0.0524	371.1
p	$0.938272 \pm 6 \cdot 10^{-9}$	0.982991 ± 0.063264	∞
K^0_S	$0.497611 \pm 1.3 \cdot 10^{-5}$	0.498227 ± 0.004206	2.68
Λ	$1.115683 \pm 6 \cdot 10^{-6}$	1.115718 ± 0.001484	7.89

Table 6.1: Experimental masses are taken from Figure 3.4a, Figure 3.6 and Figure 3.7. Literature values of mass and τ are taken from [75]. The experimental masses for charged particles are obtained from the m^2 distribution, by applying a Gaussian fit. Due to the discussed systematic uncertainties in the m^2 determination (see section 3.2), the statistic fit error is quite large.

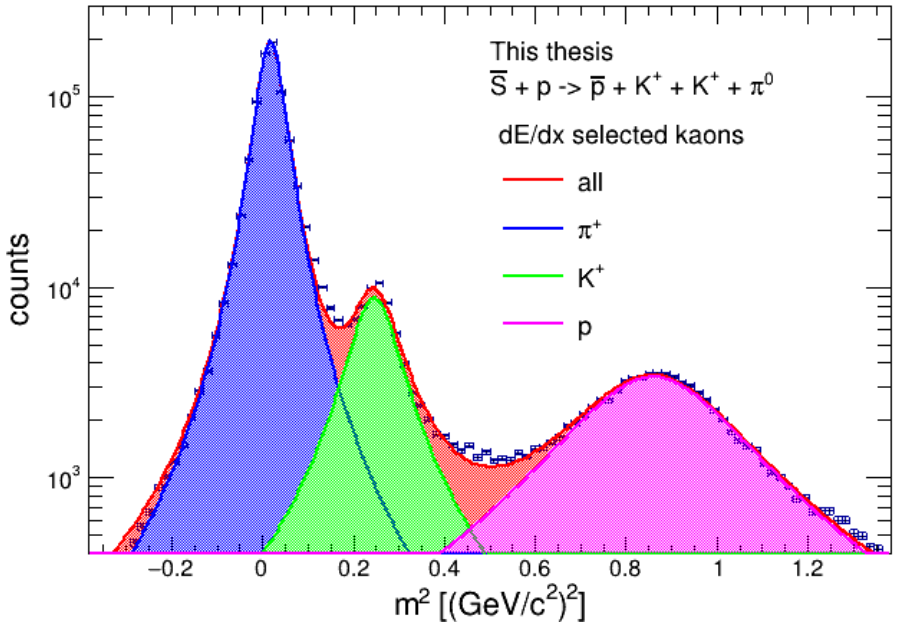

Figure 6.4: The m^2 distribution for dE/dx selected Kaons that are part of the S topology from channel a) is shown. A simultaneous Student's t function fit for all three particle species was performed.

6.3.2 PID for antiprotons

The $\bar{p}$ has to be identified for channel a) and b) and as daughter of the $\overline{\Lambda}$ of channel c). In section 3.2 was shown that generally (anti)protons are more separated in m^2 distributions than for example kaons from pions, which allows an easier PID. However, it was also demonstrated that depending on the momentum bin, $\mathrm{d}E/\mathrm{d}x$ cuts are not sufficient for the identification of $\bar{p}$ – see Figure 3.5b. It is necessary to study the PID for antiprotons that are part of the S topology separately, because they have different momentum distributions than primary particles as discussed in section 3.2. Analogously to Figure 6.4, the m^2 distribution for $\mathrm{d}E/\mathrm{d}x$ identified antiprotons of channel b) is shown in Figure 6.5. It is obvious that $\mathrm{d}E/\mathrm{d}x$ separation of (anti)protons is not sufficient and therefore m^2 cuts have to be used additionally. The most reasonable strategy in order to get the best purity with minimum loss in efficiency is to use the m^2 information if available and demand an m^2 range of $0.6 < m^2 < 1.2\,\mathrm{GeV}^2/c^4$ if there is an overlap in $\mathrm{d}E/\mathrm{d}x$ with other particles.

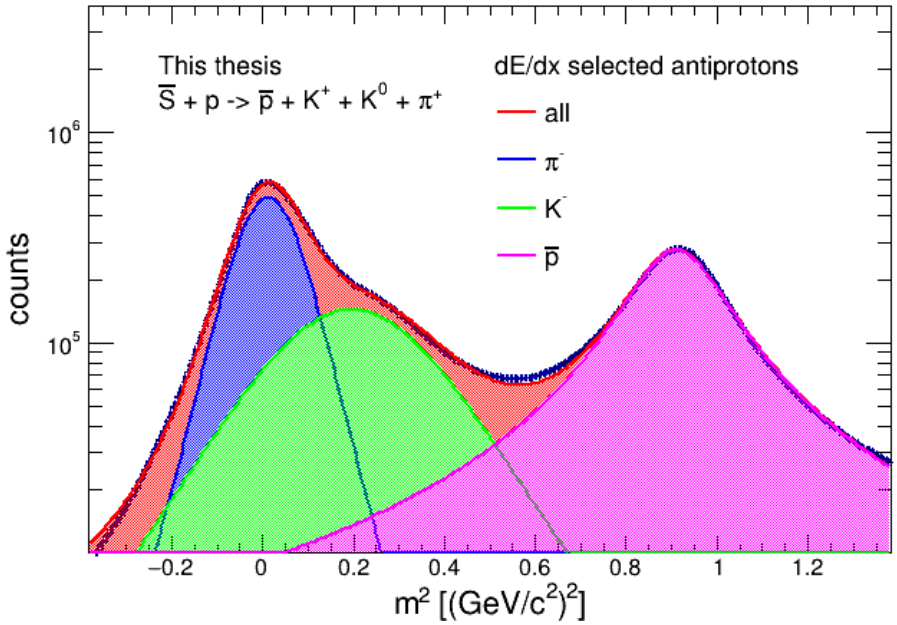

Figure 6.5: For $\mathrm{d}E/\mathrm{d}x$ selected antiprotons of channel b) the analogous procedure as in Figure 6.4 was done.

6.3.3 PID for pions

Due to the fact that pions are the most abundant particles even if $\mathrm{d}E/\mathrm{d}x$ cuts for other particle species are applied – see Figure 6.4 and Figure 6.5, it is sufficient to demand solely a $\mathrm{d}E/\mathrm{d}x$-cut for their identification. In this way already a reasonable S/B-ratio is achieved. So in general the PID for pions is straightforward, additionally only the

charge has to be taken into account.

6.3.4 PID for neutral particles

The neutral particles that play a role in the S reconstruction are the K^0 for channel b) and the $\overline{\Lambda}$ in channel c). In general they are reconstructed like in section 3.3. In addition to that, for $\overline{\Lambda}$'s a m^2-cut for the daughter antiproton is applied if there is an overlap in dE/dx with other particle species. This cut is necessary because in contrast to chapter 3 we are only looking for secondary neutral particles that are more rare than primary ones. Accordingly, the signal to background ratio is expected to be quite low. In the first level of analysis a 6σ cut[2] is applied to the kaons, so that there is enough background left in order to study if further cuts in the subsequent analysis reveal a K^0 peak. For analogous reasons the invariant mass of a $\overline{\Lambda}$ in channel c) is restricted to be within a 4σ window. The σ range for $\overline{\Lambda}$ was chosen narrower because we generally expect more S vertex candidates from channel c) than from b). This is due to the fact that for channel b) the S V^0 must consist of K^+ and antiproton, while for channel c) there has to be a pion instead of the antiproton and there more pions than antiprotons. Accordingly the number of potential $\overline{\Lambda}$s is kept lower to decrease combinatorics. How the invariant mass spectrum of K^0s and Lambdas is affected by cuts on the S candidate topology and especially the radial dependence will be studied in section 6.6.

6.4 Background estimation by anti-channel

It was discussed previously which reaction channels for the S are possible and how their topology would be. If we would not find any S candidate that fulfills a set of reasonable topological and PID cuts for any channel, then our result would be clearly that either the S does not exist or we are not able to detect it within the given statistics. However, if we find S candidates and even if we assume that their topology and PID is perfect (which is of course not assured), this would be very interesting but we can not conclude much from that. The problem is, that we do not have any estimation for combinatorial, random background sources or any other yet unknown background contribution. Theoretically an invariant mass reconstruction of the S that delivers a sharp peak would be a prove for its existence, however that is unreasonable optimistic, because as already studied in the simulation in section 5.3, the Fermi-momentum of the proton leads to a significant broadness of the invariant mass peak. Therefore we must have some estimation for the background, that we obtain by looking at the so called 'anti-channel' for each reaction channel. These anti-channels are made of the same particle species as the corresponding reaction channel, but each particle is replaced with its antiparticle (see for comparison section 5.2):

ā) anything $\rightarrow p + K^- + K^- + \pi^0$

[2]This means that the interval $[\mu - 6\sigma, \mu + 6\sigma]$ is chosen, where μ and σ are the parameters of the Gaussian obtained from fig. 3.6

$\bar{b}$) anything $\rightarrow$ p + K^- + K^0 + π^-

$\bar{c}$) anything $\rightarrow$ Λ + K^- + π^+ + π^-

The advantage of studying these anti-channels is, that the reaction (written as 'anything') can principally not be an interaction of the S. Simply reversing the reaction particles of channels a) to c) would lead to an interaction of $S + \bar{p}$ which is impossible due to the lack of antiprotons in the detector material. Therefore the anti-channels have to be 'anything' else and can be used in order to describe the background. If a fake S candidate emerges for example from a combination of decaying primary particles then the corresponding primary antiparticles would exist in equal amounts at those energies [76], so that there would be an analogous candidate in the anti-channel. Of course, in order to be able to compare S channels to their corresponding anti-channel, one has to use exactly the same topological and PID cuts, except for the charge.

6.5 Channel a) $\overline{S}$ + p $\rightarrow$ $\bar{p}$ + K^+ + K^+ + π^0

Channel a) was chosen because of its relatively simple topological structure – only one vertex has to be reconstructed – and the uncomplicated PID because we only detect charged particles. However there are also disadvantages with regard to this channel. In particular the π^0 is undetected, hence there is a missing particle in the invariant mass reconstruction, causing a broad distribution – as discussed in section 5.3. The lack of a detected neutral particle (like the K^0 in channel b) or the $\overline{\Lambda}$ in channel c)) might be an advantage for the simplicity of reconstruction, however due to that, methods like described in section 6.6 cannot be applied for channel a). Moreover a sideband analysis cannot be done for this channel. Therefore we do not expect to get meaningful results by analyzing channel a) however for completeness it will be discussed here. The previously described 'anti-channel method' can be applied for channel a) and an invariant mass reconstruction can be done although the contribution of the π^0 is missing. The invariant mass distribution for the reconstructed mass m($\bar{p}$,K^+,K^+) respectively m(p,K^-,K^-) of channel a) and its corresponding anti-channel can be seen in Figure 6.6. An m^2 overlap cut for all charged particles is applied and the restriction $r > 40\,\text{cm}$ is used. In general there is an asymmetry between the channel and its anti-channel. The reason for that might probably be that in the anti-channel the K^- could be misidentified as π^- which together with the proton is associated to a decaying Λ. This Λ might be produced regularly in (fixed target) nuclear interactions in contrast to the $\overline{\Lambda}$ which is produced less frequent due to baryon number conservation. Accordingly the same argument does not hold for the channel which might cause the asymmetry. In principle we cannot conclude anything from the invariant mass distribution with regard to the existence of the S.

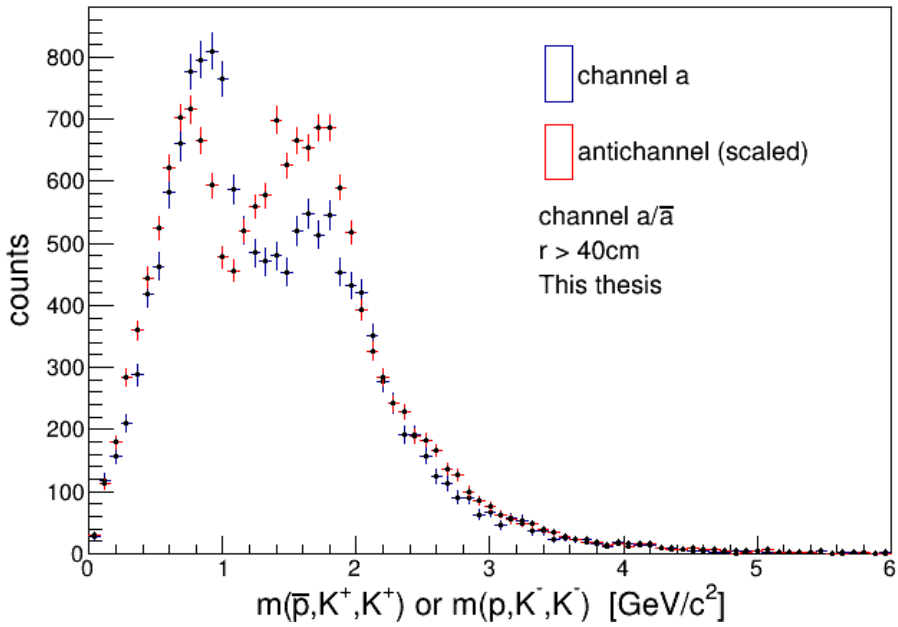

Figure 6.6: Reconstructed invariant mass for channel a) and its corresponding anti-channel. The S candidates fulfill the restriction $r > 40\,\mathrm{cm}$ and an m^2 overlap cut is applied on proton/antiproton and both kaons.

6.6 Analysis of invariant mass distributions

The general strategy of this chapter is to study invariant mass spectra of the K^0 respectively $\overline{\Lambda}$ in channel b) and c) in dependence of topological and PID cuts. As discussed in section 3.4, secondary neutral particles are almost unresolvable over the dominating background. However, if we demand the complex topology of S reaction channels, as described in section 6.2, it might be possible that some true K^0s or $\overline{\Lambda}$s become visible in the invariant mass distributions. If a true secondary neutral particle exists that belongs to an S candidate at high radii, this would be a serious hint for the existence of the S. Regarding S candidates at high radii ($r \gtrsim 40\,\mathrm{cm}$) is a convincing strategy, because as described in section 5.4 due to the material budget of the ALICE detectors, we expect about 40% of the nuclear S interactions in our detection range to happen in that region. Despite this loss in statistics, our gain is that the background is reduced drastically. Possible background sources, like e.g. decaying particles and normal nuclear events which coincidentally fulfill our topology demands due to combinatorics, mainly happen in the vicinity of the primary vertex. Accordingly, detecting a S candidate at higher radii would be a more serious hint for the existence of the S. In the following chapters, the applied topological and PID cuts on the S candidates will be varied and the effect on the invariant mass distributions will be studied. A comparison of channel

and anti-channel – as described in section 6.4 – is used as background estimation and differences might be interesting indications.

This analysis is based on two $\sqrt{s} = 5.02\,\text{TeV}$ Pb-Pb data sets from 2015 and 2018. In general these two data sets are similar but according to differences in multiplicity and triggering – see section 6.6.2 – the results from these sets are compatible but not identical. Therefore the 2015 data will be analyzed first for K^0s in section 6.6.1.

6.6.1 Channel b) ($\overline{S} + \text{p} \rightarrow \bar{\text{p}} + \text{K}^+ + \text{K}^0 + \pi^+$) 2015 data first cut combination

This section deals with the invariant mass spectra of π^+/π^- vertices that are part of the channel b) topology. In the following, the particles associated with these vertices/spectra will be called K^0s, although they might not be an actual K^0, but combinatorial background. Our overall strategy is to study whether true secondary K^0s exist that belong to a S candidate at high radii. In order to get meaningful results, there has to be some comparison to possible combinatorial background which is achieved using the anti-channels. In general, there there is an extreme variety of possible cuts, as described in section 6.2 and 6.3. Our strategy was to set a basic cut combination first and then secondly vary other cuts, which allows studying the effect on the invariant mass distribution. We applied the following fixed cut combination (*combi*1), which seemed to be reasonable: dist(K^0,S) $> 0.5\,\text{cm}$, dca(prim,K^0-$\pi^{+/-}$) $> 2\,\text{cm}$, dca(S,K^0-$\pi^{+/-}$) $> 0.2\,\text{cm}$ and the PID 'overlap' cut on $\bar{\text{p}}$ and K^+. The cuts dca(K^0,prim) $> \text{dca}_{\text{min}}$ and distance(prim,S) $> r_{\text{min}}$ were then varied. For explanation of used abbreviations see section 6.2.

In Figure 6.7 three invariant mass spectra of the reconstructed K^0s are shown – scaled as described in the legend. The following cut combinations are used: $r > 5\,\text{cm}$ and dca(K^0,prim) $> 0.5\,\text{cm}$; $r > 10\,\text{cm}$ and dca(K^0,prim) $> 1\,\text{cm}$; $r > 40\,\text{cm}$ and dca(K^0,prim) $> 3\,\text{cm}$. Regarding the distribution for the lowest radial cut, one can recognize an increase at the expected K^0 invariant mass. This is most likely due to primary K^0s, whose daughters are imprecisely reconstructed, and that coincidentally points back towards the nuclear interaction S vertex. Due to the loose dca(K^0,prim) cut, some of them contribute to the small increase.

As expected, for larger distances between primary and S vertex (e.g. $r > 10\,\text{cm}$) and if a higher dca(K^0,prim) is demanded, the invariant mass distribution seems to become flat. This might be due to the reason that there are no primary K^0_S left because of their short decay length, if one assumes that dist(K^0,prim) $>$ dist(S,prim), so that in principle the K^0s fly forwards compared to the momentum of the S. Another reason is of course the stricter dca(K^0,prim)-cut that should exclude even imprecisely reconstructed primary tracks.

Interestingly, as shown in Figure 6.7, there seems to appear again a K^0 peak for large radii, when the background decreases. This contradicts our expectation, that for large radii and dca(K^0,prim) $> 3\,\text{cm}$ there should not be any primary K^0 remaining as background source, and if that peak really corresponds to secondary hadronic interactions, this might be a hint for the existence of the S.

Comparing Figure 6.7 to Figure 6.8 demonstrates, that the anti-channel generally shows the same behaviour like the S channel, so for a small dca(K^0,prim) cut, the primary K^0s are visible but they vanish if this cut and the radial distance is increased. However the supposed K^0 peak at large radii only appears for the S channel and not for the anti-channel which supports the thesis, that this might not be background. Possibly this could have been a few real S events that were covered by background for smaller radii. However a further inspection of these candidates revealed another explanation.

The distance- and angular distribution of the K^0s from Figure 6.7 (red) are shown in Figure 6.9a respectively Figure 6.9b. We consider the distance between K^0 and S vertex as well as the angle between the connection vector from primary to S vertex and momentum of the K^0 (in the following abbreviated as 'angle'). Firstly one notices that the distances are unreasonably large as expected for K^0s that originate from the S vertex. Even for high momenta kaons, one would anticipate a distance distribution around the mean decay length L, that is $\approx 16\,\text{cm}$ for $3\,\text{GeV}$ K^0s. In our case however, there is an increase in the distribution, starting at dist $\approx 45\,\text{cm}$. Remembering that we demand $r > 40\,\text{cm}$ for the S and a minimum $r > 5\,\text{cm}$ is set for each V^0, the increase can be explained by K^0s on the opposite side of the primary vertex (viewed from the S vertex). This conjecture is confirmed by the distribution of the angle between the vector from primary to S vertex and that one from S vertex to the K^0 – see Figure 6.9b. The majority of the K^0s seem to be emitted backwards, if one assumes that they truly originate from the S vertex. An emission in an angle of $> 120°$ is not forbidden, but pretty unlikely due to total momentum conservation and in fig. 5.2b the expected angular distribution can be seen which does not agree with the observation. Combining the results of these distributions, we conclude that the 'peak' in the S channel is not associated to the S. On the contrary, this seem to be nonprimary K^0s which are likely produced in nuclear interactions close to the primary vertex and coincidentally point back towards the S. As discussed in chapter 4, there are many nuclear interactions occurring in the vicinity of the primary vertex, so it is possible that despite the large distance, some of them point towards the S vertex. However this does not explain why in the anti-channel – see Figure 6.8 – no K^0 peak is visible. The number of S candidates for the anti-channel is higher, which can be explained by the fact that due to baryon number conservation in nuclear events, there are more protons created than antiprotons. Accordingly, the combinatorial background for the anti-channel which has a proton as daughter of the S V^0, is higher than for the channel. Anyway the previously discussed nuclear K^0s should also coincidentally point back towards the anti-channel in the relative same amount.

The next step is to study the S channel, avoiding these K^0s from nuclear interactions, which will be done in section 6.6.3. However, in this section both data sets will be used and therefore it is reasonable to do a qualitative comparison of them first which is discussed in section 6.6.2.

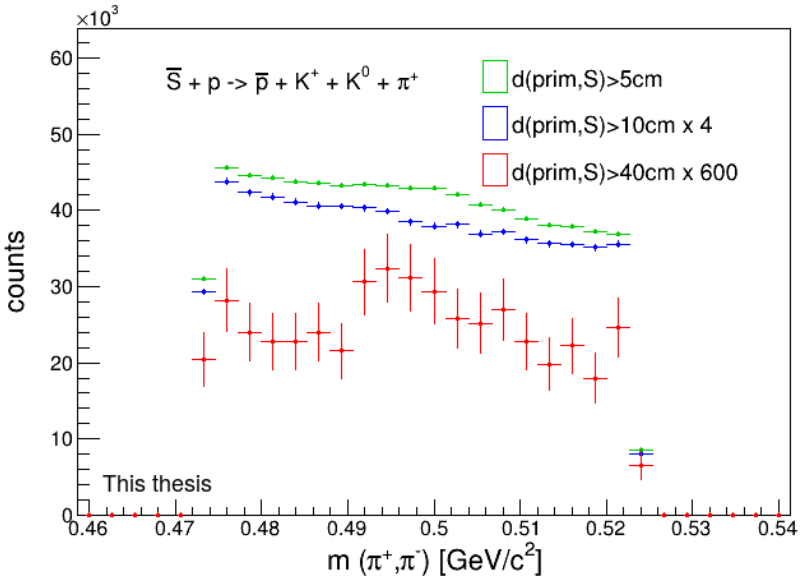

Figure 6.7: Invariant mass distribution of K^0 that is part of channel b) topology with cut *combi*1 applied. The cut d(prim,S) and dca(K^0,prim) is varied as described in the legend respectively text. For $r > 40\,\text{cm}$ and dca(K^0,prim) $> 3\,\text{cm}$ seems to appear a peak corresponding to 'true' K^0s.

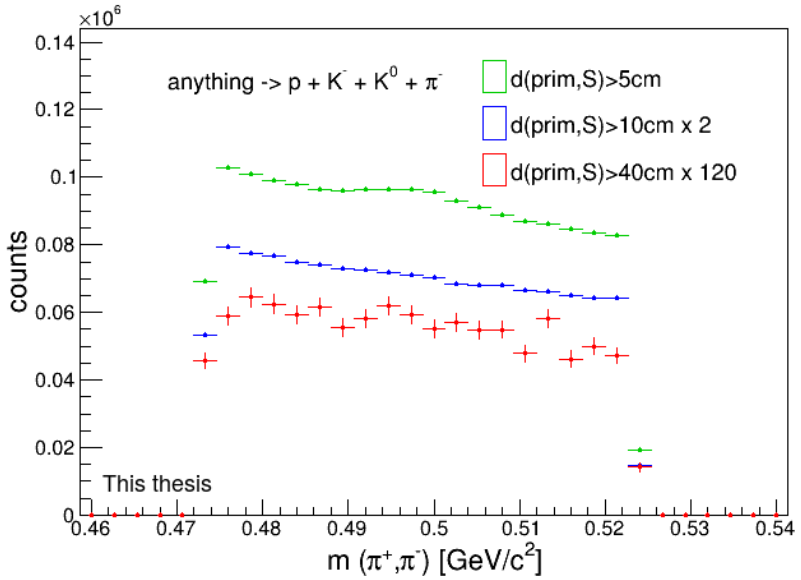

Figure 6.8: Analogous content as in Figure 6.7 but for anti-channel. Cut *combi*1 is applied and for higher radii no peak can be seen.

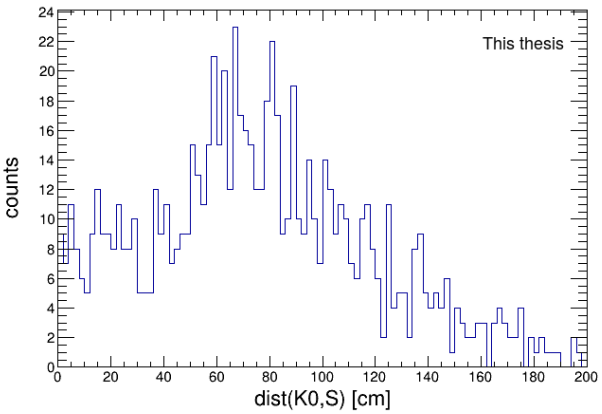

(a) Distribution of distance between K^0 and S vertex

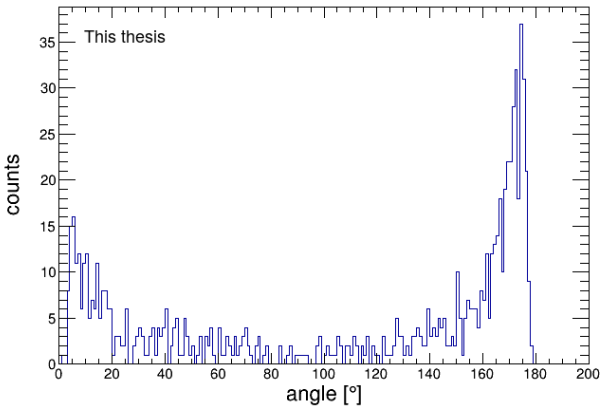

(b) The distribution of the angle between connection vector from primary to S vertex and momentum of K^0 is shown.

Figure 6.9: Distribution of distance respectively angle for K^0s in Figure 6.7 (red distribution) which fulfill $r > 40\,\text{cm}$ and dca(prim,K^0) $> 3\,\text{cm}$.

6.6.2 Qualitative comparison of 2015 and 2018 data

In this section the data sets of $\sqrt{s} = 5.02\,\text{TeV}$ Pb-Pb collisions from 2015 and 2018 will be compared shortly in particular with regard to the multiplicity. Additionally to the 2015 data, we included the 2018 data in order to increase statistics, because – as shown in section 5.4 – we expect the number of detectable S candidates to be only of the order $O(10^1)$ to $O(10^2)$ if both data sets are used. A full comparison analysis would exceed the scope of this thesis, hence we will just mention possible differences and discuss the compatibility of both data sets. In Figure 6.10 the multiplicity distribution for all events of the 2015 and 2018 data can be seen. For comparison, the histograms are scaled so that both have the same integral. The multiplicity distribution differs significantly. In the 2015 data set the number of events decreases continuously for increasing multiplicity, typical for minimum bias selected events. In contrast, for the 2018 data set obviously a multiplicity trigger was used in order to increase the number of central events. Accordingly, this can cause differences in signal-to-background ratios for various distributions that are regarded for both data sets separately. Anyway both data sets can be used combined in order to increase statistics.

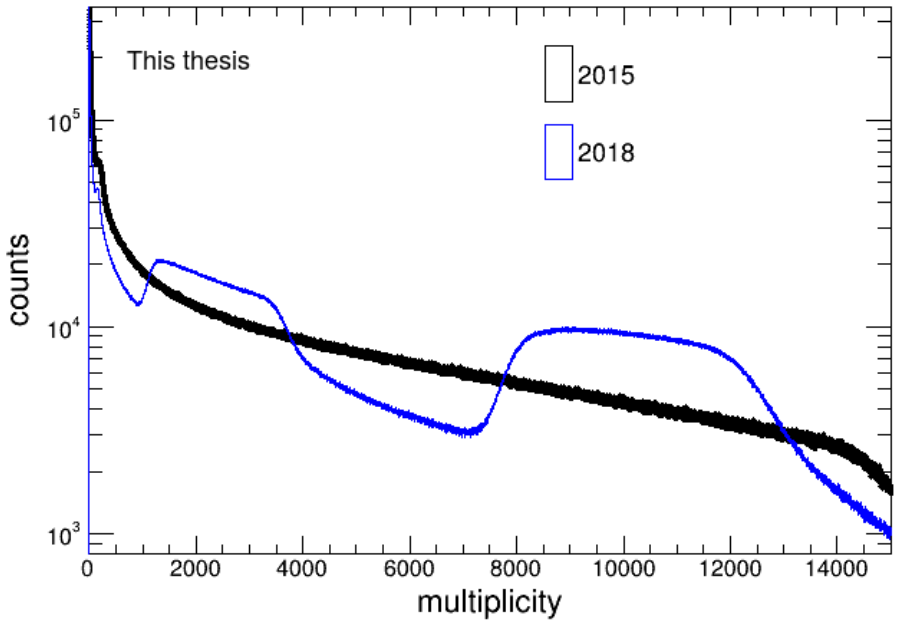

Figure 6.10: Comparison of multiplicity distribution for 2015 and 2018 data set. The 2015 data were scaled by a factor of 1.88.

6.6.3 Full statistic analysis of channel b) $\overline{S} + p \rightarrow \bar{p} + K^+ + K^0 + \pi^+$

As discussed in section 6.6.1 there are K^0s produced in nuclear interactions in the vicinity of the primary vertex which coincidentally point towards the S vertex and therefore contribute as background source. These K^0s have a large distance to the S vertex and fly 'backwards', so their angle to the supposed S flight direction is high – see fig. 6.9a and fig. 6.9b.

Cut combination 2

In order to avoid this background distribution one can restrict the distance of K^0 and S to a reasonable value and/or set an upper limit to the angle between the connection vector from primary to S vertex and K^0 momentum (in the following called angle). That is why the following topology cut combination (*combi*2) is used: $0.5 < \text{dist}(K^0, S) < 20\,\text{cm}$, angle $< 120°$, dca(prim,K^0-$\pi^{+/-}$)$> 2\,\text{cm}$ and dca(S,K^0-$\pi^{+/-}$) $> 0.2\,\text{cm}$. The lower limit of dca(prim,K^0) is set depending on the distance of primary vertex and K^0 (r_{K0}), using the relation: $0.075 \cdot r_{K0} + 0.125$. As discussed earlier, due to the complicated topology and PID, it is not possible to use a 'brute force' method for all cut combinations in order to get the best efficiency and purity combination. Therefore we have to make a best guess which restrictions are reasonable, so in the following will be discussed, why the above mentioned cuts should identify real S events, while decreasing background. For

a mid-range momentum K^0, the mean path length is around L$\approx$ 3 cm, so demanding $0.5 < \text{dist}(K^0, S) < 20$ cm will keep nearly all real S events, while background like nuclear events close to the primary vertex but distant from the S vertex will be cut out for $r > 40$ cm of S to prim. Also the expected angular distribution – see Figure 5.2b – mostly shows quite small angles, so demanding angle $< 120°$ will only slightly decrease the number of detected real S events. One has to exclude, that the K^0-daughters originate from the S vertex, so therefore it is reasonable to demand dca(S,K^0-$\pi^{+/-}$) > 0.2 cm, while this lower limit is kept low, because small distances like 0.5 cm of K^0 and S are possible and accordingly the daughter pions can be close the S vertex. In contrast to cut *combi*1 it makes more sense to demand a low limit of dca(prim,K^0) that depends on r_{K0}, because generally the more distant the K^0 is from the primary vertex, the more imprecise the back pointing of the reconstructed momentum vector might be and it could originate from the primary vertex, although the momentum vector does not directly point towards the primary vertex. Hence a higher low limit for dca(prim,K^0) has to be demanded. We used the same condition as in section 3.4 that for $r_{K0} = 5$ cm it must hold that dca(prim,K^0)> 0.5 cm and for $r_{K0} = 25$ cm one demands dca(prim,K^0) > 2.0 cm. A linear interpolation between these two points leads to the relation described above.

With regard to the PID we separately studied the invariant mass spectra if strict 'overlap' cuts for antiproton and K^+ are applied and also without this restriction. Apart from the mentioned topology cuts in *combi*2, the previous discussion in section 6.6.1 suggests to study S candidates at higher radii (at least $r > 35$ cm). The resulting invariant mass spectra together with the anti-channel are shown without PID 'overlap' cut for 2015 data in fig. 6.11a respectively for 2018 data in fig. 6.11b. As one can see, in both distributions there is an excess at the expected K^0 mass in the channel but not in the anti-channel. For the 2015 data this seems to be more significant. Both data sets combined lead to the invariant mass distribution shown in fig. 6.12a. We apply a Gaussian together with a straight line fit as shown in Figure 6.12b. Subtracting the background from the Gaussian leads to Figure 8.7. The same procedure was done for the K^0s that are associated to an S candidate, whose antiproton and K^+ are identified with a m^2 overlap cut in addition to the $n\sigma$ cut. As expected, the application of the overlap cut results in a large decrease in statistics, as discussed in section 3.2 and section 5.4. In general we can conclude that in both cases secondary K^0s that are associated to an S candidate at high radii can be found, even if we exclude unrealistic topologies like backwards flying K^0s. The significance z of this 'peak' can be calculated using $z = \text{signal}/\sqrt{\text{signal} + \text{background}}$, where the signal is the difference between Gaussian and background fit, integrated in a range of $2\sigma_{\text{Gauss}}$ besides the mean of the Gaussian. This leads to a value of $z = 2.3$ (without overlap) and $z = 2.8$ (with overlap cut). A further discussion of this result will be done in section 6.8. Of course the mentioned distributions were also studied for various other radial cuts and slight changes of topology cuts in *combi*2, however for larger radii the decrease in statistics lowered the significance of the K^0 peak. So the shown distributions in this section are the most noticeable ones. Another possibility for topological cuts will be discussed in section 6.6.4.

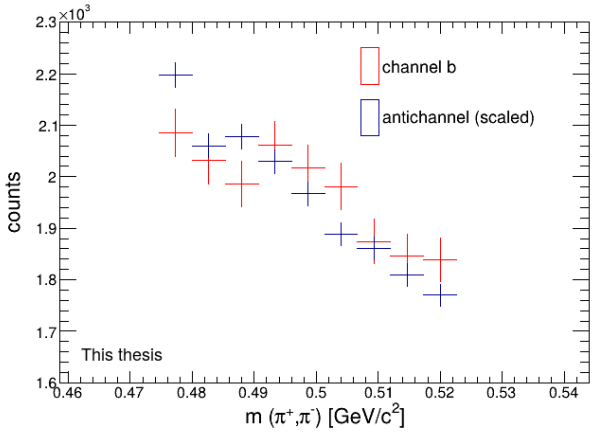

(a) 2015 data

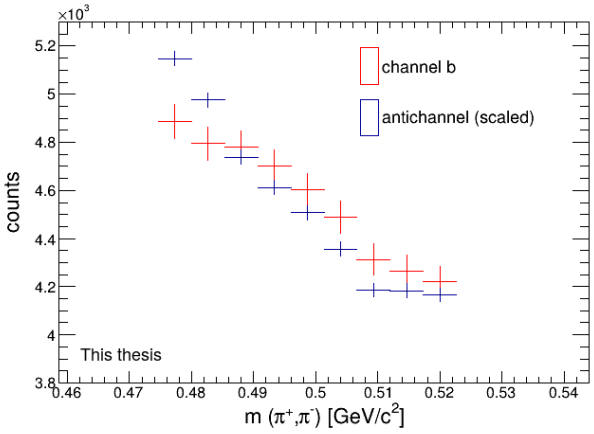

(b) 2018 data

Figure 6.11: Invariant mass distributions of K^0s that are associated to S candidates of channel b) or the corresponding anti-channel. Cut *combi*2 is applied and $r > 35\,\text{cm}$ is demanded. No 'overlap' PID cut is used.

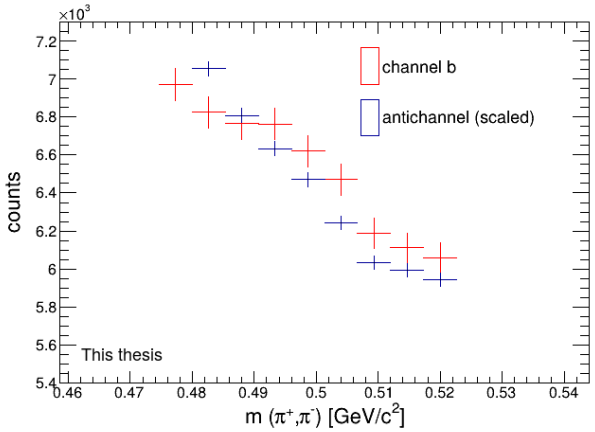

(a) Contents of Figure 6.11 combined.

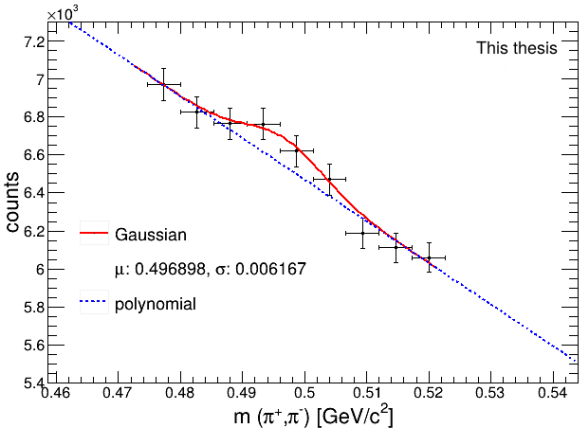

(b) A Gaussian combined with background fit is applied to K^0s of channel b.

Figure 6.12: Invariant mass distribution of K^0s that are associated to S candidates of channel b) or anti-channel which fulfill cut *combi*2 and $r > 35\,\text{cm}$. The peak for channel b) has a significance of $z = 2.3$

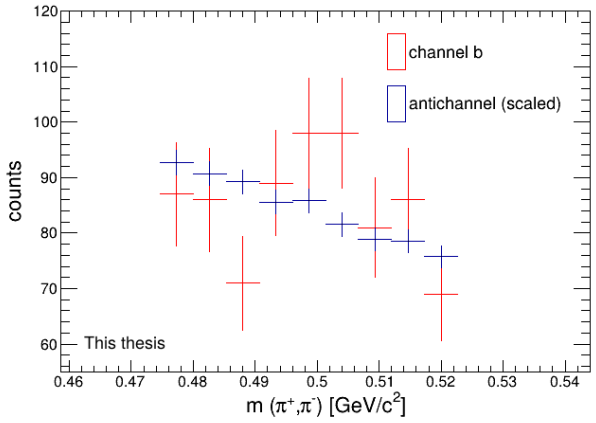

(a) Analogous to Figure 6.12a but in addition an m^2 overlap cut is applied for the K^+ and $\overline{p}$ of S candidates.

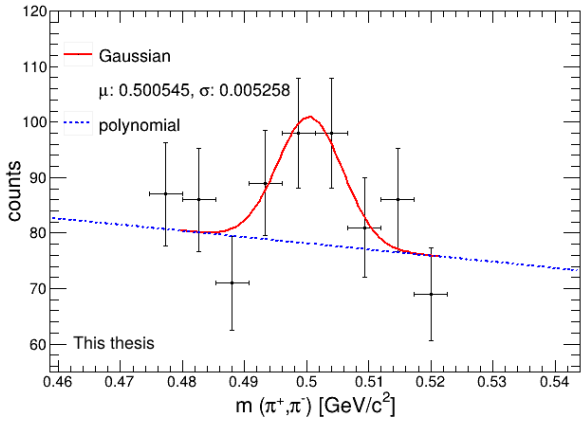

(b) Gaussian fit combined with background fit applied to the distribution for channel b) in Figure 6.13a.

Figure 6.13: Invariant mass distribution of K^0s that are associated to S candidates of channel b) or corresponding anti-channel which fulfill cut *combi*2, $r > 35\,\text{cm}$ and moreover an m^2 overlap cut is applied on the K^+ and $\overline{p}$ of S candidates. The peak for channel b) has a significance of $z = 2.8$.

6.6.4 Detector material cut

Another reasonable strategy is to use the information about the detector structure and distribution of normal nuclear events from chapter 4. This explicitly allows to cut additionally on spatial areas, where we expect nuclear interaction to occur and areas which are dominated by background can be avoided. For this cut, called 'detector material cut', we demanded the orthogonal radius r_o to be in the interval of $55 < r_o < 64\,\text{cm}$ or $75 < r_o < 85\,\text{cm}$ based on Figure 4.1, which is shown again in Figure 6.14, where the cut ranges are visualized. Furthermore we saw in Figure 4.3 that the central η range is dominated by background, but the outer η ranges are better resolvable. Thats why the detector material cut also allows S events which happen in the visualized areas in Figure 6.15 and additionally fulfill $r > 35\,\text{cm}$. The comparison of channel b) and anti-channel without overlap cut can be seen in Figure 6.16a for the 2015 data and in fig. 6.17 for both data sets. Similarly to fig. 6.12a a peak is slightly visible for channel b) for the 2015 data, however for the 2018 data it is only barely resolvable. Applying a Gaussian and background fit, as shown in fig. 6.17, reveals that this peak has a significance of about 2.2 for the 2015 data. Performing a Gaussian fit to both data sets was not reasonably possible. The analogous study for the detector material cut with additional overlap cut will not be discussed due to insufficient statistics in that case. In conclusion we did not achieve an improvement in significance by applying the detector material cut.

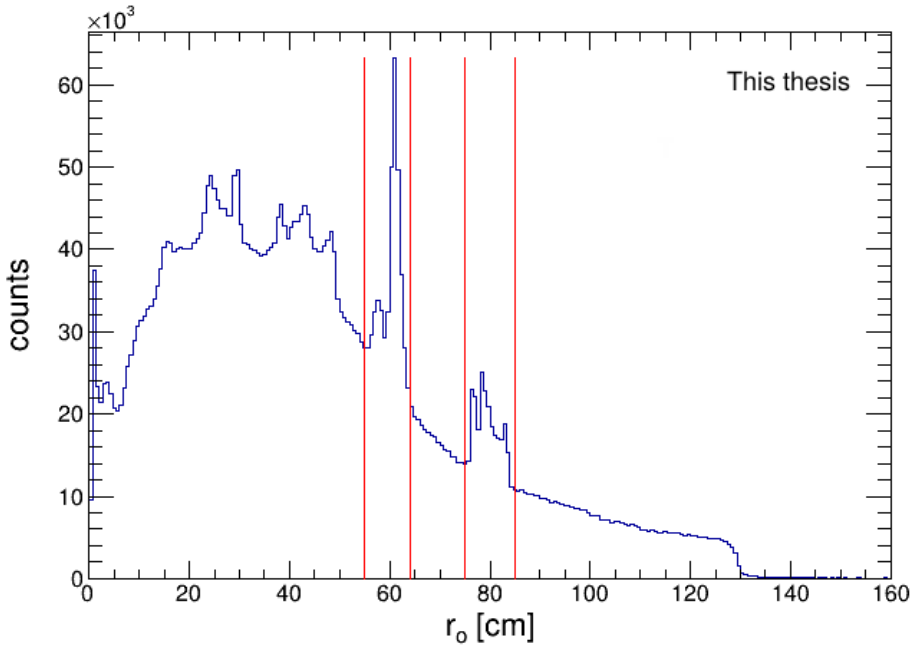

Figure 6.14: Distribution of 'normal' nuclear events – same content as Figure 4.1. The red lines indicate the r_o ranges included in the 'detector material cut'.

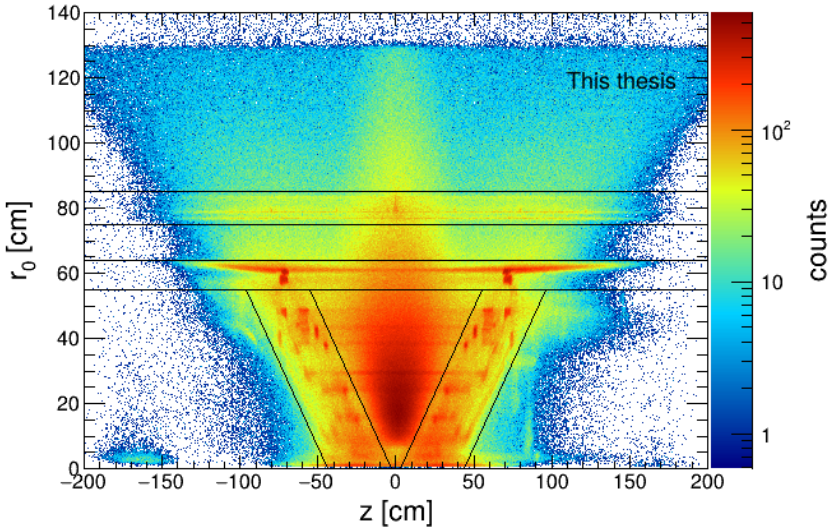

Figure 6.15: r_o vs z coordinate of normal nuclear events – same content as Figure 4.3. The black drawn 'boxes' indicate the topological areas which are included in the 'detector material cut'.

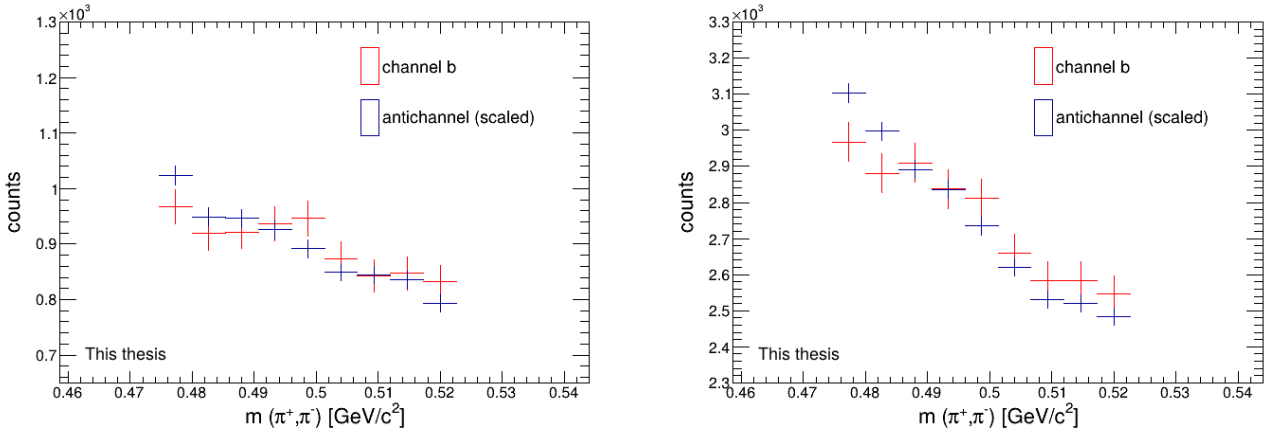

(a) 2015 data set.

(b) Both data sets.

Figure 6.16: The invariant mass distribution for the K^0s with applied 'detector material cut'.

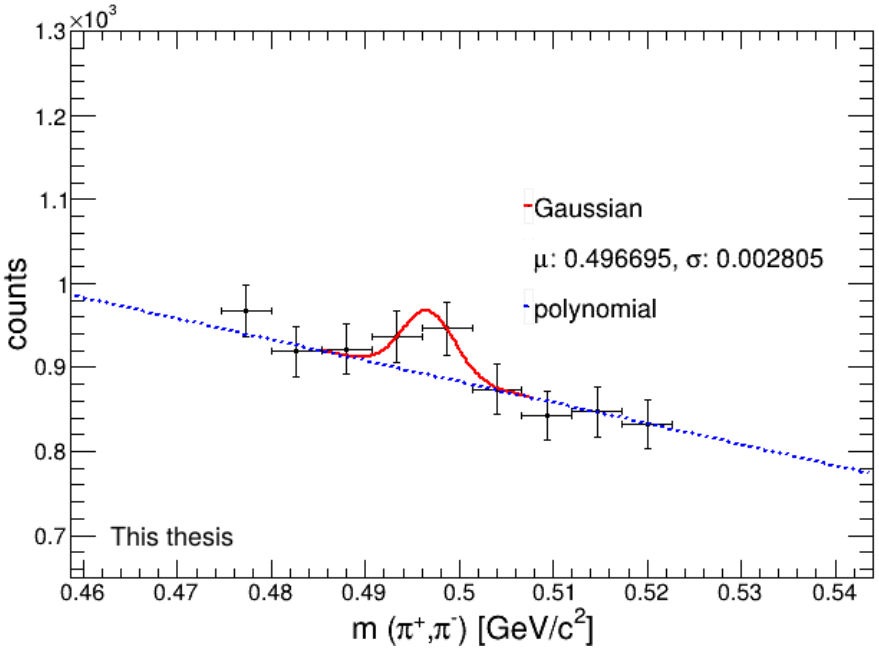

Figure 6.17: A Gaussian fit combined with a linear background fit was performed for the 2015 data. The peak has a significance of $z = 2.2$.

6.6.5 Full statistic analysis of channel c) $\overline{S} + p \rightarrow \overline{\Lambda} + K^+ + \pi^- + \pi^+$

In principle the same strategies like in section 6.6.3 can be applied for channel c), therefore this chapter will not discuss the method in detail but rather lists the applied cuts and shows the results. The PID for all final particles is done as described in section 6.3 and additionally an overlap cut is done for the daughter antiproton of the $\overline{\Lambda}$. Due to the fact, that the topology of channel c) is nearly identical to that of channel b), similar topology cuts can be applied. One result of section 6.6.1 was, that a maximum limit for the distance between S and neutral particle (in this case the $\overline{\Lambda}$) and an angular cut is required. Therefore the following set of cuts is used for the topology of channel c):

- $1 < \text{dist}(\overline{\Lambda}, S) < 35\,\text{cm}$
- angle $< 120°$
- dca(prim,$\overline{\Lambda}$-$\bar{p}$) $> 1\,\text{cm}$
- dca(prim,$\overline{\Lambda}$-π^+) $> 1\,\text{cm}$
- dca(S,$\overline{\Lambda}$-$\bar{p}$) $> 0.4\,\text{cm}$
- dca(S,$\overline{\Lambda}$-π^+) $> 0.4\,\text{cm}$
- dca(prim,$\overline{\Lambda}$)$>$ dca$_{\text{min}}$ where dca$_{\text{min}}$ depends on dist(prim,$\overline{\Lambda}$)

The allowed distance range is set higher due to the larger $c\tau$ – see table 6.1. Due to that larger mean distance, also higher limits can be set to dca(prim,$\overline{\Lambda}$-daughters). In order to assure that the $\overline{\Lambda}$ is nonprimary, the cut dca(prim,$\overline{\Lambda}$)$>$ dca$_{\text{min}}$ is used, while dca$_{\text{min}}$ depends on the distance dist(prim,$\overline{\Lambda}$) in the analogous way as described in the previous section 6.6.3. Firstly it was regarded, how the invariant mass distributions of the $\overline{\Lambda}$ depends on the distance(prim,S) (radial) cut. The resulting invariant mass distributions of the $\overline{\Lambda}/\Lambda$ can be seen in Figure 6.18 respectively Figure 6.19. Similarly to the K^0s, for small radii there is an excess over the background in the distribution at the expected Λ mass. This can be explained either by imprecisely reconstructed primary $\overline{\Lambda}$s or by nuclear interactions that happen in the vicinity of the primary vertex and lead to the production of a $\overline{\Lambda}$. Some of these nuclear interactions might be located radially more distant from the primary vertex than the S vertex. Accordingly the corresponding $\overline{\Lambda}$ could coincidentally point back towards the S (with an angle that is small enough) and due to the high density of tracks and nuclear events in the vicinity of the primary vertex, this could lead to a small peak. Considering S candidates at higher radii, the above mentioned background sources generally disappear, especially because we demand the angular restriction. As Figure 6.18 shows, we can not see a peak that could correspond to $\overline{\Lambda}$s for radii e.g. larger than 20 cm or 35 cm. Various cut combinations like the demand for 'overlap' cuts or not, the 'detector material cut' and changes in the above described set of cuts were tested – see fig. 6.20. However it was not possible to resolve a distinct peak for $\overline{\Lambda}$s that are associated to an S candidate of channel

c) at high radii. Only for the 2015 data with overlap cut and $r > 40\,\mathrm{cm}$ a peak could be suspected – see Figure 6.21. The corresponding anti-channel does not show a similar peak. Applying a Gaussian fit to the channel c) distribution leads to a significance of $z = 2.3$. In general there might be several reasons why no significant peak can be found for most cut combinations. We only used a 4σ invariant mass interval in the basic cuts as described in section 6.3.4 which might have been an inaccuracy because due to that it is hard to estimate the background for the invariant mass distributions. Furthermore the applied m^2 cuts might be necessary in order to achieve a sufficient purity, however due to the uncertainties in the time-of-flight measurement for secondary tracks this might reduce the efficiency significantly. Moreover the statistic for high radii is too low to conclude something from that.

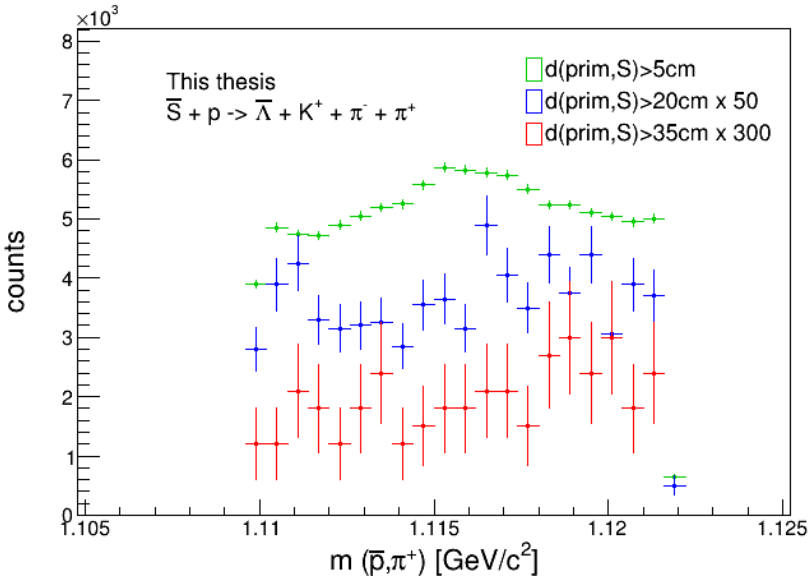

Figure 6.18: Invariant mass distribution of $\overline{\Lambda}$s that are associated to channel c) for different radial restrictions. Used topological and PID cuts are explained in the text.

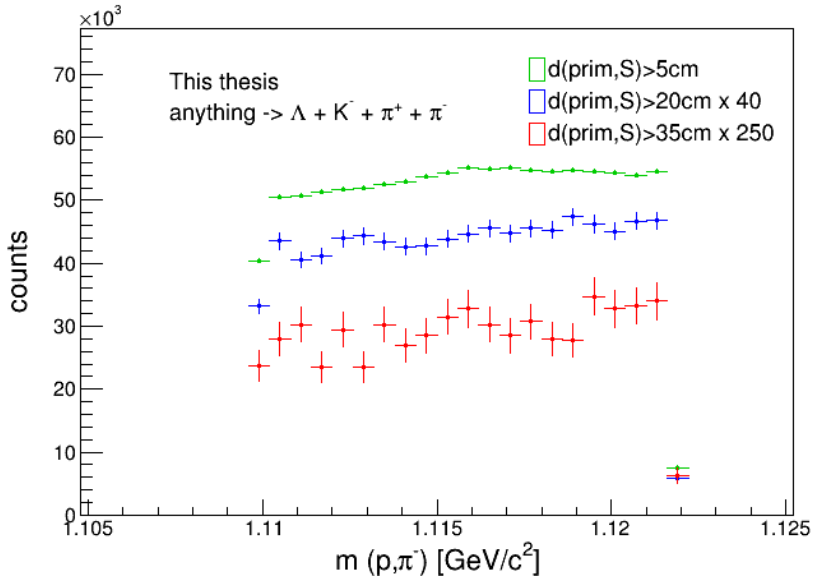

Figure 6.19: Analogous to Figure 6.18 but for Λs from the anti-channel.

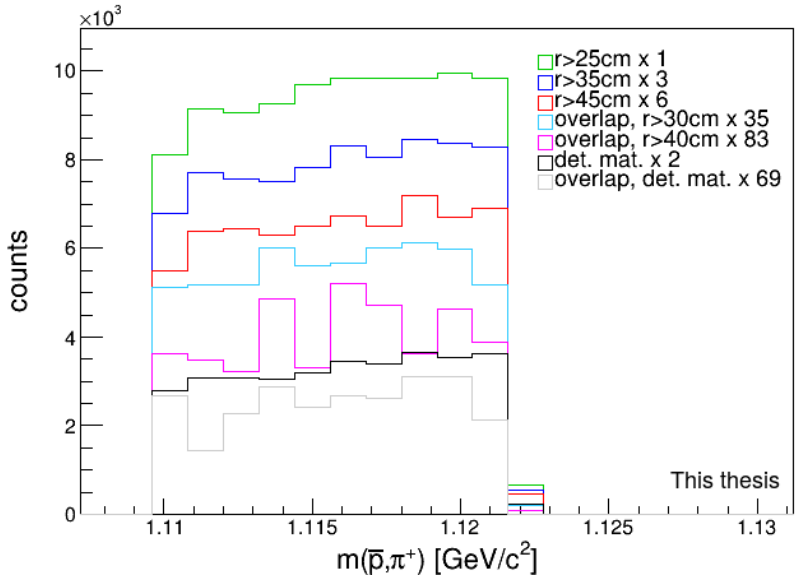

Figure 6.20: Invariant mass distribution of $\overline{\mathrm{p}}, \pi^+$-vertices that are associated to an S candidate of channel c). Different variations of topological and PID cuts are shown – scaled as indicated in the legend. The abbreviation 'overlap' stands for the demanded m^2 cut for $\overline{\mathrm{p}}$ and K^+ if there is an overlap in $\mathrm{d}E/\mathrm{d}x$. The term 'det. mat.' means the detector material cut described in section 6.6.4. No significant peak can be seen for any cut combination.

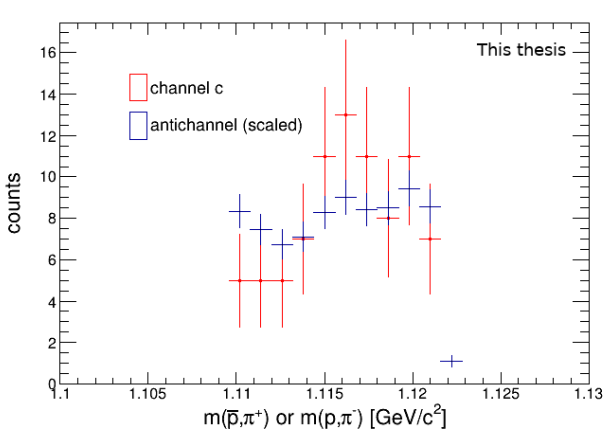

(a) Comparison of channel and anti-channel.

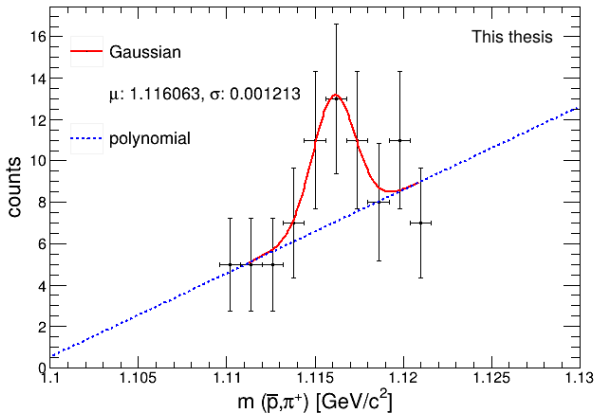

(b) A Gaussian combined with polynomial background fit was performed.

Figure 6.21: Invariant mass distribution of $\overline{\Lambda}$s from channel c) and Λs from anti-channel for 2015 Pb-Pb data. The S candidates fulfill $r > 40\,\text{cm}$ and the overlap cut. A peak might be conceivable in Figure 6.21b with a significance of $z = 2.3$.

6.7 Methods of background estimation

As described in section 6.6.5, we can not identify S candidates at high radii that unambiguously include a neutral $\overline{\Lambda}$. Some K^0 which are associated to a S candidate have been found in section 6.6.3. However even if we assume very optimistically that all of the signal is caused by true S events, we do not expect to see any difference in the invariant mass distribution if a sideband analysis is applied – see section 6.7.1. The reason for that is that on the one hand the signal-to-background ratio for the K^0s for example in fig. 6.12b is very low, on the other hand – as discussed in section 5.3 – the broadness of the expected S mass peak is large, so that true S events might be distributed in a wide invariant mass range. Moreover regarding channel a), a similar invariant mass analysis can not be done due to the lack of a detectable neutral particle, which is also the reason why S mass reconstruction is difficult for this channel – see section 5.3. Accordingly foresighted, we do not expect to get new convincing results by applying methods of background estimation. Anyway, this will be described and done in the following in order to corroborate our previous results and in order to present methods that could be used in a further analysis. One already applied method is the 'anti-channel'-approach described in section 6.4. In section 6.7.1 a sideband analysis will be done for channel b) and c). Furthermore the mixed event method will be presented, that was applied in an early stage analysis of channel c) but will not be completely accomplished.

6.7.1 Sideband analysis

A suitable method of background estimation for channel b) and c) is the sideband analysis. The general strategy of this method is to divide the invariant mass spectra of the $K^0/\overline{\Lambda}$ in two parts, a 'normalband', and a 'sideband'. The normalband is located in a 2σ range around the mass of the neutral particle m, while the sideband consists of the ranges $[m\text{-}4\sigma;m\text{-}2\sigma]$ and $[m+2\sigma;m+4\sigma]$. Due to the sigma cut one assumes that in the normalband should be the true K^0s/$\overline{\Lambda}s$ together with background, while the sideband only contains background. Accordingly if there is any genuine S candidate then its daughter K^0 should be in the normalband. As a next step, the invariant mass reconstruction for the S candidates can be done separately for those who belong to the normalband and sideband. The invariant mass for both channels is obtained by adding up the 4-momenta of all final particles and subtracting the one of a proton at rest. Both bands should approximately contain the same number of entries because of the same total mass range. Comparing both S mass distributions might reveal any differences that could be a hint for some real S candidates. However, usually the sideband analysis method is applied if there is a dominating peak in the invariant mass distribution of the neutral particle, which is not the case for both channels. Therefore, as already mentioned in the beginning, we do not expect a meaningful result by the application of this method.

Channel b) $\overline{S} + p \rightarrow \bar{p} + K^+ + K^0 + \pi^+$

In Figure 6.22 the m($\bar{p}$,K^+,K^0,π^+) mass distribution for S candidates that fulfill cut *combi*2 and $r > 35\,\text{cm}$ without PID overlap cut is shown – the corresponding invariant mass distribution of the K^0 can be seen in Figure 6.12a. Firstly we compared the normalband distribution to the expected simulated one in Figure 5.4, which shows some commonalities but also differences. The peak position of the experimentally obtained S mass distribution roughly matches to the simulated one, but generally the width is larger for data. Even if one assumes, that the measured m($\bar{p}$,K^+,K^0,π^+) mass distribution is in basic agreement with the phase space simulation, considering that the data might be dominated by background, there is still the fact that the sideband distribution does not generally differ from the normalband. This also holds for the reconstructed m($\bar{p}$,K^+,K^0,π^+) mass distribution if additional m^2 overlap cuts are applied – see Figure 6.23. A subtraction of normalband and sideband distribution shows, that the differences are compatible with zero within the statistical uncertainties, as shown in Figure 6.24 for $r > 35\,\text{cm}$ and applied overlap cut. As already discussed in section 6.6.3, we do only see a few true K^0s that correspond to S candidates especially at higher radii. However if one still assumes that there were some true S events, their daughter K^0 should be in the normalband, and therefore they could contribute to a difference between normal and sideband m($\bar{p}$,K^+,K^0,π^+) mass distributions. As already mentioned in the introduction of this chapter, the method of sideband analysis is only barely applicably for K^0 spectra that do only show a small peak. One should not overestimate the meaningfulness of the fact that there is no significant difference between normalband

and sideband, because as discussed in section 5.3 due to the Fermi-momentum of the proton the S mass distribution is quite broad. Accordingly it can not be excluded that there might be some true S candidates in the normalband that do not contribute to a difference because they are distributed over a wide mass range and therefore are hidden in the total distribution. The shape of normal and sideband are likely determined by phase space effects, because we demand that in total there are 5 final particles with momentum direction restrictions. Of course the sideband analysis was done for various topology and PID cut combinations, leading to similar results. In summary we can say, that the normal band and side band distributions are compatible, as expected from the limited S/B ratio of the K^0s. This result should not be overestimated, because as discussed previously we did not expect to see any difference in the normalband compared to the sideband.

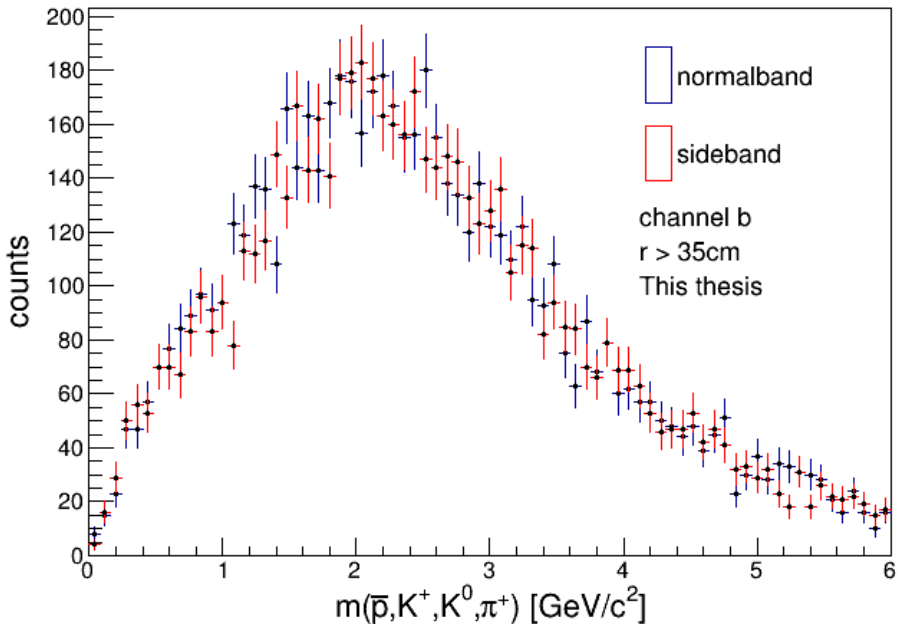

Figure 6.22: Distribution of reconstructed mass m($\bar{p}$,K^+,K^0,π^+) for K^0s in normalband and sideband separately.

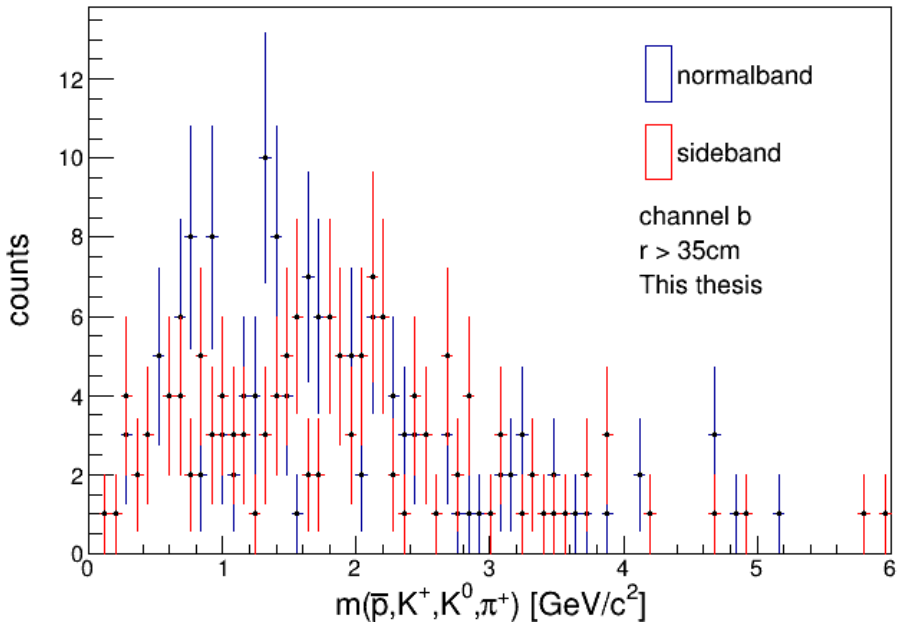

Figure 6.23: Analogous to fig. 6.22 but with additional m^2 overlap cut on $\bar{p}$ and K^+.

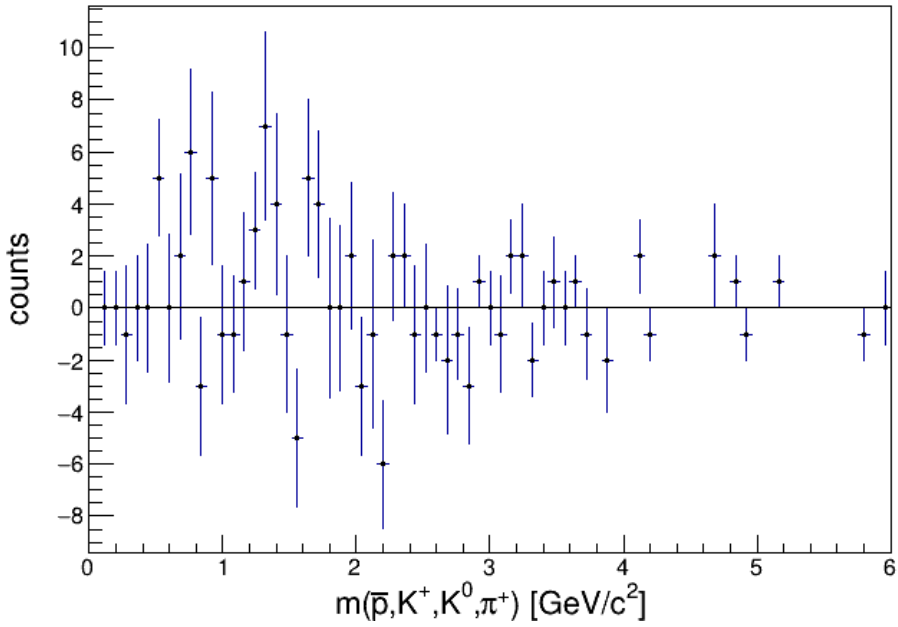

Figure 6.24: Subtraction of normalband and sideband distributions from fig. 6.23.

Channel c) $\overline{S} + p \rightarrow \overline{\Lambda} + K^+ + \pi^- + \pi^+$

In principle the analogous procedure as described previously was repeated for the $\overline{\Lambda}$ in channel c). In contrast to channel b), there was no indication that true secondary $\overline{\Lambda}$s at high radii exist which are associated with an S candidate. Therefore we do not expect to see any difference between normalband and sideband, because both seem to be completely background dominated. If we cannot resolve true $\overline{\Lambda}$s, a more detailed discussion of the S mass distributions is unnecessary at this point and therefore the result of the sideband analysis is only shortly presented. In general the m($\overline{\Lambda}$,K^+,π^-,π^+) mass distribution for channel c), shown in Figure 6.25, looks similar to the one for channel b), if analogous cuts are applied. This supports the hypothesis, that both distributions are determined by phase space effects. Normalband and sideband distribution are compatible within statistical limits, therefore similar arguments as for channel b) apply and we can not obtain an indication for the existence of the S from the sideband analysis.

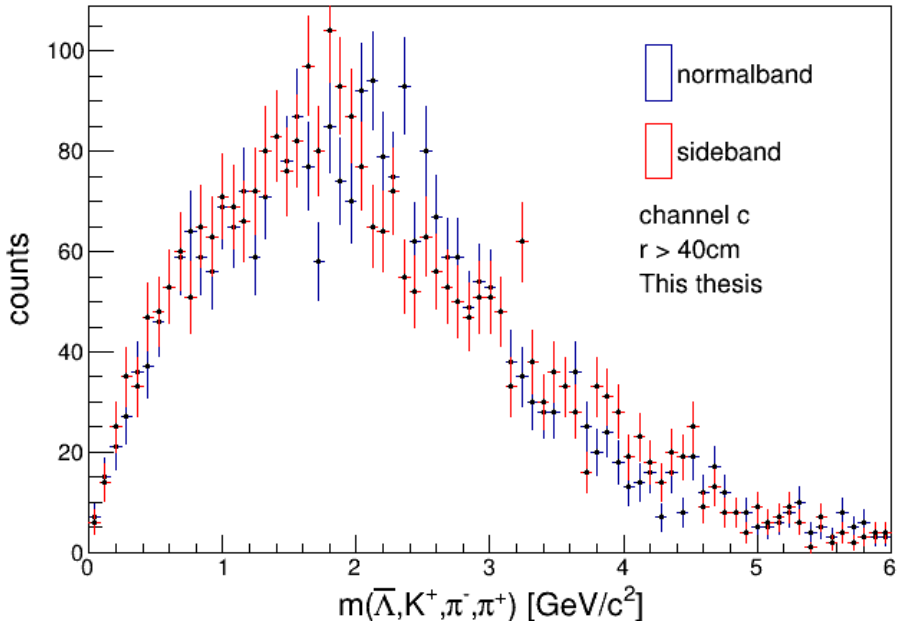

Figure 6.25: Distribution of reconstructed mass m($\overline{\Lambda}$,K^+,π^-,π^+) for $\overline{\Lambda}$s in normalband and sideband separately.

6.7.2 Mixed event

Another method for background estimation is event mixing. This is a general technique in particle physics to decorrelate (two) observables which can be combined to one quantity. As the name indicates, the observables are taken from different events, so that they have to be uncorrelated in contrast to the correlated signal, which is obtained by taking the observables from the same event. A distribution of the quantity of interest

is is made for the same event and mixed event. Assuming that the background in the 'true' same event distribution is uncorrelated, the mixed event distribution can be used as estimation for the background.

Applying a mixed event analysis for the S search is not trivial, because the complex topology has to be taken into account. In an earlier stage of the analysis, mixed event was applied but not further considered because there are some uncertainties concerning mixed event and the focus was set to the invariant mass analysis as described in section 6.6. How the mixed event method could be applied in principle will be described in the following. Under the assumption that the S exists, all momentum vectors of the final particles should be correlated for the S candidates. If the S vertex with three daughter particles is given, then the corresponding K^0 in channel b) respectively $\overline{\Lambda}$ in channel c) must have a correlated absolute momentum and momentum direction. Simply mixing the S vertex with any neutral particle from another event and checking if all cuts are fulfilled is in principle not possible, because we do not expect nuclear interactions to happen always at the same position. We used the strategy to sort S candidates according to their pseudorapidity η and angle ϕ value, that are obtained from the S vertex position. Then a mixing is done between S candidates that have similar η and ϕ values. The S vertex with three daughter tracks is used from one event, while the complete S candidate of the other (Pb-Pb) event is shifted so that both S vertices overlap. Then only the neutral particle and its daughter tracks of the second event are used. Combining the S vertex from the first event and the neutral particle from the second one, a new S_{mixed} candidate is created. If this S_{mixed} candidate fulfills all cuts, especially the in section 6.2 discussed 'scalar product' cut which assures that the total S momentum points in the direction of the primary vertex, then it is stored. This mixing is done until a sufficient number of S_{mixed} candidates is achieved and as described in the beginning, the S_{mixed} mass distribution could be used as estimation for the uncorrelated background in the true S mass distribution. However the described procedure is not a mature method and there are uncertainties including for example phase space effects if the direction is restricted. This is the reason why mixed event was not used in the final version of this analysis, but it could be a reasonable tool in a further study.

6.8 Discussion

In the previous sections reasonable topology and PID cuts were discussed and applied. The general strategy was to study in section 6.6 if there are secondary neutral particles at higher radii which are associated to an S candidate. For comparison and as basic background estimation the anti-channels were used with exactly the same PID and topology cuts. The invariant mass distributions of the $\overline{\Lambda}$ of channel c) did not show a significant peak for most of the tested cut combinations. However for the 2015 data set and applied overlap cuts a peak at high radii ($r > 40\,\text{cm}$) can be resolved with a significance of $z = 2.3$. Accordingly at this point we cannot conclude that any real S candidate had been seen even if we assume perfect PID for all charged particles because mostly no corresponding $\overline{\Lambda}$ was resolved. Of course it is still possible that there are

unseen S events of channel c) which cannot be resolved in particular due to the low number of expected detectable S – see section 5.4 and the dominating background.

A further inspection of channel a) was not done, because due to the lack of a neutral detectable particle an analysis of the invariant mass distribution was not possible. The comparison of the reconstructed S mass for channel a) and the corresponding anti-channel was discussed, however it was not possible to conclude something with regard to the S.

Interestingly we were able to resolve a significant peak in the invariant mass distribution of the K^0s in channel b) with a significance of up to $z = 2.8$. For the anti-channel no analogous peak was seen. In general this is interesting, because if we assume any background due to for example a primary decaying particle, there should be an equal contribution in the anti-channel spectrum. However at this point it is clearly too early to talk about an indication of a discovery, but this was also not the aim of this thesis. There are still uncertainties which could contribute as background sources that cannot yet be determined in detail. A study of $\bar{n}$ and $\bar{p}$ interactions in the detector material in comparison to interactions of n and p would be needed. In general a full GEANT simulation would be a way to obtain a better understanding of possible background sources. A main uncertainty is that we cannot distinguish strongly produced K^0 mesons from their antiparticles $\overline{K^0}$ by detecting the decay of K^0_S because this state is a quantum mechanical mixture. If we in fact detect a K^0_S which was originally a strongly produced $\overline{K^0}$s in channel b), then the strangeness of all final particles would be **S**=0 instead of **S**=2. Accordingly a 'normal' nuclear interaction cannot be excluded as source for the final particles any more. However there is no a priori reason why these normal interactions should not contribute equally in the anti-channel. In contrast to our expectation, cutting on areas where nuclear interactions are supposed to happen did not improve the significance of the K^0 peak, which might be an argument for still contributing yet unknown background sources. The method of sideband analysis for background estimation was presented and performed, although at this point of the analysis it was not able to reveal any interesting discovery. Anyway we can conclude that our results are interesting, because we showed that in general it is feasible to detect S interactions in ALICE and we still get S candidates even if strict topology and PID cuts are applied. During the upcoming Run 3 at the LHC it is expected that ALICE will take approximately a factor 50 more statistics compared to Run 2 as used in this thesis. With this statistics it should be clearly possible to discover the S particle if it exists.

7 Summary and Outlook

In this thesis we focused on the feasibility of detecting the dark matter sexaquark candidate, also called the S particle, at ALICE. Methods of particle identification were studied and applied on various particle species. Combining $n\sigma$ and m^2 cuts, based on the specific energy loss $\mathrm{d}E/\mathrm{d}x$ and time-of-flight measurements, we were able to identify charged particles with sufficient purity. The reconstruction of the neutral K^0_S, $\Lambda^0/\overline{\Lambda^0}$, Ξ^- and Ω^- was performed. Applying topological restrictions for the K^0_S and $\Lambda^0/\overline{\Lambda^0}$ showed that it is challenging to identify secondary neutral particles due to dominating combinatorial background.

In general it was shown that we are capable of detecting secondary hadronic interactions and accordingly resolve the detector structure spatially. This can be seen as a motivation that the S interaction could be detected in a similar way. Possible background sources for the hadronic interactions were discussed.

Conceivable reaction channels of the S with detector material were presented and the most promising ones were chosen for further analysis. A phase space simulation for these chosen channels was done, resulting in particular in the shape of the reconstructed S mass distribution. An estimation for the number of detectable S was done, based on some assumptions. As a result we expect the number of S to be of the order $O(10^1)$ to $O(10^2)$ in the available statistics of about $2.17 \cdot 10^8$ Pb-Pb events.

A main challenge was to find reasonable PID and topology cuts for the S reaction channels in order to assure a high purity and to exclude unreasonable topologies. A first analysis revealed for example that there is background originating from K^0s produced in the vicinity of the primary vertex and pointing backwards to the S vertex. This background source was then excluded in the next step.

Our main strategy was to find secondary neutral particles that belong to an S candidate at high radii away from the primary vertex and to assure they do not correspond to any background by using the 'anti-channel method.' For the channel $\overline{S} + \mathrm{p} \rightarrow \overline{\Lambda} + \mathrm{K}^+ + \pi^- + \pi^+$ no convincing $\overline{\Lambda}$s were found for various topological cut combinations, although interestingly for the 2015 data with few statistics a peak can be resolved with a significance of 2.3. The two data sets might differ because of triggers, while a detailed comparison of them was out of scope for this thesis.

In the channel $\overline{S} + \mathrm{p} \rightarrow \bar{\mathrm{p}} + \mathrm{K}^+ + \mathrm{K}^0 + \pi^+$ secondary K^0s, which belong to an S candidate, were identified with a significance of up to 2.8. The corresponding anti-channel did not show a similar peak. This can be seen as an interesting indication, anyway it should not be overestimated because there might be still unknown background sources as discussed previously. Furthermore the obtained significances only reflect the statistical uncertainties, accordingly further studies have to be done with regard to systematic uncertainties. If the independent results from the two different channels are

combined, then a total significance of $z_{\text{total}} = (2.3+2.8)/\sqrt{2} = 3.6$ is obtained, according to Stouffer's z-score method. However, because the significance of 2.3 has only been seen for one data set, one can only mention the result of $z_{\text{total}} = 3.6$ with reservation. Applying the method of sideband analysis did not lead to a significant result as expected due to the small signal over background ratio.

Although we did not get a significant indication for the S one can conclude with regard to further analyses that it is feasible to search for the S at ALICE. The order of magnitude estimation revealed that there might be enough detectable S and an increase in statistics is possible especially for the upcoming Run 3. Our current results do not exclude that there might be S candidates hidden in the background. In general it is a motivating result that we still see a signal even if strict topology and PID cuts are applied. In future analyses the discussed invariant mass distributions as well as the applied methods of background estimation might be convincing strategies to continue the search for the S particle.

8 Appendix

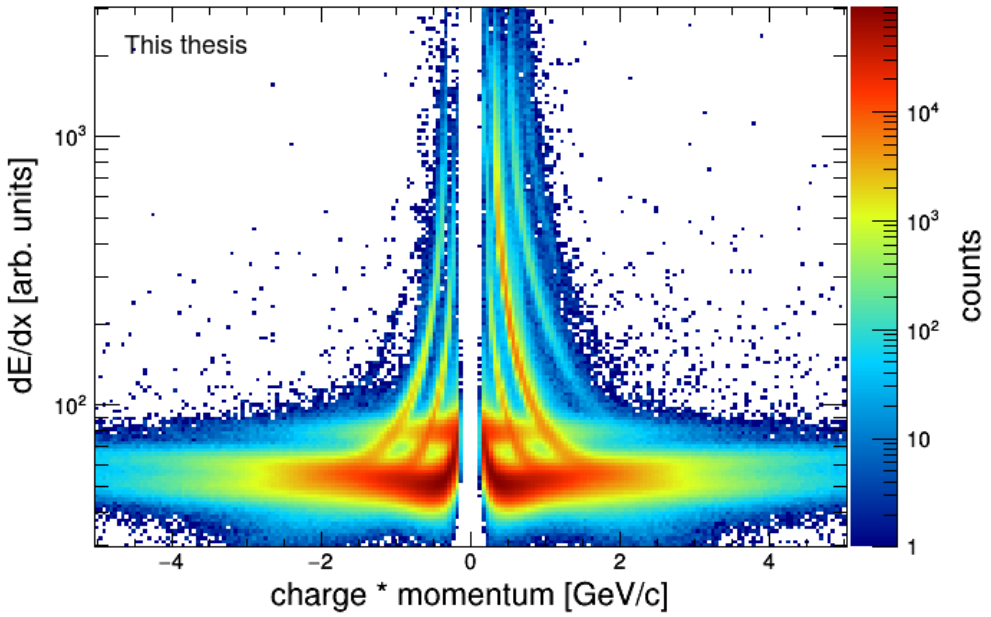

Figure 8.1: Same as Figure 3.1 but for Pb-Pb data. Less statistic is used for this plot but apart from that there are no major differences recognizable compared to p-Pb data.

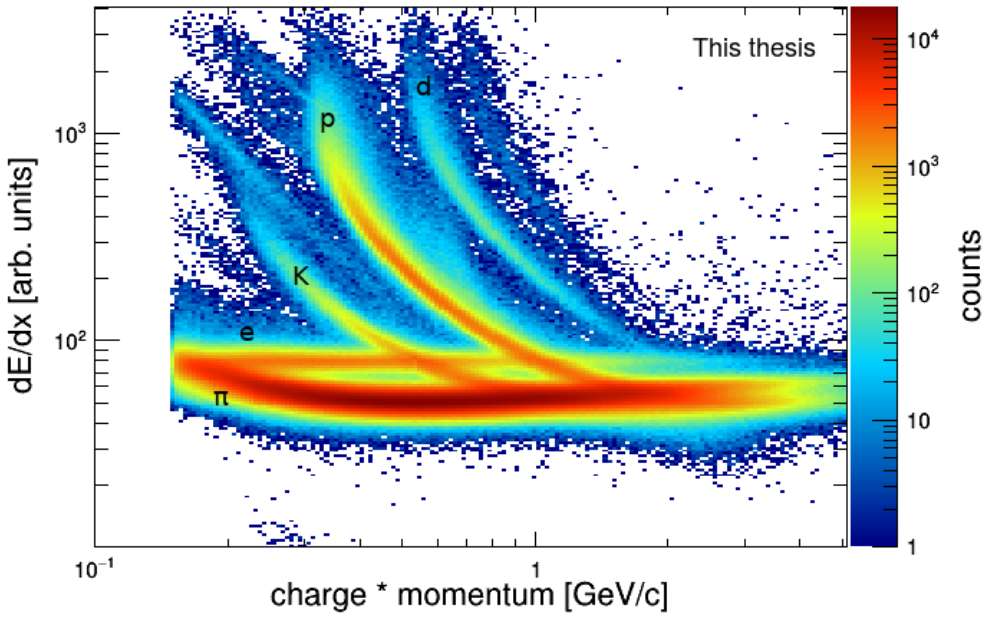

Figure 8.2: Figure 8.1 is shown for positive and logarithmic x axis range.

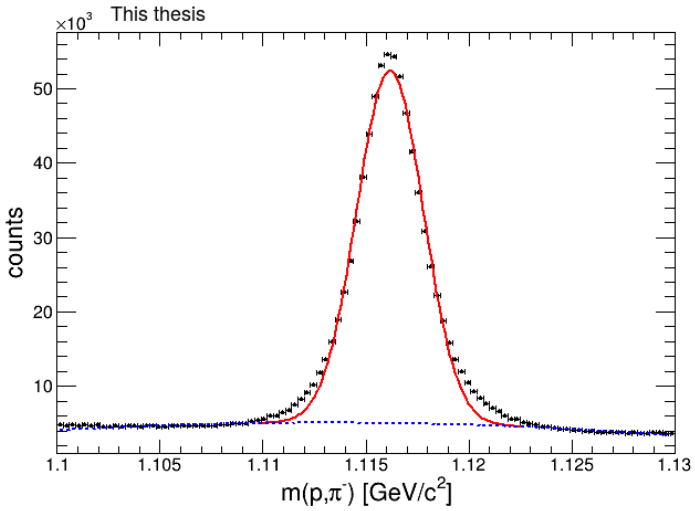

(a)

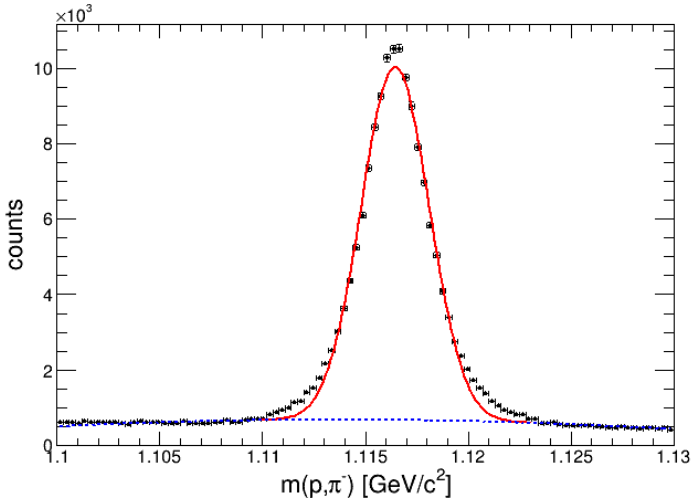

(b)

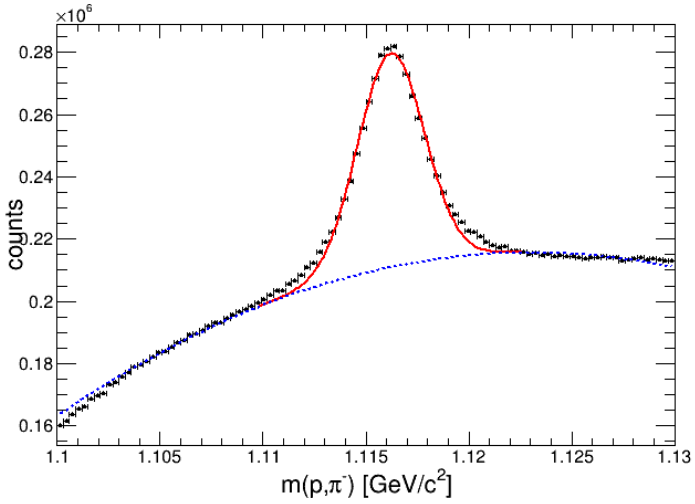

(c)

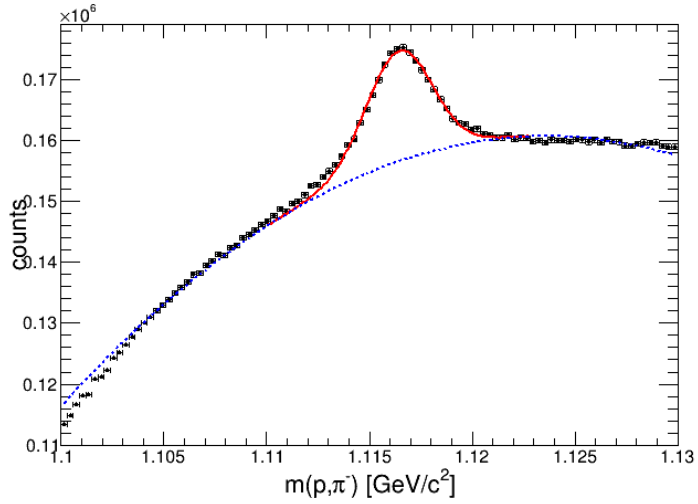

(d)

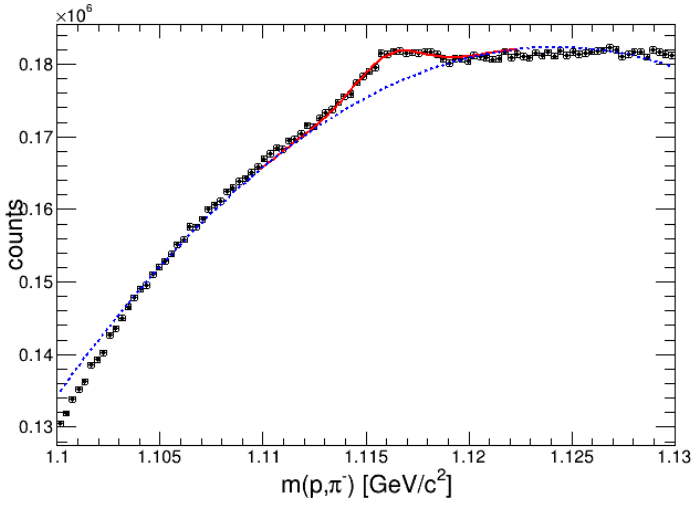

(e)

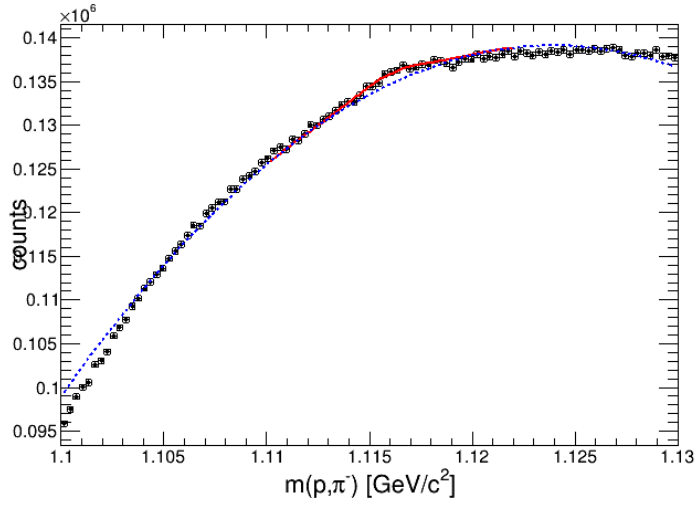

(f)

Figure 8.3: Example invariant mass distributions of p,π^- with restriction $r > 7\,\mathrm{cm}$ (left) and $r > 30\,\mathrm{cm}$ (right). Shown for primary (top row), combined (middle), and secondary particles (bottom).

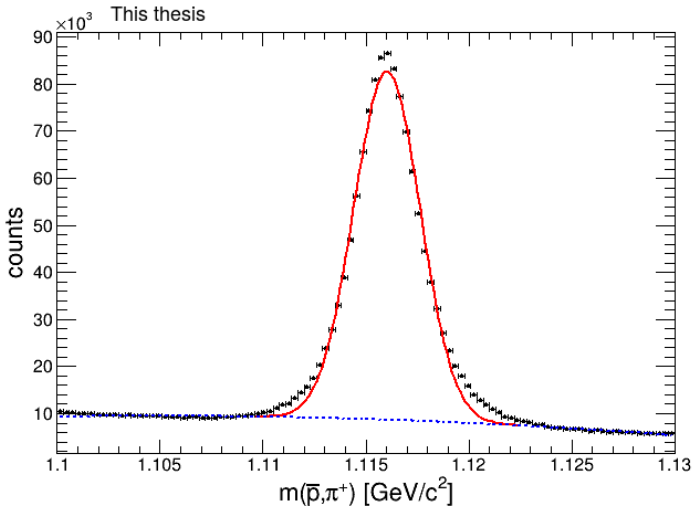

(a)

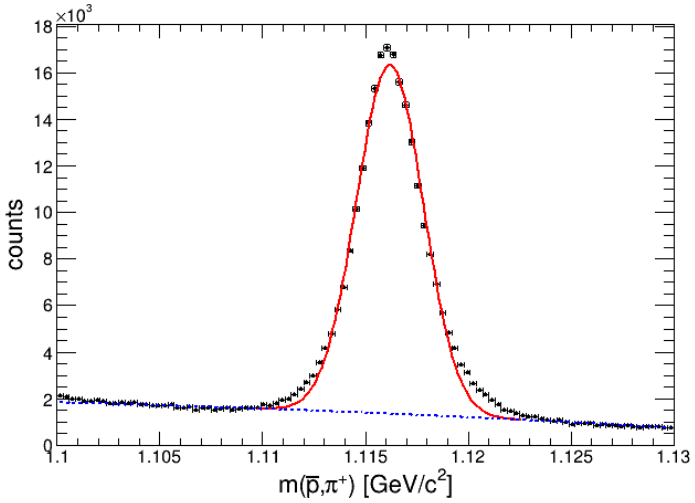

(b)

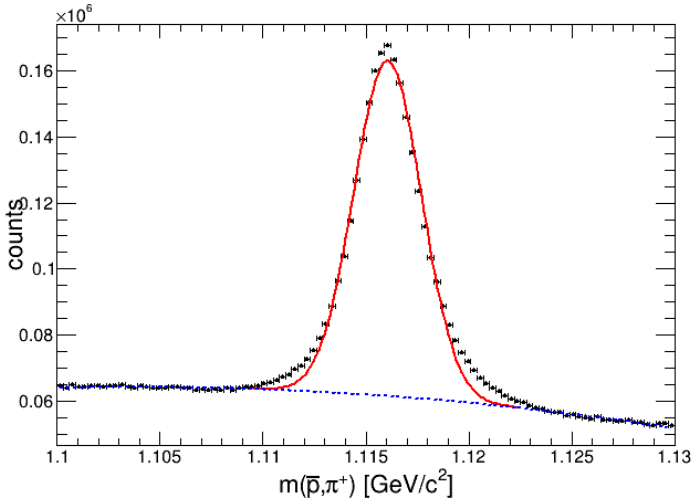

(c)

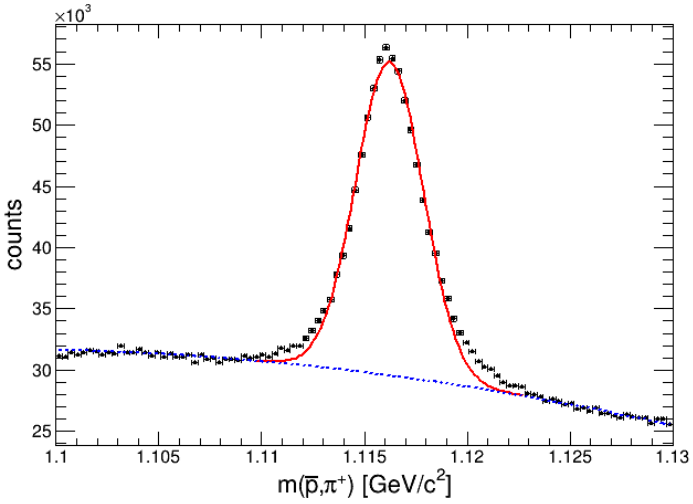

(d)

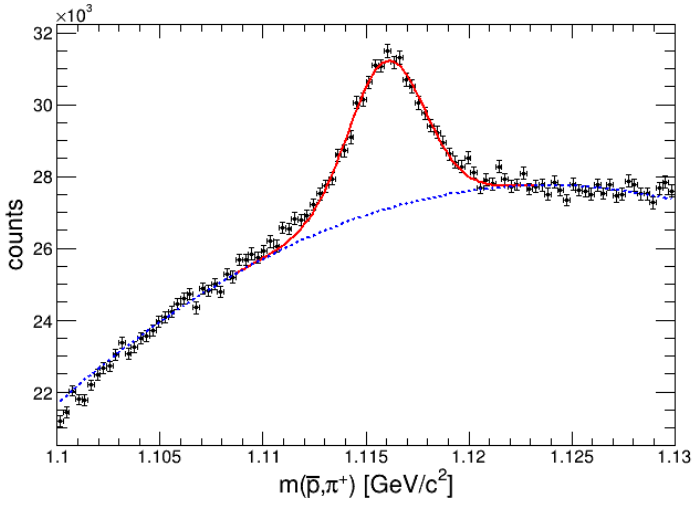

(e)

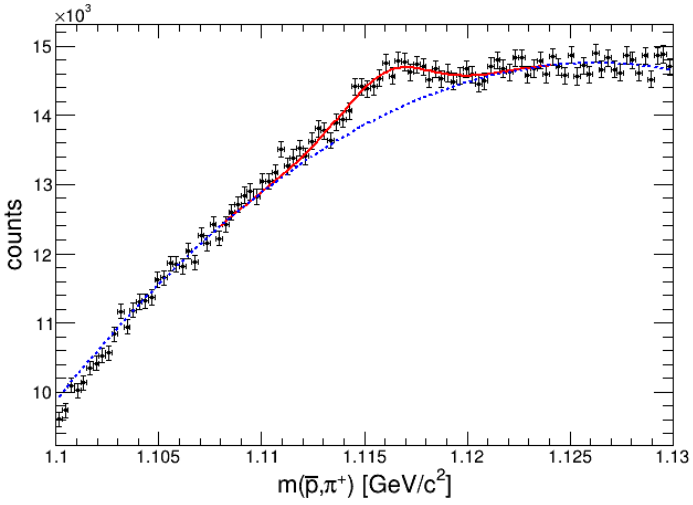

(f)

Figure 8.4: Analogous to Figure 8.3, example histograms for $\overline{\mathrm{p}}$,π^+ are shown.

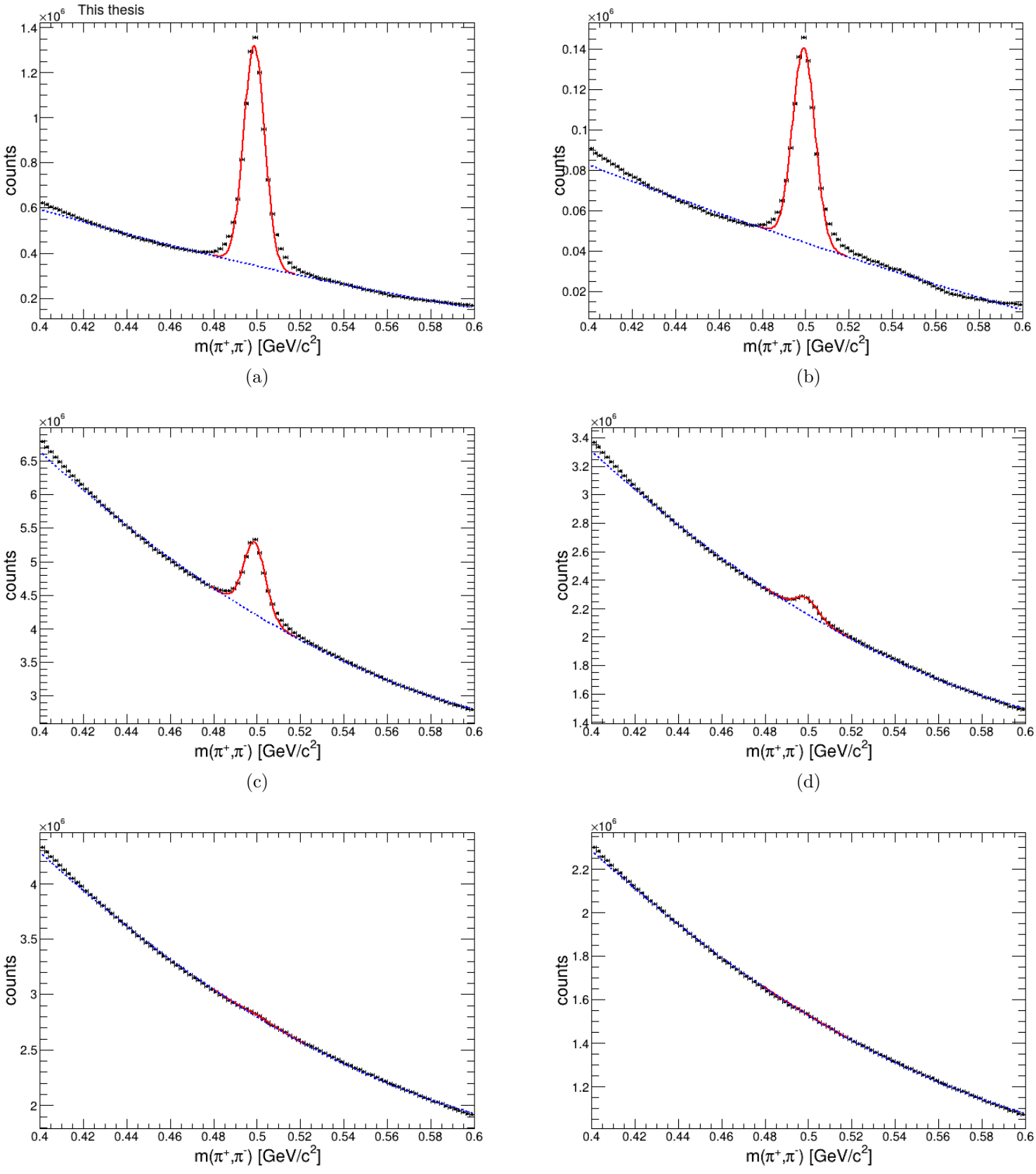

Figure 8.5: One can see example invariant mass distributions for π^-,π^+ with restriction $r > 7\,\text{cm}$ (left) and $r > 30\,\text{cm}$ (right). Depicted for primary (top row), combined (middle), and secondary particles (bottom).

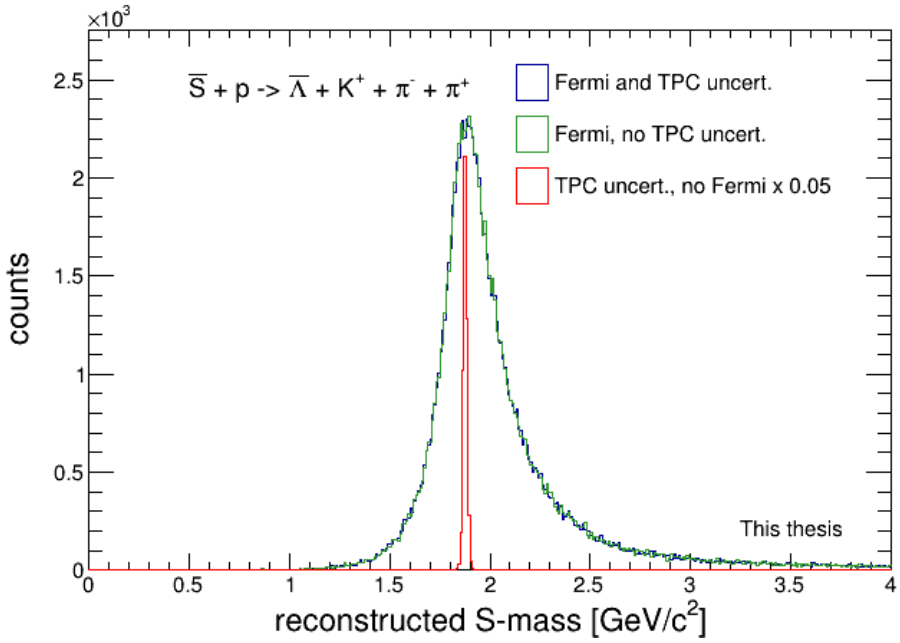

Figure 8.6: Reconstructed S mass for channel c) – analogous to Figure 5.4.

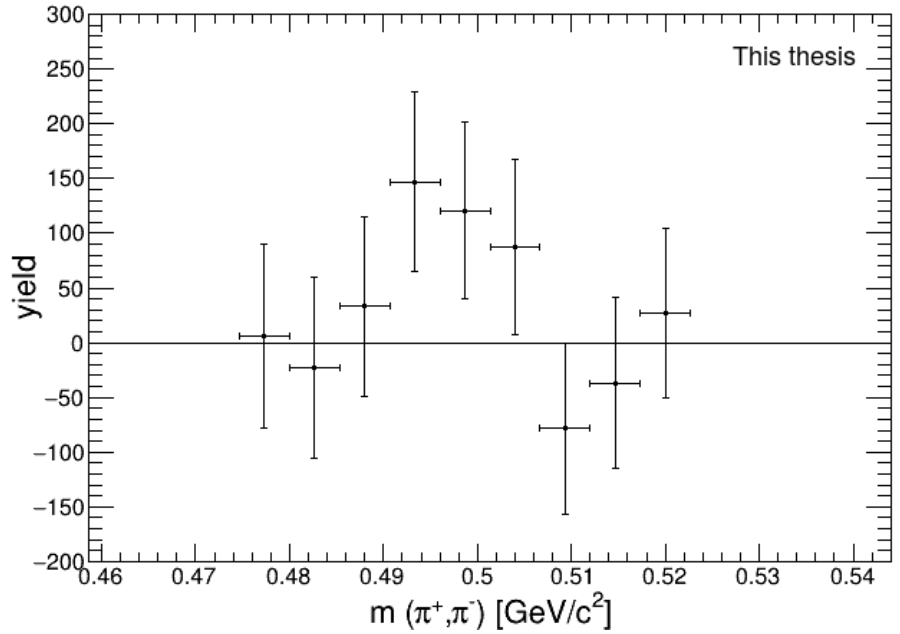

Figure 8.7: Subtraction of polynomial background fit from data in Figure 6.12b.

Acknowledgements

First I want to thank Prof. Klaus Reygers for the idea of searching for the sexaquark and the very helpful discussions.
In particular I would like to thank Dr. Alexander Schmah for his outstanding help concerning physics topics, technical problems and overall strategies. I appreciate the time he spend on helping, motivating and discussing with me.
Furthermore I want to say thanks to Ole Schmidt for his help concerning computer science issues.
Also thanks to Nadine Grünwald, Sven Hoppner and Alexander Schmah for supporting me in the data production.
Last but not least I want to say that it was a pleasure for me to experience the work in this group.

Erklärung

Ich versichere, dass ich diese Arbeit selbstständig verfasst und keine anderen als die angegebenen Quellen und Hilfsmittel benutzt habe.

Bad Rappenau, den 30.03.2021,

Fabio

Bibliography

[1] https://home.cern/science/physics/standard-model.

[2] Mark Thomson. *Modern particle physics*. Cambridge University Press, New York, 2013. 978-1-107-03426-6.

[3] R. P. Feynman. Space-time approach to quantum electrodynamics. *Phys. Rev.*, 76:769–789, Sep 1949.

[4] Ralf Lehnert. CPT Symmetry and Its Violation. *Symmetry*, 8(11):114, 2016.

[5] https://www2.ph.ed.ac.uk/~vjm/Lectures/ParticlePhysics2008_files/Feb25th2008.pdf.

[6] Jun Cao and Miao He. Neutrino oscillation: discovery and perspectives. *Sci. Bull.*, 61(1):48–51, 2016.

[7] https://www.physi.uni-heidelberg.de/~uwer/lectures/PhysikV/Vorlesung/Kapitel-IVc.pdf.

[8] http://hyperphysics.phy-astr.gsu.edu/hbase/Particles/hadron.html.

[9] Murray Gell-Mann. A Schematic Model of Baryons and Mesons. *Phys. Lett.*, 8:214–215, 1964.

[10] G. Zweig. *An SU(3) model for strong interaction symmetry and its breaking. Version 2*, pages 22–101. 2 1964.

[11] R. Aaij, B. Adeva, M. Adinolfi, A. Affolder, Z. Ajaltouni, J. Albrecht, F. Alessio, M. Alexander, S. Ali, G. Alkhazov, and et al. Observation of the resonant character of the z(4430)-state. *Physical Review Letters*, 112(22), Jun 2014.

[12] https://cms.cern/news/x3872-exotic-charmonium-charming-puzzle.

[13] Edvige Corbelli and Paolo Salucci. The extended rotation curve and the dark matter halo of M33. *Monthly Notices of the Royal Astronomical Society*, 311(2):441–447, 01 2000.

[14] M. Milgrom. Dynamics with a nonstandard inertia-acceleration relation: An alternative to dark matter in galactic systems. *Annals of Physics*, 229(2):384–415, Feb 1994.

[15] Steven W. Allen, August E. Evrard, and Adam B. Mantz. Cosmological parameters from observations of galaxy clusters. *Annual Review of Astronomy and Astrophysics*, 49(1):409–470, Sep 2011.

[16] C. L. Bennett, D. Larson, J. L. Weiland, N. Jarosik, G. Hinshaw, N. Odegard, K. M. Smith, R. S. Hill, B. Gold, M. Halpern, and et al. Nine-year wilkinson microwave anisotropy probe (wmap) observations: Final maps and results. *The Astrophysical Journal Supplement Series*, 208(2):20, Sep 2013.

[17] Zeinab Rezaei. Accelerated expansion of the universe in the presence of dark matter pressure. *Canadian Journal of Physics*, 98(2):210–216, Feb 2020.

[18] Brian Robson. *Introductory Chapter: Standard Model of Cosmology.* 04 2019.

[19] Asher Yahalom. The Effect of Retardation on Galactic Rotation Curves. *J. Phys. Conf. Ser.*, 1239(1):012006, 2019.

[20] Edward A. Baltz. Dark matter candidates. *eConf*, C040802:L002, 2004. astro-ph/0412170.

[21] Doron Lemze, Yoel Rephaeli, Rennan Barkana, Tom Broadhurst, Rick Wagner, and Mike L. Norman. Quantifying the collisionless nature of dark matter and galaxies in a1689. *The Astrophysical Journal*, 728(1):40, Jan 2011.

[22] M. Mancuso et al. Searches for Light Dark Matter with the CRESST-III Experiment. *J. Low Temp. Phys.*, 199(1-2):547–555, 2020.

[23] `https://www.mpp.mpg.de/en/research/astroparticle-physics-and-cosmology/dark-matter-experiments/tristan-detector-search-for-sterile-neutrinos`.

[24] Glennys R. Farrar. Stable sexaquark, 2017. 1708.08951.

[25] R. L. Jaffe. Perhaps a stable dihyperon. *Phys. Rev. Lett.*, 38:195–198, Jan 1977.

[26] Tsutomu Sakai, Kiyotaka Shimizu, and Koichi Yazaki. H Dibaryon. *Progress of Theoretical Physics Supplement*, 137:121–145, 03 2000.

[27] Glennys R. Farrar, Zihui Wang, and Xingchen Xu. Dark matter particle in qcd, 2020. 2007.10378.

[28] BaBar Collaboration. Search for a stable six-quark state at babar. *Phys. Rev. Lett.*, 122:072002, Feb 2019.

[29] Florian Partous. The standard model strikes back: Searching for sexaquark dark matter at the lhc. `https://iihe.ac.be/sites/default/files/thesis-florian-partous-cms-master-2018pdf/thesis-florian-partous-cms-master-2018.pdf`.

[30] `https://cds.cern.ch/record/2317058/files/CERN-HR-STAFF-STAT-2017-RESTR.pdf`.

[31] A.J.Eskovitz R.F.Doolittle, U.Pollvogt. Multiwire proportional chamber development. 1973. https://ntrs.nasa.gov/archive/nasa/casi.ntrs.nasa.gov/19730013483.pdf.

[32] http://www.lhc-facts.ch/.

[33] K. Schindl. The injector chain for the LHC. In *9th LEP Performance Workshop*, pages 47–52, 3 1999.

[34] A. Beuret et al. The LHC Lead Ion Injector Chain. In *9th European Particle Accelerator Conference (EPAC 2004)*, 7 2004.

[35] Observation of a new particle in the search for the standard model higgs boson with the atlas detector at the lhc. *Physics Letters B*, 716(1):1–29, 2012.

[36] Alice: Physics performance report, volume ii. 32:1295–2040, 2006.

[37] Marian Ivanov. Identified charged hadron production measured with ALICE at the LHC. *Nucl. Phys. A*, 904-905:162c–169c, 2013.

[38] G. Dellacasa et al. ALICE technical design report of the inner tracking system (ITS). 6 1999.

[39] J. Alme, Y. Andres, H. Appelshäuser, S. Bablok, N. Bialas, R. Bolgen, U. Bonnes, R. Bramm, P. Braun-Munzinger, R. Campagnolo, and et al. The alice tpc, a large 3-dimensional tracking device with fast readout for ultra-high multiplicity events. *Nuclear Instruments and Methods in Physics Research Section A: Accelerators, Spectrometers, Detectors and Associated Equipment*, 622(1):316–367, Oct 2010.

[40] Weilin Yu. Particle identification of the alice tpc via de/dx. *Nuclear Instruments and Methods in Physics Research Section A: Accelerators, Spectrometers, Detectors and Associated Equipment*, 706:55 – 58, 2013. TRDs for the Third Millenium.

[41] The alice transition radiation detector: Construction, operation, and performance. *Nuclear Instruments and Methods in Physics Research Section A: Accelerators, Spectrometers, Detectors and Associated Equipment*, 881:88 – 127, 2018.

[42] *ALICE Time-Of-Flight system (TOF): Technical Design Report.* Technical Design Report ALICE. CERN, Geneva, 2000.

[43] Arturo Tauro. ALICE Schematics. ALICE-PHO-SKE-2017-001, May 2017.

[44] Particle Data Group. Review of Particle Physics. *Progress of Theoretical and Experimental Physics*, 2020(8), 08 2020. 083C01.

[45] G. Dellacasa et al. ALICE: Technical design report of the time projection chamber. 1 2000. CERN-OPEN-2000-183, CERN-LHCC-2000-001.

[46] Rudolph Emil Kalman. A new approach to linear filtering and prediction problems. *Transactions of the ASME–Journal of Basic Engineering*, 82(Series D):35–45, 1960.

[47] Yan Pei, Swarnendu Biswas, Donald Fussell, and Keshav Pingali. An elementary introduction to kalman filtering. *Communications of the ACM*, 62, 10 2017.

[48] K.Safarik Y.Belikov, M.Ivanov. Tpc tracking and particle identification in high-density environment. 2003. https://arxiv.org/abs/physics/0306108.

[49] Vladimir Peskov, Micro Planicic, and Francisco García. Technical design report for the upgrade of the alice time projection chamber, 03 2014. 10.13140/RG.2.1.1761.7681.

[50] Johannes Stiller. Gain calibration of the ALICE TRD using the decay of ^{83m}Kr by internalconversion. *Nucl. Instrum. Meth. A*, 706:20–22, 2013.

[51] Elena Botta. Particle identification performance at ALICE. In *5th Large Hadron Collider Physics Conference*, 9 2017. 1709.00288.

[52] https://alice-analysis.web.cern.ch/sites/alice-analysis.web.cern.ch/files/documents/Analysis/JensJD.pdf.

[53] Nicolò Jacazio. Pid performance of the alice-tof detector in run 2, 2018. 1809.00574.

[54] J. Adam, D. Adamová, M. M. Aggarwal, G. Aglieri Rinella, M. Agnello, N. Agrawal, Z. Ahammed, S. Ahmad, S. U. Ahn, and et al. Determination of the event collision time with the alice detector at the lhc. *The European Physical Journal Plus*, 132(2), Feb 2017.

[55] https://pdg.lbl.gov/2018/listings/rpp2018-list-K-zero.pdf.

[56] https://pdg.lbl.gov/2018/listings/rpp2018-list-lambda.pdf.

[57] Friederike Bock. Neutral pion and eta meson production in pp and pb–pbcollisions at the lhc with the alice detector, 2012. https://www.physi.uni-heidelberg.de//Publications/Bock-Masterthesis.pdf.

[58] J. Wiechula. Commissioning and calibration of the alice tpc. 2008. https://www.uni-frankfurt.de/46491136/Generic_46491136.pdf.

[59] A. Bodek, M. E. Christy, and B. Coopersmith. Effective spectral function for quasielastic scattering on nuclei. *The European Physical Journal C*, 74(10), Oct 2014.

[60] Shreyasi Acharya et al. Multiplicity dependence of light (anti-)nuclei production in p-Pb collisions at $\sqrt{s_{NN}} = 5.02$ TeV. *Phys. Lett. B*, 800:135043, 2020. 1906.03136.

[61] https://alice-publications.web.cern.ch/sites/alice-publications.web.cern.ch/files/papers/716/PTresolution_vs_1Pt_pPb_2013_PerfPaper-8441.png.

[62] J. Adam, D. Adamová, M. M. Aggarwal, G. Aglieri Rinella, M. Agnello, N. Agrawal, Z. Ahammed, I. Ahmed, S. U. Ahn, I. Aimo, and et al. Production of light nuclei and anti-nuclei in pp and pb-pb collisions at energies available at the cern large hadron collider. *Physical Review C*, 93(2), Feb 2016.

[63] Peter Braun-Munzinger, Krzysztof Redlich, and Johanna Stachel. Particle production in heavy ion collisions. *Quark–Gluon Plasma 3*, page 491–599, Jan 2004.

[64] Jean Letessier and Johann Rafelski. *Hadrons and Quark–Gluon Plasma*. Cambridge Monographs on Particle Physics, Nuclear Physics and Cosmology. Cambridge University Press, 2002.

[65] Anton Andronic, Peter Braun-Munzinger, Krzysztof Redlich, and Johanna Stachel. Decoding the phase structure of qcd via particle production at high energy. *Nature*, 561(7723):321–330, Sep 2018.

[66] PD Dr. Klaus Reygers Prof. Dr. Johanna Stachel. Qgp physics - from fixed target to lhc, 2011. `https://www.physi.uni-heidelberg.de/~reygers/lectures/2011/qgp/qgp_02_kinematics.pdf`.

[67] Dezember 2020. Prof. Dr. Klaus Reygers, private communication.

[68] Shreyasi Acharya et al. Measurement of the low-energy antideuteron inelastic cross section. *Phys. Rev. Lett.*, 125(16):162001, 2020. 2005.11122.

[69] S. Acharya, D. Adamová, A. Adler, J. Adolfsson, M.M. Aggarwal, G. Aglieri Rinella, M. Agnello, N. Agrawal, Z. Ahammed, S. Ahmad, and et al. Measurement of the low-energy antideuteron inelastic cross section. *Physical Review Letters*, 125(16), Oct 2020.

[70] S. Okubo. Phi meson and unitary symmetry model. *Phys. Lett.*, 5:165–168, 1963.

[71] `https://pdg.lbl.gov/2014/tables/rpp2014-tab-mesons-strange.pdf`.

[72] David Rohr. Tracking performance in high multiplicities environment at alice, 2017. 1709.00618.

[73] F. Carnesecchi. Performance of the alice time-of-flight detector at the lhc. *Journal of Instrumentation*, 14(06):C06023–C06023, Jun 2019.

[74] `https://root.cern.ch/doc/master/classTEveManager.html`.

[75] `https://pdg.lbl.gov/2020/listings/contents_listings.html`.

[76] Aamodt et al. Midrapidity antiproton-to-proton ratio in pp collisions at $\sqrt{s} = 0.9$ and 7 tev measured by the alice experiment. *Physical Review Letters*, 06 2010.